Facilitating miniaturized bioanalytical assays in microfluidic devices

Thesis by

Dmitriy V. Zhukov

In Partial Fulfillment of the Requirements for the degree of

Doctor of Philosophy

CALIFORNIA INSTITUTE OF TECHNOLOGY

Pasadena, California

2020

(Defended December 13th, 2019)

Dmitriy V. Zhukov
ORCID: 0000-0002-4834-3147

ACKNOWLEDGEMENTS

I would like to start by thanking Caltech and the Division of Chemistry and Chemical Engineering for giving me the opportunity to pursue my doctorate degree at this extraordinary institution. It has been a privilege to interact with and work alongside some of the brightest minds these last few years. This dissertation manifests an ending to one of my life's most formative phases thus far, and I feel enormous gratitude for all my time at Caltech.

I want to express special thanks to my advisor, Professor Rustem F. Ismagilov. Rustem has been a tireless champion for me since my first days at Caltech and a big source of inspiration throughout my time in his lab. I am indebted to him for all the support and intellectual guidance that I depended on throughout graduate school and for playing a monumental role in shaping my identity as a scientist. I aspire to be as driven, focused, and patient as Rustem.

All of the members of Ismagilov Lab will always have a special place in my heart. Specifically, I would like to thank the wonderful people that I collaborated with: Tahmineh Khazaei, Justin Rolando, Erik Jue, Stefano Begolo, David Selck, Eugenia Khorosheva, Jacob Barlow, Si Hyung Jin, Jesus Rodriguez-Manzano, Mikhail Karymov, Liang Li, and Wenbin Du. I don't say this enough, but I am extremely appreciative of my colleagues and close friends Tahmineh Khazaei, Said Bogatyrev, and Justin Rolando for all the words of encouragement and advice, for being there for me during tough times, and for celebrating with me in the times of success.

I want to express my appreciation for everyone else that I was fortunate to overlap with in Ismagilov Lab, including Asher Preska Steinberg, Roberta Poceviciute, Travis Schlappi, Daan Witters, Matthew Curtis, Mary Arrastia, Nathan Schoepp, Joanne Lau, Eric Liaw, Octavio Mondragón-Palomino, Michael Porter, Songzi Kou, Weishan Liu, Liang Ma, Alexandre Persat, Sujit Datta, Joong Hwan Bahng, Matt Cooper, Anna Romano, Emily Savela, Sarah Simon, and Alex Winnett. Natasha Shelby deserves a special recognition for all the help with writing and organizing that went into this thesis, and countless other things that we worked on together.

I would also like to express my gratitude to Professors Dave Tirrell, Mitch Guttman, and Wei Gao for serving alongside Rustem on my thesis committee and being a part of my academic growth. I

have collaborated with multiple members of the Guttman Lab, whom I wish to acknowledge: Alexander Shishkin, Mario Blanco, Prashant Bhat, and Mason Lai.

My gratitude extends to all the faculty whose classes I was fortunate enough to be a part of, for their stimulating course material and intellectual influence: Professors Justin Bois, Matt Thomson, Lior Pachter, Michael Elowitz, Jared Leadbetter, Zhen-Gang Wang, John Brady, Frances Arnold, Niles Pierce, Thomas Miller, and Konstantinos Giapis. As well as my brilliant classmates, whom I spent countless hours studying with: Emily Wyatt, Roberta Poceviciute, Nick Porubsky, Yapeng Su, Matthew Curtis, Mikey Phan, Ahmad Omar, and Jordan Dykes. My life at Caltech would also not be as enjoyable and memorable without my friends, including but not limited to Samuel Ho, Kelly Zhang, Bryan Yoo, Lucy Chong, Aaron Markowitz, and Scott Saunders.

Of course, this section would not be complete without an acknowledgement of my family's unwavering support of all my undertakings. From an early age, they have allowed me a great deal of autonomy and have always been supportive of my choices along the way.

Finally, I would like to acknowledge the National Science Foundation (Graduate Research Fellowship Program Grant # DGE-1144469) and Donna & Benjamin M. Rosen Bioengineering Center at Caltech for the generous financial support of the work presented in this dissertation.

ABSTRACT

This work describes several efforts in making microfluidic lab-on-a-chip technology more convenient to use for bioanalysis in limited-resource settings (Chapters 2-3), and describes a device for miniaturized multistep process execution (Chapter 4). One underlying theme of these projects is the streamlining of the ‘chip-to-world’ interfacing to help bring this technology from specialized labs of its developers into more widespread utilization by potential users in other disciplines. Chapter 2 outlines a portable method for achieving stable fluid pumping for sample loading and flow control in microfluidic devices. Chapter 3 details a method for digital nucleic acid test readout with unmodified smartphone cameras. Chapter 4 demonstrates a lab-on-a-chip platform capable of carrying out complex multiplexed biochemical reactions requiring multiple sequential additions of reagents by performing RNA barcoding for multiplexed cDNA library generation.

PUBLISHED CONTENT AND CONTRIBUTIONS

Chapter II: Stefano Begolo*, Dmitriy V. Zhukov*, David A. Selck, Liang Li, Rustem F. Ismagilov. 2014 “The pumping lid: investigating multi-material 3D printing for equipment-free, programmable generation of positive and negative pressures for microfluidic applications.” Lab on a Chip 14(24): 4616-4628. doi: 10.1039/C4LC00910J.

*Equal contribution

Author contributions

Stefano Begolo: Took the lead for Figures 2.4, 2.5, 2.6B. Shared responsibility for Figures 2.1, 2.3, 2.7. Developed model for pressure values (Figure 2.1) and laminar flow (Figure 2.5).

Dmitriy V. Zhukov: Took the lead for Figure 2.2. Shared responsibility for Figures 2.1, 2.3, 2.7. Developed model for VLE experiments (Figure 2.7).

David A. Selck: Provided devices for Figure 2.6. Wrote software for the data acquisition in Figures 2.1 and 2.2.

Liang Li: Provided images and performed experiments for Figure 2.6A.

Chapter III: Jesus Rodriguez-Manzano*, Mikhail A. Karymov*, Stefano Begolo, David A. Selck, Dmitriy V. Zhukov, Erik Jue, and Rustem F. Ismagilov. 2016 "Reading Out Single-Molecule Digital RNA and DNA Isothermal Amplification in Nanoliter Volumes with Unmodified Camera Phones." ACS NANO. 10(3): 3102-3113. doi: 10.1021/acsnano.5b07338.

*Equal contribution

Author contributions

Jesus Rodriguez-Manzano: Developed idea, designed experiments and prepared the manuscript. Took the lead for TOC, Figure 3.1, Figure 3.2, Figure 3.3, Figure 3.4, Figure 3.5, Figure S3.1, Figure S3.2, Figure S3.3, Figure S3.8, and Table TS3.1. Shared responsibility for Figure 3.6. Involved in developing idea for enhancing contrast by image processing. Involved in developing idea for predicting RGB ratiometric signal output based on transmittance spectra for positive and negative amplification reactions containing indicator dye and the spectral sensitivity of an image sensor. Involved in writing ImageJ macro for image processing.

Mikhail A. Karymov: Developed idea, designed experiments and helped with manuscript preparation. Took the lead for Figure 3.6 and Figure S3.6. Shared responsibility for Figure 3.4 and Figure 3.5. Wrote ImageJ macro for image processing and automatic counting.

Stefano Begolo: Developed idea and designed experiments. Shared responsibility for Figure 3.1, Figure 3.2 and Figure 3.3. Developed idea of enhancing contrast between positive and negative reaction by image processing. Wrote ImageJ macro for image processing.

David A. Selck: Took the lead for Figure S3.7. Shared responsibility for Figure 3.2 and Figure 3.5. Helped with fluorescent images for Figure 3.4 and Figure 3.6. Developed idea of enhancing contrast between positive and negative reaction by image processing. Developed idea for predicting RGB ratiometric signal output based on transmittance spectra for positive and negative amplification reactions containing indicator dye and the spectral sensitivity of an image sensor.

Dmitriy V. Zhukov: Took the lead for Figure S3.4, Figure S3.5, Figure S3.9 and Figure S3.10. Designed, optimized and fabricated rotational MV SlipChip device for Figure 3.4 and Figure 3.5.

Designed and fabricated the two-step SlipChip device for Figure 3.6. Helped JRM for MV experiments.

Erik Jue: Designed and tested C-clamp interface for the pumping lid. Used the C-clamp pumping lid to help load the multivolume device for a handful of experiments until JRM was trained. Designed and fabricated MV device with insertable washer features to aid slipping. MV device with washer has been used for TOC, Figure 3.4 and Figure 3.5.

Chapter IV: Dmitriy V. Zhukov, Eugenia M. Khorosheva, Tahmineh Khazaei, Wenbin Du, David A. Selck, Alexander A. Shishkin, Rustem F. Ismagilov. 2019 "Microfluidic SlipChip device for multistep multiplexed biochemistry on a nanoliter scale." Lab on a Chip, 19(19): 3200-3211. doi: 10.1039/C9LC00541B.

Author contributions:

Dmitriy V. Zhukov: Based on the initial prototype by D.A.S., improved, fabricated, and tested subsequent drop-in device prototypes. Designed, fabricated, and tested final drop-in device prototypes, with feedback from E.M.K. Performed experiments to generate data for Figures 4.3 and 4.4. Performed on-device steps of the experiments to generate data for Figure 4.6, together with E.M.K. Analyzed sequencing data results for Figure 4.6. Generated Figures 4.1, 4.2, 4.3, 4.4, 4.5 (right panel), 4.6, S4.1, S4.2, S4.3, S4.4. Contributed to writing of all sections of the manuscript and supporting information.

Eugenia M. Khorosheva: Major contributor to the idea of making the device for barcoding for RNAseq. Re-designed RNAtag-Seq protocol (from extraction to barcoding) to perform it as an additive protocol on device. Key additions/changes: selected published lysis methods that work for bacteria and do not impair ligation performance; verified that each step works well for small initial number of loaded RNA molecules; used surfactants, and added buffers step-wise to allow for performing a pipeline of biochemical reactions on device without any intermediate clean ups; implemented wash buffer to stop ligation and allow for pooling nucleic acids well enough so the loss on water/oil interface is neglectable. Contributed to writing Experimental and SI sections.

Tahmineh Khazaei: Developed pipeline to process and analyze sequencing data. Analyzed data shown in Figure 4.6.

Wenbin Du: Theorized the drop-in idea in the context of microfluidic SlipChip devices. Generated Figure 4.5 (left panel).

David A. Selck: Designed the initial drop-in device prototype. Optimized the automatic spotting process.

Alexander A. Shishkin: Major contributor to the idea of making the device for barcoding for RNAseq. Re-designed RNAtag-Seq protocol off device to work for small initial number of loaded RNA molecules. Key additions/changes: suggested addition UMIs to p38 sequence, suggested modified R14 and P38 sequences; optimized intermediate clean up between off device reactions using MyOneSilane beads and final 0.6 - 0.7 v/v EtOH for size selection.

TABLE OF CONTENTS

LIST OF ILLUSTRATIONS AND/OR TABLES

CHAPTER 1

Introduction

Microfluidics, the study of fluids confined by sub-millimeter geometric features, has proved itself a useful set of tools for applications that are difficult to investigate with more traditional, macroscopic methods. Shrinking the experiments down produces multiple advantages, such as lower reagent volumes, shorter reaction times, and the potential for high-level multiplexing, to name a few.[1,2] With dimensions and volumes that approach those of the fundamental biological units themselves (*e.g.* cells and macromolecules), microfluidics stands to benefit fields such as molecular diagnostics and single-cell omics (*e.g.* genomics, transcriptomics, and proteomics with single-cell resolution) in particular.

Since its inception, the field of microfluidics has amassed a wealth of capabilities and devices dealing with pressing challenges of biology, chemistry, and medicine. However, the fact that operation of many of these devices requires substantial additional equipment like pumps, power supplies, and signal readout instruments, has been commonly overlooked. Not surprisingly, the large size of these external appliances relative to microfluidic components themselves frequently undermines many of the practical benefits of assay miniaturization and claims to portability.[3] The goal of the first two chapters of my thesis work has been to address these obstacles and to improve the stand-alone usability of microfluidic devices, in an effort of making them more portable and more friendly to resource-limited settings.

Chapter II addresses the challenge of pumping in microfluidic devices. Since many microfluidic workflows require stable pressure gradients and sample flows, not to mention sample loading before an assay can even begin, pumping method development has been an active area of lab-on-a-chip research.[4] While good enough to demonstrate a proof-of-concept microfluidic device operation in lab, typical lab bench pumps are bulky, expensive, and power grid dependent. A portable version of a pump would be able to liberate microfluidic technology out of the labs where it is being developed into the labs of users (such as biologists and clinicians) and into a range of other applications in

resource-limited settings. In this previously published work on which I am a co-first author, we first theorize and then use multimaterial 3D printing to create and validate such pumping mechanisms. We show that these pumps provide precise and predictable control of flow over a wide range of flow rates, independent of the sample's volume, surface energy, and density. Also, unlike their classical counterparts, these pumps don't have any moving parts—an important feature for applications requiring stable flows (*e.g.* droplet generation by flow focusing).[5] We further demonstrate the utility of these 3D printed, attachable pumps with a variety of microfluidic devices, requiring both positive and negative relative pressures. We also show this technology's sufficient robustness to operator error by asking an untrained 6-year-old user to load a device.

At the other end of a microfluidic assay workflow is the result readout. Making this part robust to the environment and the user's level of training, while not requiring specialized equipment, is a significant challenge to democratization of lab-on-a-chip technology.[6] Chapter III of this thesis presents previously published work (on which I am a contributing author) in which we demonstrate a quantitative, ultrasensitive microfluidic nucleic acid amplification test that permits the counting of single DNA and RNA molecules using an unmodified camera phone. This is accomplished by combining colorimetric indicator dye and a digital isothermal amplification strategy inside a microfluidic device, together with an image processing algorithm that converts the endpoint change in color into a ratiometric readout. The conversion of the colorimetric signal to its ratiometric alternative is central to the robustness of the method, since it normalizes for ambient lighting conditions. We also demonstrate that this is a hardware-agnostic approach by testing several smartphone cameras and imaging devices.

In addition to all the benefits of miniaturization mentioned above, microfluidic technology also holds the potential for integrating entire laboratory procedures on a single chip (hence the term lab-on-a-chip).[7] In Chapter IV, I switch gears from the previous chapters and explore this angle. In this previously published work on which I am the first author, I present a versatile, SlipChip-based microfluidic platform as an approach for performing multistep biochemical reactions in a multiplexed format on a nanoliter scale. With its straightforward chip-to-world interfacing (requiring only pipette and manual operation), this technology provides an accessible approach that addresses

a previously unfilled niche in the reaction miniaturization field.[3] We demonstrate the device's functionality by performing a complex multistep biochemical scheme—barcode ligation of RNA transcripts for downstream multiplexed sequencing. Our comparative analysis shows that the multistep device's performance is competitive with the current state of transcriptomic technologies. This simple-to-use lab-on-a-chip technology for sequentially merging droplets in parallel will enable numerous applications, and will be particularly beneficial for protocols and biological assays such as biomarker detection, nucleic acid quantification, and time-sensitive reactions.

References

1. A. Folch, *Introduction to bioMEMS*, CRC Press, **2016**.
2. D. J. Beebe, G. A. Mensing, and G. M. Walker, "Physics and Applications of Microfluidics in Biology," *Annual Review of Biomedical Engineering*, **2002**, 4, 261-286.
3. M. I. Mohammed, S. Haswell, and I. Gibson, "Lab-on-a-chip or Chip-in-a-lab: Challenges of Commercialization Lost in Translation," *Procedia Technology*, **2015**, 20, 54-59.
4. Y.-N. Wang and L.-M. Fu, "Micropumps and biomedical applications – A review," *Microelectronic Engineering*, **2018**, 195, 121-138.
5. V. Gnyawali, M. Saremi, M. C. Kolios, and S. S. H. Tsai, "Stable microfluidic flow focusing using hydrostatics," *Biomicrofluidics*, **2017**, 11, 034104.
6. E. Fu, "Enabling robust quantitative readout in an equipment-free model of device development," *Analyst*, **2014**, 139, 4750-4757.
7. M. Boyd-Moss, S. Baratchi, M. Di Venere, and K. Khoshmanesh, "Self-contained microfluidic systems: a review," *Lab on a Chip*, **2016**, 16, 3177-3192.

CHAPTER 2

The pumping lid: Investigating multi-material 3D printing for equipment-free, programmable generation of positive and negative pressures for microfluidic applications

Abstract

Equipment-free pumping is a challenging problem and an active area of research in microfluidics, with applications for both laboratory and limited-resource settings. This paper describes the pumping lid method, a strategy to achieve equipment-free pumping by controlled generation of pressure. Pressure was generated using portable, lightweight, and disposable parts that can be integrated with existing microfluidic devices to simplify workflow and eliminate the need for pumping equipment. The development of this method was enabled by multi-material 3D printing, which allows fast prototyping, including composite parts that combine materials with different mechanical properties (e.g. both rigid and elastic materials in the same part). The first type of pumping lids we describe was used to produce predictable positive or negative pressures via controlled compression or expansion of gases. A model was developed to describe the pressures and flow rates generated with this approach and it was validated experimentally. Pressures were pre-programmed by the geometry of the parts and could be tuned further even while the experiment was in progress. Using multiple lids or a composite lid with different inlets enabled several solutions to be pumped independently in a single device. The second type of pumping lids, which relied on vapor-liquid equilibrium to generate pressure, was designed, modeled, and experimentally characterized. The pumping lid method was validated by controlling flow in different types of microfluidic applications, including the production of droplets, control of laminar flow profiles, and loading of SlipChip devices. We believe that applying the pumping lid methodology to existing microfluidic devices will enhance their use as portable diagnostic tools in limited resource settings as well as accelerate adoption of microfluidics in laboratories.

Introduction

This paper describes an equipment-free method for generating positive and negative pressures in a microfluidic device using a pumping lid. Most of the microfluidic devices developed in the past two decades rely on external equipment for operation, including the use of pumps, gas cylinders or other external controllers[1-5] for precise pumping and loading. Achieving the same degree of flow control without expensive or bulky equipment is necessary for making microfluidic devices more accessible. Currently, equipment-free pumping is both a challenging problem and an active area of research, with several proposed approaches.[6-15] For applications in which the total sample volume is less than the internal volume of the device, the sample's surface energy is known and stable flow rate isn't required, capillary-based pumping (wicking) can be used.[6-10] This has been done by flowing samples through microchannels[9,10] or using fibrous materials, such as paper.[6-8] For cases when the device can be pre-loaded with a solution, and the solution's surface energy is known, the flow of the solution can be driven by the difference in capillary pressure between droplets of different sizes of this solution placed at the inlet and outlet of the device. For this method the pressure difference can be restored constantly by the addition of solution to the smaller droplet.[11,12] When only small sample volumes are used (a few microliters or less) and the application does not require flow rates greater than a few nanoliters per second, pre-degassed microfluidic devices can be used to generate flow.[13,14] Finally, when the density and volume of the sample are known, and the device can be stabilized in a precisely horizontal position, gravity can generate predictable pressure drops and drive the flow in a microfluidic device. In this approach, the difference in height of fluid in separate reservoirs generates the desired pressure drop.[15] These methods have wide-ranging applications, but none can provide precise and predictable control of pumping in the absence of external equipment, independent of the sample's volume, surface energy and density, while still achieving a wide range of flow rates.

Here we describe the theory, characterize the method, and validate the design of a range of equipment-free pumping lids for controlled-pressure generation in microfluidic applications. This pressure generation approach is based on controlled gas expansion or compression, so it does not depend on the nature of the liquid being pumped, the geometry of the channels, or the device's

orientation. It can also be coupled with evaporation of a volatile liquid to generate pressure. Development and characterization of this method was enabled by multi-material 3D printing which allows fast prototyping of composite parts that have sections with different mechanical properties. In addition, the pumping lid approach has the following beneficial features that have not been combined previously in a single method:

a) The same setup can pump liquids of different density and/or surface energy with no difference in the resulting flow rate.
b) The pressure source is integrated with the device, so the method does not require the use of external connectors or tubing.
c) A simple model can be used to predict the pressure/flow rate generated by a specific lid/cup combination.
d) Pumping lids are interchangeable, so the same microfluidic device can be used with different lids to generate different flow rates. Pressures can be tuned by choosing the pumping lid with the appropriate dimensions and/or by modifying the lid's geometry.
e) The user can alter the pressure by simply changing the position of the pumping lid, without interrupting the experiment.
f) Flow rates can be tuned precisely, with values ranging from a few nanoliters to more than a microliter per second, and remain consistent for long periods (hours in some cases).
g) The sample volume pumped can be larger than the internal volume of the device, making the method appropriate for handling samples that range from a few microliters to milliliters.
h) Both positive and negative pressures can be produced in predictable ways and used to generate and control flow.
i) While pumping is in progress, the lid keeps the sample isolated from the external environment, preventing contamination and evaporation.
j) The combined weight of all parts is less than 50 g, making it portable.
k) The device can be made of low-cost, disposable/recyclable polymeric materials, making it adaptable to resource-limited settings.

Results and discussion

Principle of pumping lid operation

The pumping lid method described in this paper is based on controlled compression or expansion of gas (Figure 2.1). To generate positive pressure, the user places the sample at the device inlet and then places the pumping lid on the cup integrated into the microfluidic device (Figure 2.1A). When the user pushes the lid down to its final position, the air in the lid's cavity is isolated and compressed, creating positive-gauge pressure. The lid's position is held by friction, but to increase robustness, guiding and locking structures can be integrated into the design (Figure 2.1A-B). Conversely, to create negative pressure, a pumping lid is pre-placed on the cup (Figure 2.1B) and the user pulls up on the pumping lid, expanding the air in the cavity. The degree of expansion is controlled by guiding structures.

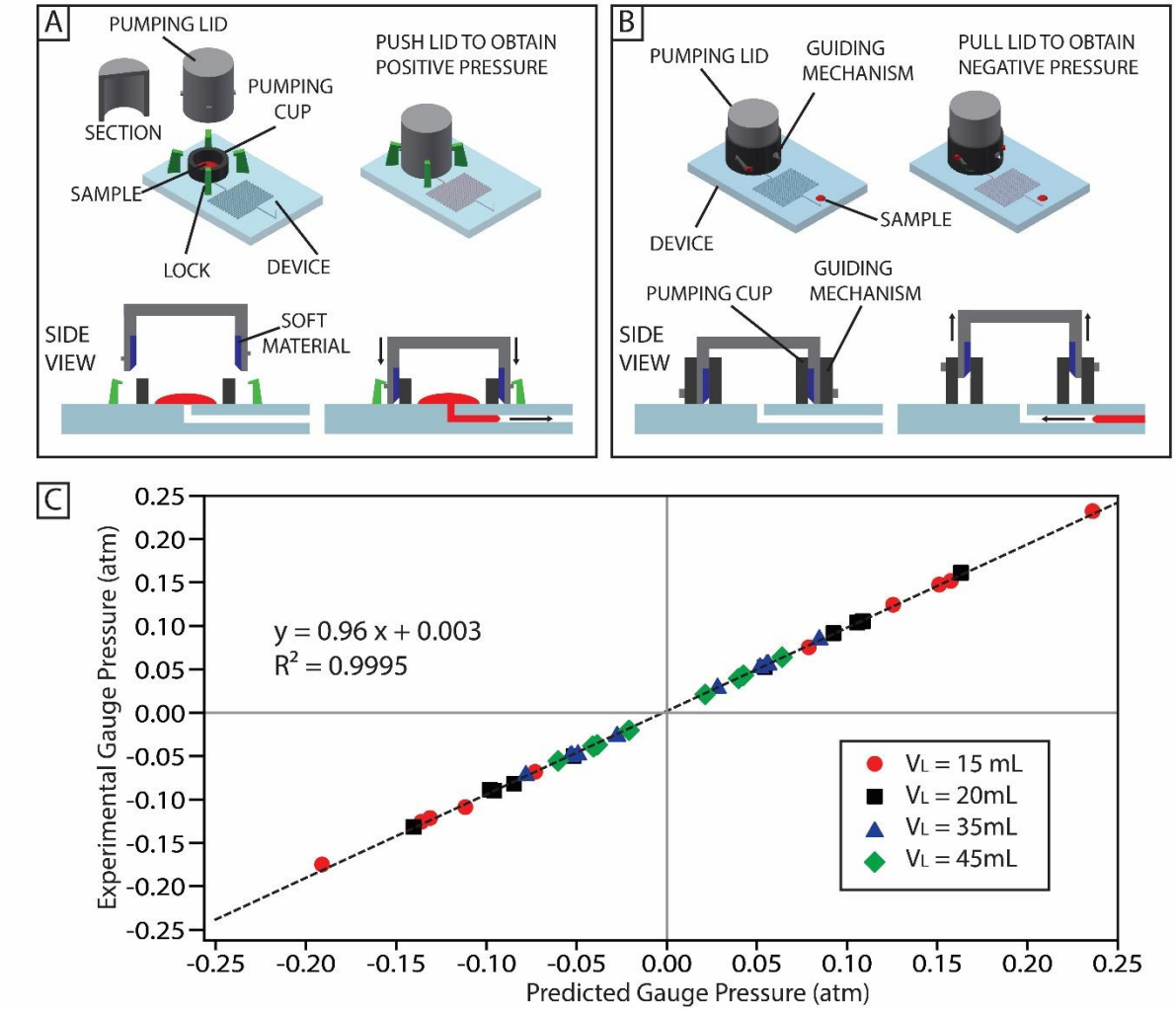

Figure 2.1 Principle of pumping lid operation. (A) Schematic of the method to generate positive pressure. A device is equipped with a cup (black) and locks (green). A sample (red) is placed in the cup before pumping. The pumping lid (grey) contains a cavity as shown in the side view. Part of the pumping lid is composed of a soft, deformable material (blue). Placing the lid on the cup compresses the air in the cavity and generates the pressure used to pump the sample in the device. The locks hold the lid in place to maintain the pressure over time. (B) Schematic of the method to generate negative pressure. The pumping lid (grey) is placed on the inner cup (black, visible only in the side view) before the experiment, and is equipped with guiding pins (red). These pins slide on a guiding structure (black) to guide the movement of the lid. When the user pulls the lid, the air in the cavity expands, creating a negative gauge pressure that pumps the sample into the device. (C) Pressures obtained from 40 experimental cup-lid combinations (N=3) plotted against the pressure values

obtained from the model (Eq. 2.2 and Eq. 2.6). The colors denote lids of different cavity volumes. The dashed black line indicates the linear fit of the data and its parameters are reported in the graph.

Theoretical model for prediction of the pressure generated with the pumping lid

First, we analyze the initial pressure generated by the pumping lid and cup, prior to pumping. We use the Boyle law for isothermal gas compression: $P_0V_0 = P_1V_1$; assumptions of ideal gas behavior are appropriate in this case because the pressures are low (~ 1 atm) and the temperatures are sufficiently high (~ 300K).

Positive pressures

The positive pumping pressure depends on four main parameters: the volume of the cavity in the pumping lid (V_L), the volume of the cup walls (V_W), the volume of the empty space inside the cup (V_C), and the volume of sample loaded in the cup (V_S). When the lid is placed on the cup and first creates the seal, the volume of air enclosed is defined as $V_0 = V_L + V_C - V_S$, and the initial pressure is P_0 ~1 atm (Figure S2.1, Option 1). After the user pushes down the lid, the air is compressed and the final volume is given by $V_1 = V_L - V_W - V_S$. Applying Boyle's law, the pressure at this point is calculated as follows:

$$P_1 = \frac{P_O\,(V_L + V_C - V_S)}{(V_L - V_S - V_W)} = P_O + \frac{P_O\,(V_W + V_C)}{(V_L - V_S - V_W)} \qquad \text{(Eq. 2.1)}$$

A more generalized formula can be used for the case when the lid is already pre-placed on the cup, at a distance d from the final position (Figure S2.1, Option 2). The pressure is generated when the user pushes the lid to the final position. In this case, the pressure depends on the four volumes described above (V_L, V_C and V_S, V_W) and on the ratio x, between d and the total height of the cup (h), defined as $x = d/h$. The initial volume in this case is given by $V_0 = V_L - (1 - x)\,V_W + x\,V_C - V_S$ and the initial pressure is again, the atmospheric pressure, P_0 ~ 1 atm. After the lid has been pushed down by a distance d, the final volume is given by $V_1 = V_L - V_W - V_S$. The pressure at this point is calculated by using the same relation, $P_0V_0 = P_1V_1$, and is defined as:

$$P_1 = \frac{P_O\,[V_L + \mathrm{x}\,V_C - (1-\mathrm{x})V_W - V_S^0]}{V_L - V_W - V_S^0} = P_O + \frac{P_O\ \mathrm{x}(V_W + V_C)}{V_L - V_W - V_S^0} \quad \text{(Eq. 2.2)}$$

V_S^0 defines the initial sample volume.

Second, we analyzed changes in pressure due to pumping. The pressure as a function of time is expressed as:

$$P_1(t) = \frac{P_O\,[V_L + \mathrm{x}\,V_C - (1-\mathrm{x})V_W - V_S^0]}{V_L - V_W - V_S(t)} \quad \text{(Eq. 2.3)}$$

$V_S(t)$ defines the volume of sample present in the cup at time t. When the sample volume is substantially smaller than the difference between the cavity and pumping cup volumes, $V_L - V_W$, the change in the only time-dependent term, $V_S(t)$, becomes negligible and the pressure can be considered constant, and Eq. 2.3 becomes identical to Eq. 2.2. This assumption was verified in all the experiments described in this paper, unless otherwise stated. Eq. 2.3 can be used to guide the design of pumping lids and cups, to predict the variation in pressure due to pumping and tune it, if needed.

When the sample volume is large enough to affect the pressure, the following set of equations can be used to describe the change in pressure. Given the hydraulic resistance (R_H) of the device, the time-resolved drop in positive pressure can be calculated as the sample is pumped out of the cup:

$$P_1(t) = \frac{P_0\left(V_L - (1-x)V_W + xV_C - V_S^0\right)}{\sqrt{(V_L - V_W)^2 + 2\left(\frac{P_0 t}{R_H}\left(V_L - (1-x)V_W + xV_C - V_S^0\right) - V_S^0\left(V_L - V_W - \frac{V_S^0}{2}\right)\right)}} \quad \text{(Eq. 2.4)}$$

Eq. 2.4 is only valid for $P_1 \geq P_0$ and while pumping is in progress. We assumed that the values of R_H remained constant in our experiments, because we pre-filled the channels with the solution being pumped. If the channel is not pre-filled, the initial variation of R_H during filling would need to be accounted for. To calculate the time required to pump the whole sample volume, the following equation is used:

$$t^* = \frac{\left(V_L - V_W - \frac{V_S^0}{2}\right)V_S^0}{\frac{P_0}{R_H}\left(V_L - (1-x)V_W + xV_C - V_S^0\right)} \quad \text{(Eq. 2.5)}$$

Eq. 2.5 relies on the same assumptions as Eq. 2.4.

Negative pressures

For generation of negative gauge pressures, the pumping lid is pre-placed onto the cup, and the user pulls it by a distance d. Assuming the cup is empty prior to pumping, the initial volume is given by $V_0 = V_L - V_W$. The initial pressure is the atmospheric pressure, P_0 ~1 atm. If the channel is not pre-filled with solution prior to pumping, the channel volume needs to be accounted for in V_0. After the lid has been pulled by a length d, the final volume of air is given by $V_1 = V_L + x\,V_C - (1-x)\,V_W$. Using previously defined parameters and the relation $P_0V_0 = P_1V_1$, the pressure at this point is defined as:

$$P_1 = \frac{P_O\,(V_L - V_W)}{V_L + \mathrm{x}\,V_C - (1-\mathrm{x})V_W} = P_O - \frac{P_O\ \mathrm{x}(V_W + V_C)}{V_L + \mathrm{x}\,V_C - (1-\mathrm{x})V_W} \quad \text{(Eq. 2.6)}$$

Similarly to the case of the positive pressure, once pumping commences, the time dependence of P_1 is given by the expression:

$$P_1(t) = \frac{P_O\,(V_L - V_W)}{V_L + \mathrm{x}\,V_C - (1-\mathrm{x})V_W - V_S(t)} \quad \text{(Eq. 2.7)}$$

$V_S(t)$ represents the volume of sample pumped into the cup at a given time t. When the sample volume is much smaller than $V_L + \mathrm{x}\,V_C - (1-\mathrm{x})V_W$, the only time dependent term in Eq. 2.7, $V_S(t)$, becomes negligible and the pressure can be considered constant. Whenever this assumption cannot be made, one can calculate the time-resolved drop in pressure as the sample is pumped into the cup, given the hydraulic resistance (R_H) of the device:

$$P_1(t) = \frac{P_0(V_L - V_W)}{\sqrt{(V_L - (1-x)V_W + xV_C)^2 - 2\frac{P_0 t}{R_H}(V_L - V_W)}} \quad \text{(Eq. 2.8)}$$

Eq. 2.8 is only valid for $P_1 \leq P_0$ and while pumping is in progress. To calculate the time required to pump a given sample volume one should use the following equation:

$$t^* = \frac{\left(V_L + xV_C - (1-x)V_W - \frac{V_S^f}{2}\right)V_S^f}{(V_L - V_W)} \cdot \frac{R_H}{P_0} \qquad \text{(Eq. 2.9)}$$

V_S^f represents the total sample volume to be pumped into the cup.

Generation of predictable positive and negative pressures

We experimentally tested (Figure 2.1C) predictions of the model for generating both positive (Figure 2.1A) and negative (Figure 2.1B) gauge pressures. We report (Figure 2.1C) the pressures obtained from 40 combinations of cups and pumping lids, plotted against the pressure value predicted by Eq. 2.2 and Eq. 2.6. Cups were 3D-printed directly on a rigid support and not connected to a device. We used a 5 psi differential pressure sensor (PXCPC-005DV, Omega Engineering), which was connected to a power supply (Portrans FS-02512-1M, 12V, 2.1 Amp power supply, Jameco Electronics) and to a data acquisition board (OMB-DAQ-2408, Omega Engineering). A custom program was written in LabVIEW (National Instruments) to convert the signal collected by the sensor to gauge pressure. The sampling frequency was 2 Hz. Each condition varied in at least one model parameter (V_L: 14.7 mL − 44.8 mL; V_C: 0 − 2.7 mL; V_W: 0.8 µL − 3.6 µL; x: 0.25 − 0.75). The pumping lids used for these experiments included a nozzle that could be connected to the positive side of the pressure sensor using a short piece of Tygon tubing (1 cm long). Lid volumes were calculated using CAD software, accounting for the extra volume introduced by the nozzle, tubing, and the sensor. The other side of the sensor was exposed to the external environment, so all data collected were in terms of gauge pressure. The results were a close match to the predicted outcome, with an R^2 value of 0.9995 and a slope of 0.96. The pressures produced in this experiment spanned more than an order of magnitude (Table TS2.1). Furthermore, the model predicts that even higher pressure could be obtained by decreasing the volume of the empty parts (V_L, V_C) and/or by increasing the other volumes (V_W and V_S).

Design guidelines for the pumping lid and cup

We found three guidelines to be helpful in designing pumping lids and cups: (1) the model can be used to either predict the pressure generated by a particular lid/cup combination, or to determine the lid and cup dimensions needed to achieve a particular pressure. All parameters can be tuned and the resulting pressure for each combination can be predicted using the equations described in the previous section. (2) To ensure effective sealing between the pumping lid and the cup, at least one of the two parts (lid or cup) should contain a deformable (soft) portion. The design requires a small overlap between the parts, so the soft portion is forced to deform when the lid is placed on the cup, thus creating a hermetic seal. Typical overlaps were in the order of 100 µm to 200 µm, which corresponds to ~ 1-2% of the cup diameter. We used multi-material 3D printing provided by Objet 260 system (Stratasys, Eden Prairie, MN, USA), which can produce parts composed of two different materials, and mixtures of these two materials. (3) Compression deforms the soft portion of the lid, and the material tends to be squeezed laterally. We observed that if this deformed material goes between the pumping lid and the base of the cup, the lid cannot be pushed to its final position and the obtained pressure will be lower than the one predicted by the model. This effect can be minimized by ensuring that the thickness of the soft layer is significantly larger than the overlap between the lid and cup, typically in the order of 1-1.5 mm. Another solution is to use soft layers with a tapered profile (Figure 2.1A).

Controlled pressure variation during an experiment

Next, we wished to test whether it would be possible to switch the pressure applied by the pumping lid without interrupting the flow or exposing the sample to the environment (to minimize contamination or evaporation). This capability is desired when several flow rates need to be tested in one continuous experiment. Pressure is changed by compressing or expanding air in the cavity. Therefore, here we investigated whether the level of compression or expansion, and therefore the pressure, can be controlled precisely by using the guiding structures (Figure 2.2). For example, for both positive- and negative-gauge pressures, we designed lids that can be placed in three positions, labeled (a), (b), and (c). Each position provides a defined, specific pressure, and the user can switch between the positions by rotating the lid on its axis (Figures 2.2D, 2.2H). The lids for these

experiments were 3D-printed with a nozzle for the pressure sensor and pressure data was collected with the same setup as described in previous sections. For both positive- and negative-pressure devices, the starting position, (a), corresponds to zero gauge pressure (Figure 2.2). This adjustable design thus enables customized, "pre-programmed" pressure control during an experiment (e.g. to initiate or stop flow, and to change the flow rate) and allows the fully assembled device to be stored without applying pressure before use. While the devices demonstrated here are able to produce three specific pressures, more lid positions can be designed to enable finer tuning.

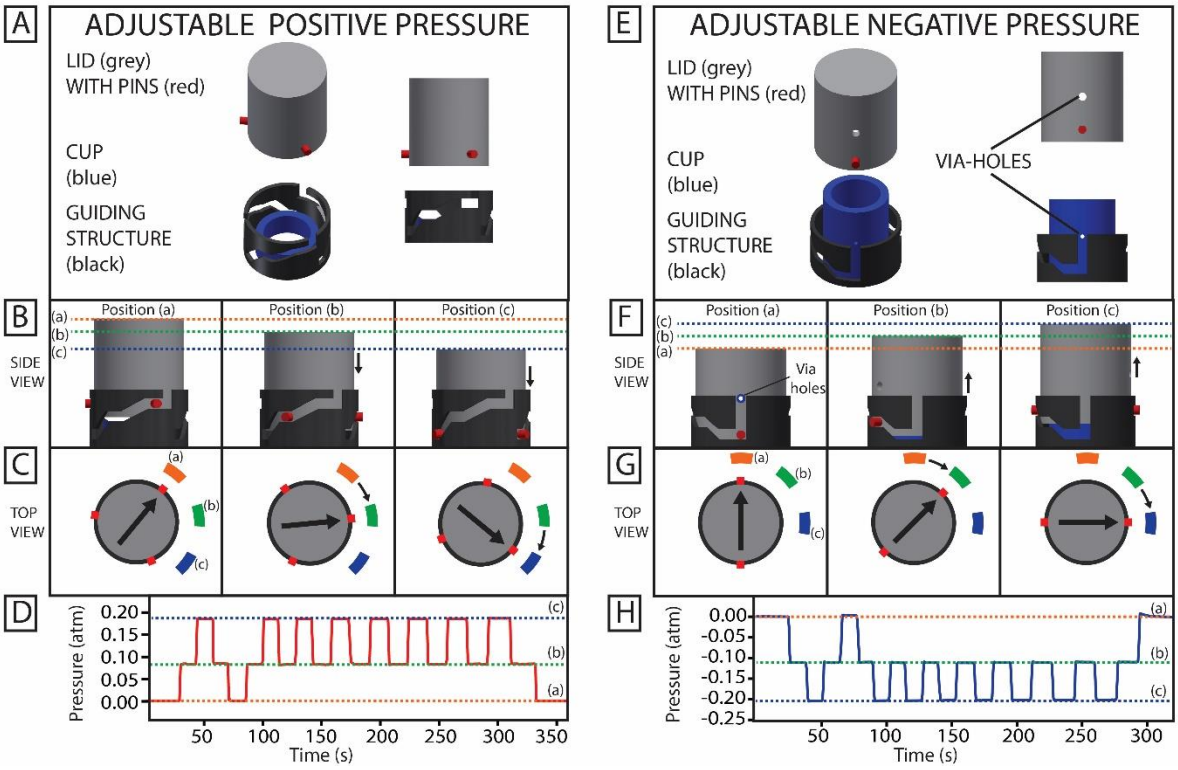

Figure 2.2 Strategies for producing multiple pressure values in a single device using a cup and pumping lid. (A-D) Positive pressures produced by turning a pumping lid (grey) using a cup (blue) fit with a guiding structure (black) (A). Turning the lid within the guiding structure yields three potential lid positions, which are shown in side (B) and top (C) views, each of which produces a different pressure. In Position (a), the lid is not in contact with the cup, so no pressure is produced. In Position (b), the lid is lowered and positive pressure is produced. In Position (c), the lid is lowered further, and the pressure increases. The horizontal dashed lines show the level of the lid in the three

positions. Panel D shows an experimental pressure profile obtained by turning the lid between the three positions. (E-H) Negative pressures produced by turning a pumping lid (grey), using a cup (blue) fit with a guiding structure (black) (E). Turning the guiding structure yields three potential lid positions, which are shown in side (F) and top (G) views, each of which produce a different pressure. The pumping lid and the cup have via-holes that align only in Position (a), so there is no gauge pressure in this configuration. In Position (b), the lid is raised and negative pressure is produced. In Position (c), the lid is raised further, and the pressure decreases. The horizontal dashed lines show the level of the lid in the three positions. Panel H shows an experimental pressure profile obtained by turning the lid between the three positions.

Generation of flow using the pumping lid approach

Next, we tested the prediction that for a given channel geometry, the pumping lid method would provide consistent flow rate that depends on viscosity, but not on surface energy or density of the fluid being pumped. We used Eq. 2.1 to predict the pressure applied by the pumping lid, and Eq. 2.10 to predict hydraulic resistance R_H that depends on the viscosity and the dimensions of the channel.[16]

$$R_H = \frac{12\mu L}{h^3 w\left(1-0.63\left(\frac{h}{w}\right)\right)} \quad \text{(Eq. 2.10)}$$

L defines the channel length, h the channel height, and w the width of the channel. The volumetric flow rate can thus be predicted with Eq. 2.11:

$$Q = \frac{P}{R_H} = \frac{Ph^3 w\left(1-0.63\left(\frac{h}{w}\right)\right)}{12\mu L} \quad \text{(Eq. 2.11)}$$

To test these predictions, we first characterized pumping of water through a microfluidic device using seven pumping lids, each providing a different pressure (Figure 2.3A). The device consisted of glass-bonded PDMS layer[17], pumping cup, PTFE tubing, and the pumping lid (Figure S2.3). A

30.8 cm long, 58 µm high, 110 µm wide serpentine was molded into the PDMS layer, and was pre-filled with each solution prior to pumping experiment, as described in SI. The slope of the fitting curve is the inverse of the hydraulic resistance (R_H) for the experimental setup, as suggested by Eq. 2.11.

The experimental value for R_H obtained from the fit is 2.59*10^{14} Pa s /m^3, which matched the theoretical value calculated for the microfluidic channel geometry: 2.58*10^{14} Pa s /m^3.[16] Thus, it was possible to predict the flow rate for a given pumping lid used with a given microfluidic device, and the design was robust enough to give reproducible results. The flow rates in this experiment were 1 – 5 µL/min, and this range was chosen to minimize the experimental errors when measuring flowing time. Higher flow rates could be produced by increasing the pressure generated by the pumping lid (as described in the previous sections), or by using a device with lower hydraulic resistance. For example, a device with a channel 150 µm tall x 150 µm wide x 20 mm long will have a hydraulic resistance almost 200 times less than the devices used for these experiments, so the flow rate generated with the same pumping lids would approach 1 mL/min.

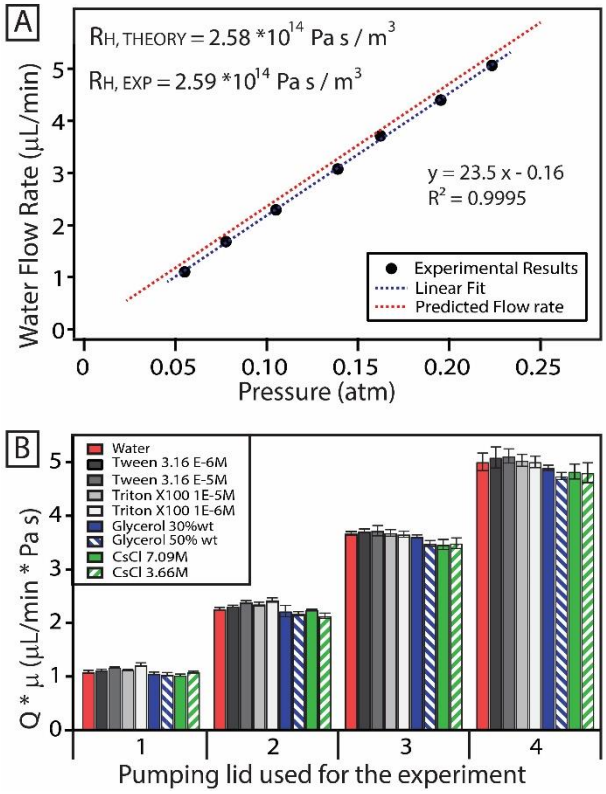

Figure 2.3 Experimentally and quantitatively testing the model describing pumping with a pumping lid as a function of hydraulic resistance of the channel and properties of the fluid. (A) Flow rate of water in a microfluidic device using different pumping lids to generate different pressures. The dotted red line indicates the predicted flow rate based on the device geometry, while the dotted blue line shows the linear fit of the data; its parameters are reported on the graph (N=3; error bars smaller than the size of the marker). (B) A plot of experimental flow rates, multiplied by the viscosity, for different aqueous solutions. Flow rates were inversely proportional to viscosity and independent of the surface energy or density of the solutions. Schematics of the setup used for these experiments are provided in the supplementary material. (Figure S2.3).

Generation of flow rate independent of density and surface energy

To verify that the flow rate in the pumping lid method is independent of solution density and surface energy, we pumped nine aqueous solutions of different properties (Table TS2.2) using seven different lids to measure the flow rate at different inlet pressures. Solutions of viscosity similar to water, but with different surface energies (30 – 72 mN/m) and different densities (1 – 1.9 g/mL), had flow rates comparable to those obtained for water. We experimentally measured viscosities of all nine solutions to confirm this result. Note that the viscosity-adjusted flow rate values ($Q \cdot \mu$) were similar for all liquids (Figure 2.3B), which is explained in the next section.

Generation of flow for solutions of different viscosities

We then tested whether the pumping lid is appropriate to produce flow in solutions with viscosities higher than that of water. In our experiments, solutions had viscosities between 1 mPa*s and 4 mPa*s (Figure 2.3B). The flow rates for high viscosity solutions were lower than those obtained for pure water, because the value of the hydraulic resistance R_H described above is directly proportional to the viscosity of the liquid pumped (Eq. 2.10)[16]. Eq. 2.11 can be re-written as:

$$Q \cdot \mu = \frac{Ph^3w\left(1-0.63\left(\frac{h}{w}\right)\right)}{12L} \qquad \text{(Eq. 2.12)}$$

Eq. 2.12 predicts that, if the same lid-cup combination is used on the same device, the product of the flow rate and the viscosity of the solution will be constant.[16] Our experimental results (Figure 2.3B) corroborated this prediction, since the $\mu \cdot Q$ values for all the solutions analyzed were comparable to those obtained for water (Figure 2.3B). This means that the pressure generated by a pumping lid depended solely on the lid-cup dimensions, and not on the nature of the solution to be pumped.

Use of multiple lids on the same device to achieve complex flow control over long timescales

Next, we tested the idea that using separate cups and lids at different inlets makes it possible to simultaneously pump more than one solution and to independently control the pressure imposed at each inlet (Figure 2.4A). First, we used multiple lids to produce nanoliter droplets (Figure 2.4B).[18-20] Immiscible fluids can be difficult to handle under pressure-driven flow because the applied pressure should be higher than capillary pressure but not so high to generate an excessive capillary number that would cause droplet deformation[21]. Also, when multiple inlets are controlled with different pressures, liquid could potentially flow from one cup to another. To avoid this, we designed devices with geometries that included a serpentine channel between the inlets and the junction used to produce the droplets. This serpentine channel had a fluidic resistance higher than that of the outlet channel, and ensured that liquids were not transferred from one cup to the other during experiments. This approach was used to generate nanoliter droplets (plugs) of water in fluorinated oil, using flow focusing and T-junction geometries (Figure 2.4B), with volumes that ranged from 0.5 to 2.5 nL.

Parallel laminar flow profiles can also be produced (Figure 2.4C). We achieved stable flow patterns for more than 2.5 h, with a total pumped amount of 0.9 mL. The predicted decrease of flow rate in this system over a 2.5 h period was 45% of the original value (Eq. 2.4), which was consistent with our experimental observations (Figure 2.4C). Increased diffusion between the dyes was observed, due to the longer residence time in the channel. Because we used lids of the same size and loaded samples of the same volume and viscosity, over time we observed a decrease in the absolute value of the flow rates, but not a decrease in their ratios. We emphasize that if the volumes of the lids, cups, sample volumes and/or viscosities are different, the flow rates will drop at different rates (Eq. 2.4).

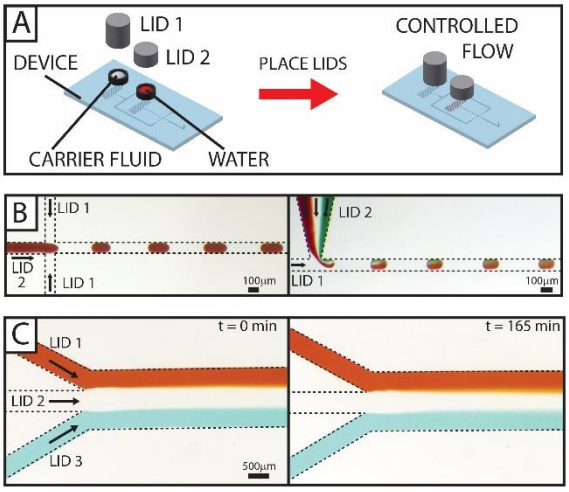

Figure 2.4 Use of the pumping lid approach to control pumping of each of several fluids with different properties in a microfluidic device. (A) Schematic of the pumping approach using multiple solutions in the same device. Each sample was pumped in the device with a different pumping lid, each lid producing a different pressure. (B) Left: Experimental photographs illustrating production of nanoliter plugs (red) in fluorinated oil (transparent), using a microfluidic device with flow focusing geometry. Right: Production of multicomponent aqueous droplets in fluorinated oil using a T-junction. The solutions (red, transparent and green) were pumped independently and used to produce nanoliter plugs. (C) Experimental photographs illustrating that the parallel laminar flow profile of three separate streams of aqueous solution (red, transparent and light blue) was stable even after 165 min (2.75 h). A total volume of 0.9 mL (300 µL of each solution) was pumped in this experiment.

Use of composite lids to produce different flow patterns in the same device

A "composite lid," a pumping lid with multiple cavities, was designed to simultaneously seal multiple cups (Figure 2.5). The cavities in the composite lid can be isolated or connected to one another. For example, if inlets require identical pressures, their corresponding cavities can be linked (Figure 2.5C).

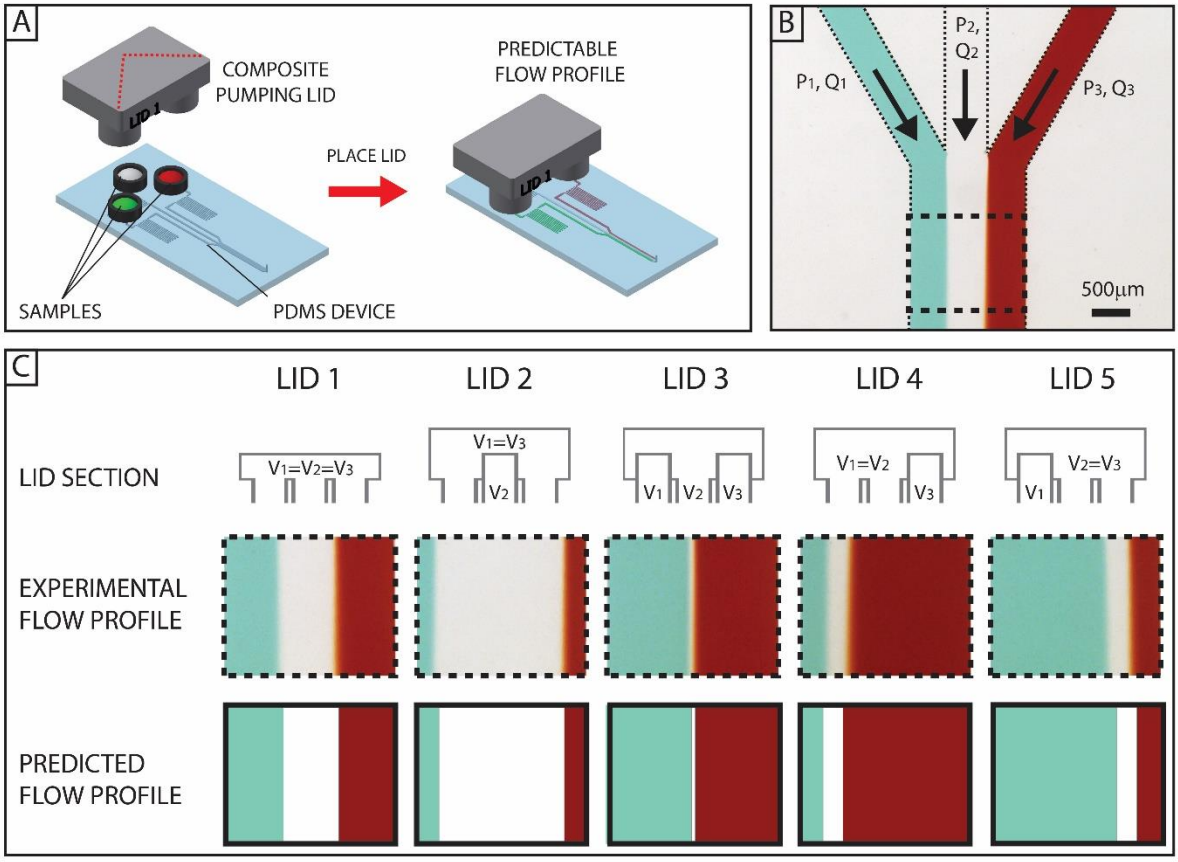

Figure 2.5 Production of different flow profiles in the same device using composite pumping lids. (A) Schematics of the setup used for the experiments. The microfluidic device has three cups, each dedicated to a different aqueous solution (from left to right: green, transparent, and red). A composite lid controls the pressure at each of the three inlets, thus controlling the flow rate of each solution. (B) Micrograph of the junction at which the three inlet branches combine into a single channel and the streams from the three inlets produce parallel laminar flow. (C) Different composite lids can be used to produce different flow profiles. The top row shows the cross-section of five different lids, cut along the red dashed line in panel A. The middle row shows the experimental flow profiles obtained with these five lids in the same microfluidic device. The sketches (bottom row) show the expected flow profiles based on the pressures produced by the lids and the device geometry. For the channel used in these experiments, the width (1.5 mm) was more than 35 times bigger than the channel height (40 µm), so the effect of parabolic flow near the lateral walls was negligible.[16]

To test these devices quantitatively, we measured the width of each solution stream in the three-stream aqueous laminar flow, (the Reynolds number was always less than 1 in our experiments). The gauge pressures at the three inlets are defined as P_1, P_2, and P_3, while the pressure at the device outlet is zero. Fluidic resistances for the three inlet branches (before the junction) are defined as R, while the resistance of the main channel (formed by the junction of the three inlet branches) is defined as r. In the experiments described in this paper, the fluidic resistance R of the inlet branches was intentionally set larger than the outlet resistance r, to increase the range of pressures that could be applied to the three inlets without generating back-flow in the branch with the lowest pressure. Under these conditions, theory predicts that Q_i is proportional to P_i and can be approximated by Eq. 2.11. Ignoring the effects of three-dimensional diffusion[22,23] and ignoring the effect of the parabolic flow profile for these wide channels, we predicted the flow profiles as described in the supplementary material, and found them to be in good agreement with experiments.

These lids were used to produce parallel laminar flow profiles in a microfluidic device (Figure 2.5B). Each composite lid had a different geometry (Figure 2.5C) and generated a different set of pressures at the three device inlets. These pressures were used to predict the flow profile in the microfluidic device, as described in the supplementary material, and experimental results matched the flow profiles predicted by the flow rate model (Figure 2.5C). Based on the geometries of the device and the composite pumping lid, flow profiles can be controlled and predicted.

Use of pumping lids to load SlipChip devices by positive and negative pressures

Next, we showed that the pumping lid could be used to reliably and easily load SlipChip devices[24] using either positive or negative pressures. This is a good test because loading SlipChip devices requires control of the inlet pressure within a defined range,[25] and SlipChips are intended to be used in limited resource settings (LRS) by untrained users.[26-29] First, we tested the pumping lid on a SlipChip designed for a digital nucleic acid detection assay[26] (Figure 2.6A), pumping a total of 5 μL of solution with 0.03 atm pressure (Eq. 2.1). We asked a 6-year-old volunteer to use the pumping lid to operate the device. We found that pumping proceeded to completion despite the variation of

pressure applied to the pumping lid by the volunteer.[30,31] We expect the simplicity of the pumping lid to be valuable in both LRS and laboratory settings, e.g. for digital single-molecule measurements.[31]

In another experiment, we tested loading of a different SlipChip device by negative pressure. To further illustrate the applicability of the pumping lid method to complex tests, we used a SlipChip designed for multivolume digital nucleic acid amplification,[32,33] which presents challenges in filling due to variation of capillary pressure among wells of different sizes. Previously, this type of device was filled by positive pressure and dead end filling.[25] We modified the device for negative-pressure filling by adding a sealing ring filled with high-vacuum grease (sealing structure) around the active area containing the amplification wells (Figure 2.6B). We also added an outlet for oil to the device, over which the negative-pressure pumping lid was placed. The device was assembled such that the lubricating oil (5 cSt silicone oil) was filling the wells. For loading, sample (50 µL of 0.5 M FeSCN aqueous solution) was placed onto the inlet, and the pumping lid was pulled up to create negative pressure of 0.1 atm, remove excess oil and draw the sample into all of the wells of the device (Figure 2.6B). This experiment demonstrated that bubble-free filling can be accomplished using the pumping lid, and that complex devices (a combination of immiscible fluids and wells with different capillary pressures) can be handled.

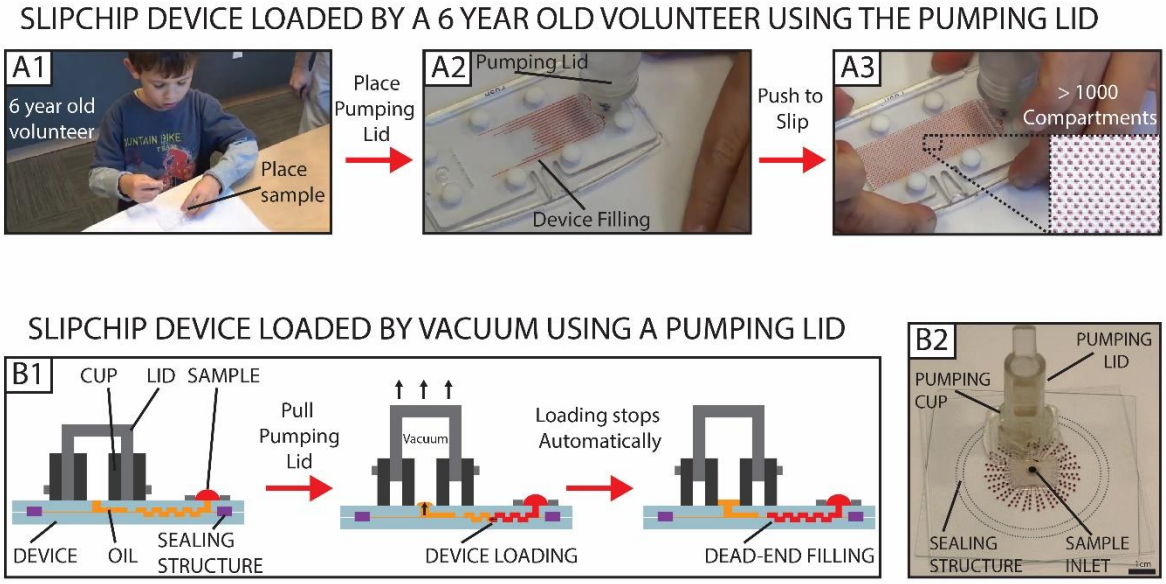

Figure 2.6 Use of the pumping lid for loading of SlipChip devices. (A) Photographs of a 6-year-old volunteer with minimal training using the pumping lid to load a SlipChip device. The sample is placed in the cup at the device inlet (A1), the pumping lid is placed on the cup, and when the lid is pushed, positive pressure is generated and sample pumping starts (A2). Once the sample loading is complete, slipping two plates generates discrete compartments (A3). A video of this experiment is provided.[30] (B) SlipChip sample loading by negative pressure. (B1) Schematic outline of the steps. The lid is pre-placed on the cup, and the sample is placed at a separate inlet in the device. Pulling the lid creates negative gauge pressure and initiates loading. Dead-end filling ensures that the loading stops once the device is completely filled. (B2) Photograph of a multivolume SlipChip device for digital nucleic acid quantification loaded with negative pressure pumping lid method.

Vapor-liquid equilibrium (VLE) method for pressure generation

We then explored how vapor pressure of a volatile liquid can aid the pumping process by isolating its effect from compression, and investigated the potential to harness the vapor pressure for pumping a non-volatile sample. Our hypotheses were that (i) by taking advantage of vapor-liquid equilibrium (VLE), one would be able to pump large volumes of liquid over extended periods of time at a relatively constant pressure, without the need to compress a large volume of a gas inside the device; (ii) a single lid design could be used to generate different pressures by using liquids of different vapor pressure; (iii) a single combination of a lid design and a volatile liquid could be used to generate different pressures by tuning the temperature. In this approach, a volatile liquid is stored in a sealed compartment inside a pre-assembled vapor pressure pump, comprised of a lid and cup (Figure 2.7A). The design of this lid and cup differ from those described previously, as turning this lid connects or disconnects the compartments in the cup, rather than compressing or expanding the gas enclosed in the cavity, as in a SlipChip device.[24] In addition, the cup is divided to contain the volatile liquid and one or more separate sample compartments. When the user turns the lid, the volatile liquid evaporates into the cavity (Figure 2.7B). The cavity in the pumping lid is isolated from the atmosphere, so evaporation of the volatile liquid increases the pressure in the cavity. Once the volatile liquid reaches equilibrium with its vapor, the pressure will be higher than the atmospheric pressure, and its value

can be calculated using the thermodynamic VLE model. The user can initiate pumping by opening a valve or removing a plug. During pumping, evaporation of additional liquid provides additional pressure, although there is a drop in pressure, since the volume previously occupied by sample is now available to the gas phase, effectively causing expansion. Similarly to the pressure change observed in the pumping lid method, this pressure drop can often be neglected, if the sample volume being pumped is much smaller than the pump gas compartment volume. Once the entire sample has been pumped through the device, the vapor in the lid connects to the atmosphere and the gauge pressure drops to zero. This method of vapor pressure pumping can be used independently or in conjunction with compression.

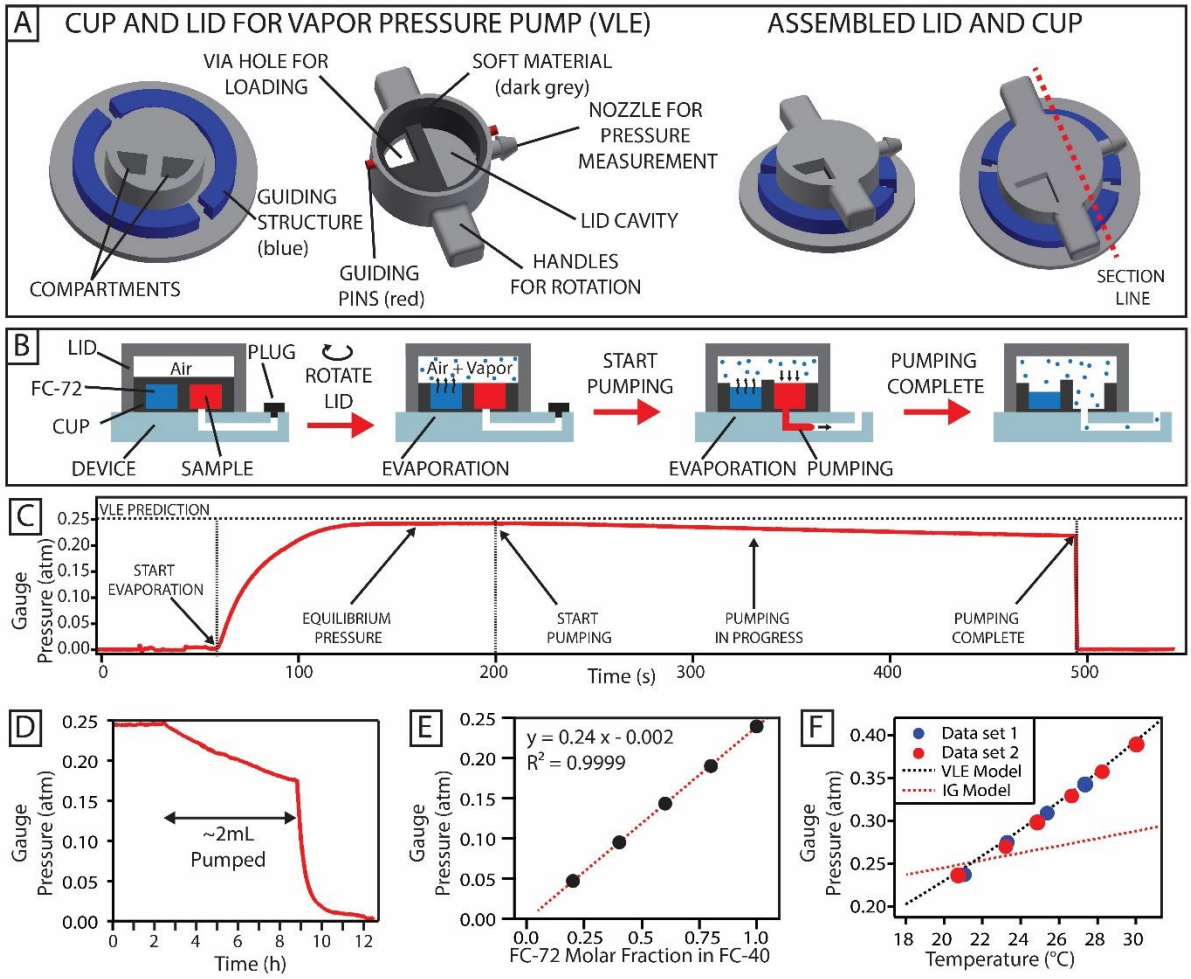

Figure 2.7 Generation of pressure using vapor liquid equilibrium (VLE). (A) Schematics of the parts used for VLE pressure generation. (B) Schematics of the method used to generate pressure.

The figures show the cross section of the lid and cup assembly along the red line shown in panel A. Prior to the experiment, a volatile liquid (FC-72, blue) and the sample (red) are placed in isolated compartments of the cup. At this stage, the pressure in the lid cavity is equilibrated with the atmosphere. When the lid is rotated, the volatile liquid is exposed to the air in the cavity and starts to evaporate to reach its equilibrium pressure. When the plug is removed from the device outlet, the sample starts flowing. After the entire sample has been pumped, the cavity is in contact with the external atmosphere and the pressure returns to zero. (C) An experimental pressure profile obtained by performing the steps described in panel B, for pumping 20 µL of water. (D) Pressure profile obtained when pumping a 2 mL sample volume through a microfluidic device. (E) Equilibrium pressures obtained by using mixtures of liquids (FC-72 and FC-40) at different molar fractions (N=3; error bars smaller than the size of the marker). The dashed line indicates the linear fit of the data and its parameters are reported in the graph. (F) Equilibrium pressure obtained using FC-72 at different temperatures. The dashed line shows the values predicted by the VLE model (Eq. 2.16). Each point represents the average over at least 62 and up to 87811 pressure measurements after the system has equilibrated.

Model for VLE pressure generation using perfluorohexane (FC-72)

To find the predicted pressure at VLE, the fugacities of perfluorohexane in both liquid (right hand side in Eq. 2.13) and gas (left hand side in Eq. 2.13) phases are set equal. The general expression for VLE is:

$$\hat{\phi}_{FC} y_{FC} P = \gamma_{FC} x_{FC} \phi_{FC}^{sat} P_{FC}^{sat} \exp\left[\frac{V_{FC}^{L}(P - P_{FC}^{sat})}{RT}\right] \quad \text{(Eq. 2.13)}$$

where:

$\hat{\phi}_{FC}$ = fugacity coefficient of FC-72 in gas phase at T, P

y_{FC} = equilibrium mole fraction of FC-72 in the gas phase at T, P

P = equilibrium system pressure

γ_{FC} = FC-72 activity coefficient in liquid phase

x_{FC} = equilibrium mole fraction of FC-72 in the liquid phase at T, P

ϕ_{FC}^{sat} = fugacity coefficient for pure FC-72 at T, P^{sat}

P_{FC}^{sat} = FC-72 saturation pressure at T, oftained from Antoine equation

V_{FC}^{L} = FC-72 liquid molar volume

R = ideal gas constant

T = system temperature

To simplify the calculation, we made the following assumptions:

- Liquid phase is pure FC-72 (ignoring air dissolving in FC-72), $x_{FC} = 1$
- Liquid phase behaves ideally, $\gamma_{FC} = 1$
- Gas phase also behaves ideally, $\hat{\phi}_{FC} = 1$ and $\phi_{FC}^{sat} = 1$, and that Dalton's law applies:

  $P = \sum_i p_i = p_{air} + p_{FC}$, where $p_{FC} = y_{FC}P$
- T is constant

After simplification, the equation becomes:

$$y_{FC}P = P_{FC}^{sat}\exp\left[\frac{V_{FC}^{L}(P-P_{FC}^{sat})}{RT}\right] \quad \text{(Eq. 2.14a)}$$

or, equivalently:

$$V_{FC}^{L}(P - P_{FC}^{sat}) = RT\ln\left(\frac{P-p_{air}}{P_{FC}^{sat}}\right) \quad \text{(Eq. 2.14b)}$$

Because the Poynting factor (exponential term in Eq. 2.14a) is close to unity, the equilibrium system pressure P is almost equal to the initial pressure plus FC-72 saturation pressure. This equation was analyzed numerically to calculate the predicted total pressure in the system (equal to P). If vapor pressure pumping is used in combination with the pumping lid approach, the final pressure P_1 should be used in place of p_{air}.

The values of P_{FC}^{sat} were obtained with the Antoine equation:

$$\ln(P_{FC}^{sat}\,[\text{atm}]) = 9.19734 - \frac{2488.59}{T\,[°C]+213.42} \quad \text{(Eq. 2.15)}^{34}$$

Model for temperature dependence of VLE pressure

Vapor pressure of the volatile liquid, and therefore the performance of this pumping approach, is affected by temperature. To make accurate predictions of the pressure generated by this vapor pressure pump, the ideal gas law was substituted for p_{air} (the initial pressure), which allowed us to take into account both the change in vapor pressure and gas expansion as the temperature is changed:

$$V_{FC}^{L}(P - P_{FC}^{sat}) = RT \ln\left(\frac{P - \frac{n_{air}RT}{V}}{P_{FC}^{sat}}\right) \quad \text{(Eq. 2.16)}$$

Eq. 2.16 was used to calculate the predicted value of P at different temperatures. The total volume available for gas in the device (V) was calculated in CAD software. The initial number of moles of air in the gas compartment (n_{air}) remains constant, and is dictated by the temperature at which the compartment was initially sealed from atmosphere (21.5 °C). The device was designed specifically to avoid any compression during the turning of the lid, to isolate the effects of VLE on pressure. For VLE pumping, we neglected the vapor pressure of the aqueous sample, because the vapor pressure of water is much lower than that of perfluorohexane (0.025 atm vs. 0.248 atm) at 21.5 °C.

Pressure and flow generation using the VLE method

The experimental behavior of pressure agreed with the theoretical predictions (Figure 2.7C). The equilibrium pressure obtained experimentally approached the pressure predicted by the simplified VLE model (Eq. 2.14), and the system was used to pump 20 µL of water through a microfluidic device in ~ 280 s (4.7 min). The VLE method could be used for pumping volumes in the milliliter range, for example 2 mL of water was pumped in more than 7 h, showing less than 30% reduction in the input pressure using a lid with a 30 mL gas compartment (Figure 2.7D). This reduction was caused by the fact that the volume previously occupied by sample became available to the gas phase to expand. As expected, larger lids took longer to equilibrate because more liquid needed to evaporate. However, the pressure remained stable when pumping was not in progress (Figure 2.7D),

so equilibration can be done prior to the pumping experiment. Alternatively, if the pressure does not need to be controlled precisely, the pumping can be started as soon as evaporation is initiated.

Tuning of VLE pressure by changing composition of the volatile liquid or temperature

To test our second hypothesis, we investigated generating pumping pressures by liquids with different vapor pressures. The equilibrium gauge pressure reached by the VLE system is related (but not necessarily equal) to the vapor pressure of the volatile liquid, according to Eq. 2.13. For a mixture of liquids, vapor pressure depends on the molar fraction of each component, amongst other factors. We measured the equilibrium pressures for different mixtures of FC-40 (vapor pressure 0.003 atm at 21.5 °C) and FC-72 (vapor pressure 0.248 atm at 21.5 °C). Equilibrium VLE pressure scaled linearly with the FC-72 molar fraction (R^2 = 0.9999) and approached ~ 0.003 atm for pure FC-40 (Figure 2.7E), as expected.

To test our third hypothesis, we investigated pressure generated by this vapor pressure pump at different temperatures using FC-72 as the volatile liquid. Because vapor pressure is a function of temperature (Eq. 2.15 and Eq. 2.16), the equilibrium pressure of FC-72/air system increased with temperature, yielding values consistent with those predicted by the VLE model (Figure 2.7F). Note that the change in pressure with temperature far exceeded the one predicted for heating of an ideal gas in a closed volume. This presents an opportunity to incorporate simple microfabricated heaters[35,36] to precisely control the pressures provided by this pump, and emphasizes the importance of temperature control for the operation of the vapor pressure pump. As mentioned earlier, VLE pumping can potentially be used in combination with the pumping lid gas compression or expansion. When generating positive pressure, the compression can be used to increase the range of pressures that can be achieved with the VLE approach. In the case of gas expansion, the use of VLE sets a lower limit to the pressure that can be obtained to the vapor pressure of the volatile liquid. The long-term stability of volatile liquids in the acrylic-based resins used for 3D-printing was not characterized, but preliminary experiments with the same liquids pre-packed in blister packs showed that it is possible to obtain similar pressures.

Conclusions

Here we described a way of generating positive and negative pressures with an equipment-free pumping lid and demonstrated its utility to induce flow in microfluidic devices. We used multi-material 3D printing to produce the parts, allowing fast prototyping without reducing their quality. This fabrication process is attractive because it allows rapid design iterations, and can also be scaled up to mass production using overmolding techniques. Here, pumping cups were attached to the device post-fabrication, but they can be included as part of the device during manufacturing. The first method described in this work relies on controlled compression or expansion of gas. While compression of gas has been demonstrated previously for pumping in microfluidic applications,[37] this work extends the previous approach. It demonstrates new capabilities, including (i) enabling the generation of both positive and negative pressures, (ii) the capability to adjust pressure in a programmed way while pumping is in progress; (iii) the use of multiple lids or a composite lid to control pressure at different inlets within the same device; and (iv) in addition to device loading applications, here we show more complex fluid manipulations, such as stable long-term laminar flow of multiple solutions and nanoliter droplet formation in two-phase flows. Furthermore, this work will enable others to use this approach more easily because (i) the method has been modeled and the model was quantitatively validated by experimentally measuring the pressures generated by the pumping lids; and (ii) the model was used to provide guidelines for the design of cups and pumping lids. We also demonstrated a complementary second method for generating pressure via evaporation of a volatile liquid in the pumping lid. The equilibrium pressure generated with this approach (before pumping starts) depends on the nature of the volatile liquid and on its temperature, but is not dependent on the geometry of the lid used for the experiment.

The approaches described in this work address many of the fluid-handling challenges that are faced when working with microfluidic devices[1-15] including those involving laminar flow,[22,38] droplets,[21,39-41] and cell culture experiments.[42-44] The simplicity of this pumping method overall and the use of the guiding structures make it robust to differences in pushing/pulling force; the user simply places a sample at the inlet and then pushes/pulls the pumping lid to generate the flow. Even when the user is applying excessive force (see video[30]), the method still operates as programmed;

this makes it suitable for even the most minimally trained users. The pumping lid approach is thus appropriate for a variety of applications in different settings. Experiments taking place in a research lab can benefit from this compact and equipment-free approach, reducing the need for external connectors and simplifying the workflow, especially when experiments are conducted in the controlled environments of a cell culture incubator[42-44] or an anaerobic chamber.[45] Additionally, contamination from the external environment and evaporation are minimized because the sample is contained in the pumping cup during the entire experiment. The pumping lid also allows flow rates to be tuned in real time while the experiment is in progress. The isolation and containment of samples is a characteristic that is highly desirable for cell culturing,[42] particularly when dealing with biohazardous samples and "organs-on-chip" technologies.[43,44] Such experiments are usually performed in controlled conditions (temperature, gas composition, etc.) and often require long pumping times.[15] With this approach, the entire pumping lid setup can be placed inside an incubator, without the need for external controllers. The use of VLE pumping is particularly suitable for temperature-controlled environments. Due to its portability and programmability, the pumping lid can also benefit applications in resource-limited settings, specifically for portable diagnostic devices.[6,7,24,26,28,46,47]

References

1. A. E. Herr, J. I. Molho, J. G. Santiago, M. G. Mungal, T. W. Kenny, and M. G. Garguilo, "Electroosmotic Capillary Flow with Nonuniform Zeta Potential," *Analytical Chemistry*, **2000**, 72, 1053-1057.
2. K. Choi, A. H. C. Ng, R. Fobel, and A. R. Wheeler, "Digital Microfluidics," *Annual Review of Analytical Chemistry*, **2012**, 5, 413-440.
3. A. A. Darhuber, J. P. Valentino, J. M. Davis, S. M. Troian, and S. Wagner, "Microfluidic actuation by modulation of surface stresses," *Applied Physics Letters*, **2003**, 82, 657-659.
4. S.-Y. Tang, K. Khoshmanesh, V. Sivan, P. Petersen, A. P. O'Mullane, D. Abbott, A. Mitchell, and K. Kalantar-zadeh, "Liquid metal enabled pump," *Proceedings of the National Academy of Sciences*, **2014**, DOI: 10.1073/pnas.1319878111.

5. C. Futterer, N. Minc, V. Bormuth, J. H. Codarbox, P. Laval, J. Rossier, and J. L. Viovy, "Injection and flow control system for microchannels," *Lab on a Chip*, **2004**, 4, 351-356.
6. A. W. Martinez, S. T. Phillips, G. M. Whitesides, and E. Carrilho, "Diagnostics for the Developing World: Microfluidic Paper-Based Analytical Devices," *Analytical Chemistry*, **2009**, 82, 3-10.
7. A. W. Martinez, S. T. Phillips, M. J. Butte, and G. M. Whitesides, "Patterned Paper as a Platform for Inexpensive, Low-Volume, Portable Bioassays," *Angewandte Chemie International Edition*, **2007**, 46, 1318-1320.
8. J. L. Osborn, B. Lutz, E. Fu, P. Kauffman, D. Y. Stevens, and P. Yager, "Microfluidics without pumps: reinventing the T-sensor and H-filter in paper networks," *Lab on a Chip*, **2010**, 10, 2659-2665.
9. R. Safavieh and D. Juncker, "Capillarics: pre-programmed, self-powered microfluidic circuits built from capillary elements," *Lab on a Chip*, **2013**, 13, 4180-4189.
10. M. Zimmermann, H. Schmid, P. Hunziker, and E. Delamarche, "Capillary pumps for autonomous capillary systems," *Lab on a Chip*, **2007**, 7, 119-125.
11. P. J. Resto, E. Berthier, D. J. Beebe, and J. C. Williams, "An inertia enhanced passive pumping mechanism for fluid flow in microfluidic devices," *Lab on a Chip*, **2012**, 12, 2221-2228.
12. G. M. Walker and D. J. Beebe, "A passive pumping method for microfluidic devices," *Lab on a Chip*, **2002**, 2, 131-134.
13. I. K. Dimov, L. Basabe-Desmonts, J. L. Garcia-Cordero, B. M. Ross, A. J. Ricco, and L. P. Lee, "Stand-alone self-powered integrated microfluidic blood analysis system (SIMBAS)," *Lab on a Chip*, **2011**, 11, 845-850.
14. D. Y. Liang, A. M. Tentori, I. K. Dimov, and L. P. Lee, "Systematic characterization of degas-driven flow for poly(dimethylsiloxane) microfluidic devices," *Biomicrofluidics*, **2011**, 5, 024108.
15. Y.-H. Hsu, M. L. Moya, C. C. W. Hughes, S. C. George, and A. P. Lee, "A microfluidic platform for generating large-scale nearly identical human microphysiological vascularized tissue arrays," *Lab on a Chip*, **2013**, 13, 2990-2998.
16. H. Bruus, *Theoretical microfluidics*, Oxford university press Oxford, **2008**.

17. D. C. Duffy, J. C. McDonald, O. J. A. Schueller, and G. M. Whitesides, "Rapid Prototyping of Microfluidic Systems in Poly(dimethylsiloxane)," *Analytical Chemistry*, **1998**, 70, 4974-4984.
18. S. L. Anna, N. Bontoux, and H. A. Stone, "Formation of dispersions using “flow focusing” in microchannels," *Applied Physics Letters*, **2003**, 82, 364-366.
19. H. Song, J. D. Tice, and R. F. Ismagilov, "A Microfluidic System for Controlling Reaction Networks in Time," *Angewandte Chemie International Edition*, **2003**, 42, 768-772.
20. T. Thorsen, R. W. Roberts, F. H. Arnold, and S. R. Quake, "Dynamic Pattern Formation in a Vesicle-Generating Microfluidic Device," *Physical Review Letters*, **2001**, 86, 4163-4166.
21. C. N. Baroud, F. Gallaire, and R. Dangla, "Dynamics of microfluidic droplets," *Lab on a Chip*, **2010**, 10, 2032-2045.
22. P. J. A. Kenis, R. F. Ismagilov, and G. M. Whitesides, "Microfabrication Inside Capillaries Using Multiphase Laminar Flow Patterning," *Science*, **1999**, 285, 83-85.
23. R. F. Ismagilov, A. D. Stroock, P. J. A. Kenis, G. Whitesides, and H. A. Stone, "Experimental and theoretical scaling laws for transverse diffusive broadening in two-phase laminar flows in microchannels," *Applied Physics Letters*, **2000**, 76, 2376-2378.
24. W. Du, L. Li, K. P. Nichols, and R. F. Ismagilov, "SlipChip," *Lab on a Chip*, **2009**, 8, 2286-2292.
25. L. Li, M. A. Karymov, K. P. Nichols, and R. F. Ismagilov, "Dead-End Filling of SlipChip Evaluated Theoretically and Experimentally as a Function of the Surface Chemistry and the Gap Size between the Plates for Lubricated and Dry SlipChips," *Langmuir*, **2010**, 26, 12465-12471.
26. F. Shen, E. K. Davydova, W. Du, J. E. Kreutz, O. Piepenburg, and R. F. Ismagilov, "Digital Isothermal Quantification of Nucleic Acids via Simultaneous Chemical Initiation of Recombinase Polymerase Amplification Reactions on SlipChip," *Analytical Chemistry*, **2011**, 83, 3533-3540.
27. F. Shen, W. Du, J. E. Kreutz, A. Fok, and R. F. Ismagilov, "Digital PCR on a SlipChip," *Lab on a Chip*, **2010**, 10, 2666-2672.

28. B. Sun, F. Shen, S. E. McCalla, J. E. Kreutz, M. A. Karymov, and R. F. Ismagilov, "Mechanistic Evaluation of the Pros and Cons of Digital RT-LAMP for HIV-1 Viral Load Quantification on a Microfluidic Device and Improved Efficiency via a Two-Step Digital Protocol," *Analytical Chemistry*, **2013**, 85, 1540-1546.
29. B. Sun, J. Rodriguez-Manzano, D. A. Selck, E. Khorosheva, M. A. Karymov, and R. F. Ismagilov, "Measuring Fate and Rate of Single-Molecule Competition of Amplification and Restriction Digestion, and Its Use for Rapid Genotyping Tested with Hepatitis C Viral RNA," *Angewandte Chemie International Edition*, **2014**, 53, 8088-8092.
30. D. Witters, B. Sun, S. Begolo, Rodriguez-Manzano, W. Robles, and R. Ismagilov, "SlipChip Movies," https://ismagilovlab.caltech.edu/multimedia/slip_chip_movies.shtml, **2014**.
31. D. Witters, B. Sun, S. Begolo, J. Rodriguez-Manzano, W. Robles, and R. F. Ismagilov, "Digital biology and chemistry," *Lab on a Chip*, **2014**, DOI: 10.1039/c4lc00248b.
32. F. Shen, B. Sun, J. E. Kreutz, E. K. Davydova, W. Du, P. L. Reddy, L. J. Joseph, and R. F. Ismagilov, "Multiplexed Quantification of Nucleic Acids with Large Dynamic Range Using Multivolume Digital RT-PCR on a Rotational SlipChip Tested with HIV and Hepatitis C Viral Load," *Journal of the American Chemical Society*, **2011**, 133, 17705-17712.
33. J. E. Kreutz, T. Munson, T. Huynh, F. Shen, W. Du, and R. F. Ismagilov, "Theoretical Design and Analysis of Multivolume Digital Assays with Wide Dynamic Range Validated Experimentally with Microfluidic Digital PCR," *Analytical Chemistry*, **2011**, 83, 8158-8168.
34. R. C. Reid, J. M. Prausnitz, and T. K. Sherwood, *The properties of gases and liquids*, McGraw-Hill, **1977**.
35. H. Takagi, R. Maeda, K. Ozaki, M. Parameswaran, and M. Mehta, "*Phase transformation type micro pump*," 1994 5th International Symposium on Micro Machine and Human Science Proceedings, IEEE, **1994**.
36. Y. Zhizhong and P. Andrea, "A microfluidic 'blinking bubble' pump," *Journal of Micromechanics and Microengineering*, **2005**, 15, 643.

37. S. Begolo, F. Shen, and R. F. Ismagilov, "A microfluidic device for dry sample preservation in remote settings," *Lab on a Chip*, **2013**, 13, 4331-4342.
38. R. S. Kane, S. Takayama, E. Ostuni, D. E. Ingber, and G. M. Whitesides, "Patterning proteins and cells using soft lithography," *Biomaterials*, **1999**, 20, 2363-2376.
39. H. Song, D. L. Chen, and R. F. Ismagilov, "Reactions in droplets in microflulidic channels," *Angewandte Chemie-International Edition*, **2006**, 45, 7336-7356.
40. S.-Y. Teh, R. Lin, L.-H. Hung, and A. P. Lee, "Droplet microfluidics," *Lab on a Chip*, **2008**, 8, 198-220.
41. A. B. Theberge, F. Courtois, Y. Schaerli, M. Fischlechner, C. Abell, F. Hollfelder, and W. T. S. Huck, "Microdroplets in Microfluidics: An Evolving Platform for Discoveries in Chemistry and Biology," *Angewandte Chemie International Edition*, **2010**, 49, 5846-5868.
42. E. K. Sackmann, A. L. Fulton, and D. J. Beebe, "The present and future role of microfluidics in biomedical research," *Nature*, **2014**, 507, 181-189.
43. D. Huh, G. A. Hamilton, and D. E. Ingber, "From 3D cell culture to organs-on-chips," *Trends in Cell Biology*, **2011**, 21, 745-754.
44. D. Huh, Y.-s. Torisawa, G. A. Hamilton, H. J. Kim, and D. E. Ingber, "Microengineered physiological biomimicry: Organs-on-Chips," *Lab on a Chip*, **2012**, 12, 2156-2164.
45. L. Ma, J. Kim, R. Hatzenpichler, M. A. Karymov, N. Hubert, I. M. Hanan, E. B. Chang, and R. F. Ismagilov, "Gene-targeted microfluidic cultivation validated by isolation of a gut bacterium listed in Human Microbiome Project's Most Wanted taxa," *Proceedings of the National Academy of Sciences*, **2014**, 111, 9768-9773.
46. P. Yager, T. Edwards, E. Fu, K. Helton, K. Nelson, M. R. Tam, and B. H. Weigl, "Microfluidic diagnostic technologies for global public health," *Nature*, **2006**, 442, 412-418.
47. P. Yager, G. J. Domingo, and J. Gerdes, "Point-of-Care Diagnostics for Global Health," *Annual Review of Biomedical Engineering*, **2008**, 10, 107-144.

Supplementary Material

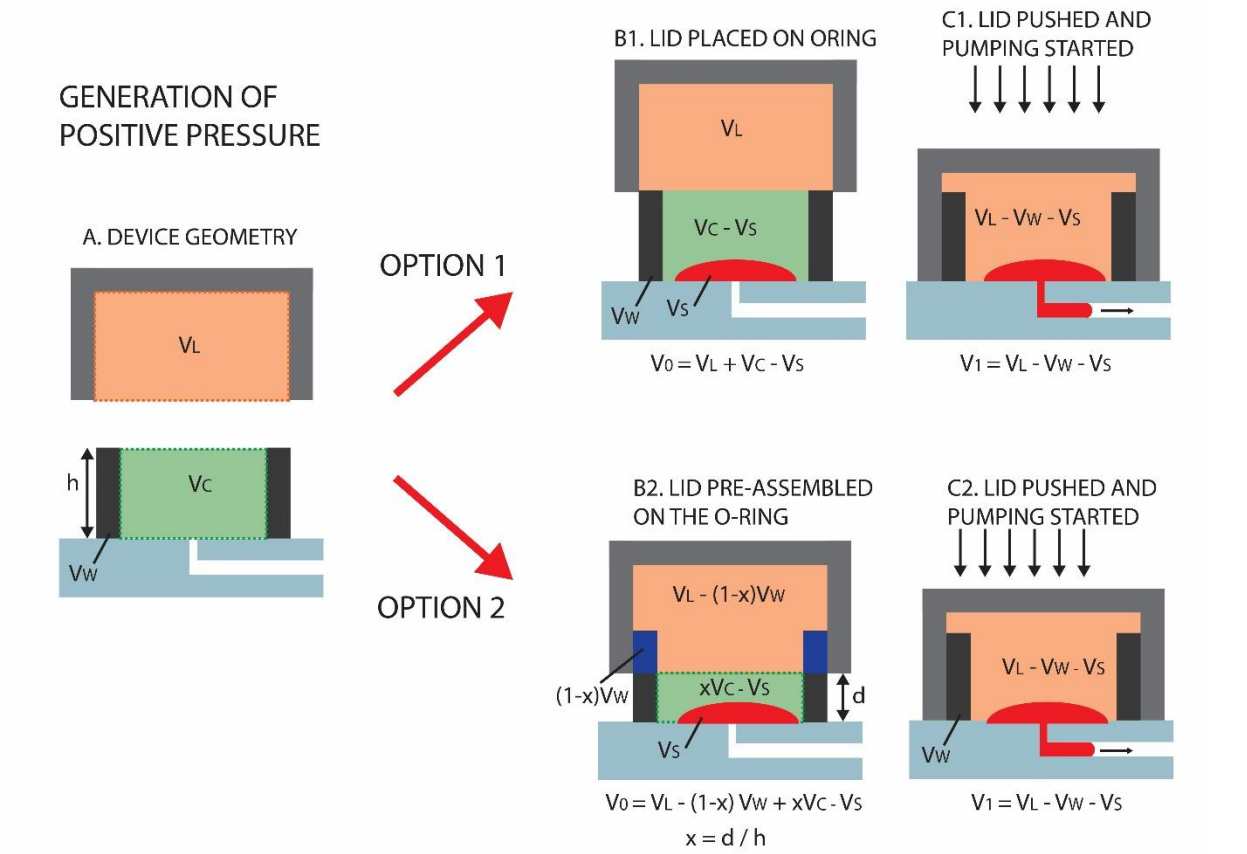

Figure S2.1 Schematic representation of the parameters used for the calculation of the positive pressure.

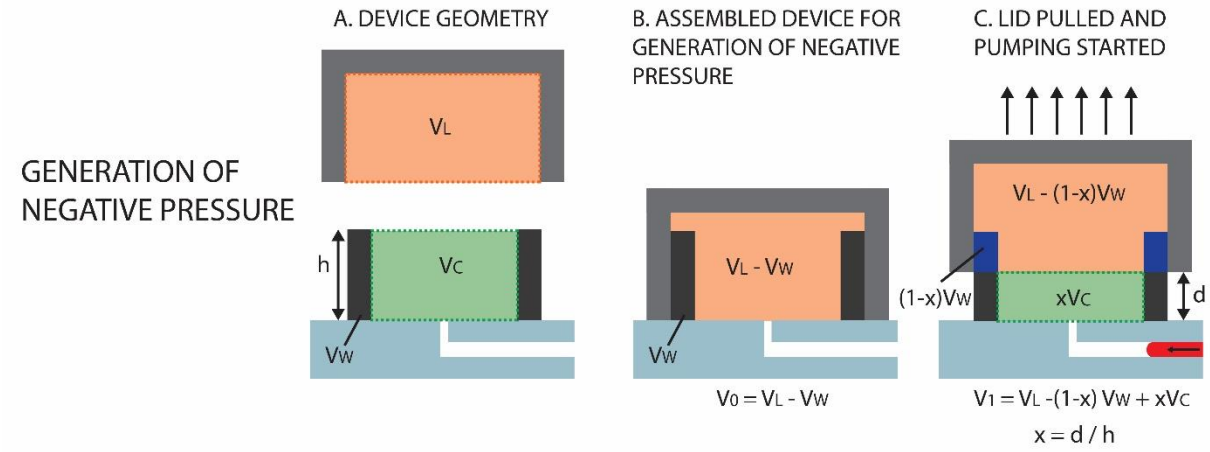

Figure S2.2 Schematic representation of the parameters used for the calculation of the negative pressure.

Experimental section

3D printing

Lids and cups described in this paper were produced by multi-material 3D printing. The geometry of each part was designed using CAD software and exported to STL-files. Parts were printed with an Objet 260 printer (Stratasys, Eden Prairie, MN, USA), which can produce composite parts that combine two materials with different mechanical properties, and mixtures of these two materials. All rigid parts described in this paper were made of VeroClear material (RGD810); flexible parts were made of TangoPlus material (FLX930). Both materials were purchased from Stratasys.

Lid and cup design

All pumping lids described in this paper were designed to have an empty cavity. In some cases, the lids were printed in separate parts and then assembled using 5-min epoxy glue (ITW Devcon, Danvers, MA, USA). Surfaces used for bonding were sand-papered to remove any trace of the 3D printing support material. Cups were designed with a flat base (0.5 mm to 2 mm thick) for bonding to the microfluidic devices. Other alignment-aiding features (such as locks, guiding structures, etc.) were integrated with this flat base as well. The pumping mechanism relies on air being confined in the lid cavity. To ensure effective sealing, the cup must be slightly (100 μm to 200 μm) bigger than the hole in the pumping lid. A deformable soft layer was included at the junction to provide a hermetic seal. This layer was between 1 mm and 1.5 mm thick and could be made pre-attached to either the pumping lid or the cup. Lubricants such as high-vacuum grease (Dow Corning) and Krytox (DuPont) were used to reduce friction between the parts during the experiments.

Pressure measurement experiments

For the experiments described in Figure 2.1, four different pumping lids and five different cups were used. All 20 combinations were tested for generation of positive and negative pressure (Figure 2.1C). In this case, the cups were printed directly on a rigid support and not connected to a microfluidic device. To ensure that the measured pressure was due to controlled expansion or compression of air, this rigid support had a venting hole that was closed with adhesive tape after the pumping lid was placed in its starting position. The experimental values of pressures measured with this approach were compared to the theoretical values calculated using Eq. 2.2 and Eq. 2.6. For simplicity, no

sample was placed in the cup during the reported experiments. The experimental conditions and predicted values of the generated pressure are reported in Table TS2.1.

Table TS2.1 Pressure measurements reported in Figure 2.1C. The geometrical parameters (V_C, V_R, V_E, x) were used to calculate the predicted gauge pressure value for both positive and negative pressures, according to Eq. 2.2 and Eq. 2.6 in the main text. These were compared to experimental values (mean ± S.D.) (N=3).

V_C (µL)	V_R (µL)	V_E (µL)	x	Positive Pressure			Negative pressure		
				Predicted Gauge Pressure (atm)	Experimental Gauge Pressure (atm)	Standard Deviation (atm)	Predicted Gauge Pressure (atm)	Experimental Gauge Pressure (atm)	Standard Deviation (atm)
14730	3527	0	0.25	0.079	0.075	0.002	-0.073	-0.068	0.002
19746	3527	0	0.25	0.054	0.053	0.001	-0.052	-0.050	0.001
34795	3527	0	0.25	0.028	0.028	0.001	-0.027	-0.027	0.000
44828	3527	0	0.25	0.021	0.021	0.001	-0.021	-0.020	0.000
14730	3527	0	0.5	0.157	0.152	0.002	-0.136	-0.126	0.003
19746	3527	0	0.5	0.109	0.105	0.001	-0.098	-0.089	0.000
34795	3527	0	0.5	0.056	0.055	0.001	-0.053	-0.050	0.001
44828	3527	0	0.5	0.043	0.043	0.002	-0.041	-0.039	0.000
14730	3527	0	0.75	0.236	0.232	0.002	-0.191	-0.175	0.000
19746	3527	0	0.75	0.163	0.161	0.001	-0.140	-0.132	0.001
34795	3527	0	0.75	0.085	0.084	0.000	-0.078	-0.072	0.000
44828	3527	0	0.75	0.064	0.064	0.001	-0.060	-0.056	0.000
14730	3056	471	0.5	0.151	0.148	0.001	-0.131	-0.121	0.001
19746	3056	471	0.5	0.106	0.104	0.001	-0.096	-0.090	0.001
34795	3056	471	0.5	0.056	0.056	0.001	-0.053	-0.049	0.000
44828	3056	471	0.5	0.042	0.043	0.000	-0.041	-0.039	0.000
14730	813	2714	0.5	0.126	0.124	0.001	-0.112	-0.109	0.003
19746	813	2714	0.5	0.093	0.092	0.002	-0.085	-0.082	0.002
34795	813	2714	0.5	0.052	0.052	0.000	-0.049	-0.048	0.001
44828	813	2714	0.5	0.040	0.039	0.000	-0.038	-0.037	0.000

Microfluidic device fabrication (PDMS)

Devices used for flow experiments were fabricated using rapid prototyping in PDMS[1] from SU-8 photoresist molds. The devices were sealed by using a Plasma Prep II (SPI Supplies, West Chester, PA), and then baked overnight at 110 °C. Cups were connected to the PDMS devices by using adhesive transfer tapes (3M 468MP; Uline, Pleasant Prairie, WI, USA), except in experiments involving fluorinated oils, where we used a silicone based adhesive (RTV 108 Translucent adhesive, Momentive performance materials, Columbus, OH, USA).

Flow rate experiments

The device consisted of glass-bonded PDMS layer, cup, PTFE tubing, and the pumping lid (Figure S2.3). A 30.8 cm long, 58 µm high, 110 µm wide serpentine was molded into the PDMS layer. The nominal hydraulic resistance for this device with pure water at 21.5 °C is 2.58 * 10^{14} Pa s /m^3 (as calculated using Eq. 2.10).[2] Prior to bonding to the glass slide, the PDMS layer was punctured (0.5 mm diameter) at the beginning and end of the serpentine. The 3D printed cup was attached to the other side of the PDMS layer with 3M 468MP transfer adhesive. A PTFE tubing (ID 356 µm) was connected to the device outlet, as shown in Figure S2.3. The serpentine in the PDMS-glass device was pre-loaded with sample up to the point A. The cup was loaded with 50 µL of the same sample. The pumping lid was then pressed onto the cup, resulting in compression of air in the pumping lid cavity. The time it took the air-liquid interface to travel from point A to point B was recorded (point B was 3.2 cm downstream from point A). Given the constant inner diameter of the PTFE tubing, the total volume pumped in that time was calculated to be 3.178 µL. This value was used to calculate the flow rate. The same device was used for all the flow rate experiments, with a DI water flush between different sample types. The density of the Tween-20 and Triton X100 solutions was assumed to equal that of pure water and viscosity was measured for all of the liquids using a M2-6 viscometer (Cannon Instrument Co., State College, PA, USA).

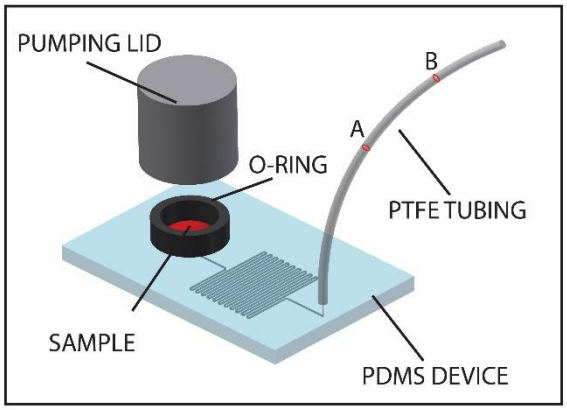

Figure S2.3 Schematic of the experimental setup used for flow rate measurement.

Table TS2.2 Properties of the liquids used in the flow rate experiments.

Aqueous solution	Surface Energy (mN/m)	Viscosity (mPa*s)	Density (g/mL)
Water (DI)	72.4 [3]	0.99	1.00
Tween 20 3.16e-6M	***53*** [4]	0.99	1.00
Tween 20 3.16e-5M	***35*** [4]	1.00	1.00
Triton x100 1e-5M	***57.5*** [5]	1.00	1.00
Triton x100 1.6mM	***30*** [5]	1.00	1.00
Glycerol 30 wt%	71 [6]	***2.10***	1.07
Glycerol50 wt%	69 [6]	***3.98***	1.11
CsCl 3.66 M	>75 [7]	0.93	***1.47***
CsCl 7.09 M	>75 [7]	1.24	***1.90***

Table TS2.3 Mean (± s.d.) pumping times and mean experimental flow rate, Q, (± s.d.) of nine sample types (N=3).

Pressure (atm)	Water		Tween-20 3.16e-6 M		Tween-20 3.16e-5 M	
	Mean pumping time (± s.d.) (s)	*Q* (± s.d.) (μL/min)	Mean pumping time (± s.d.) (s)	*Q* (± s.d.) (μL/min)	Mean pumping time (± s.d.) (s)	*Q* (± s.d.) (μL/min)
0.199	37.7 (1.2)	5.06 (0.17)	37.0 (1.4)	5.15 (0.20)	37.3 (0.9)	5.11 (0.13)
0.174	43.3 (0.9)	4.40 (0.10)	43.0 (0.8)	4.43 (0.08)	43.0 (1.4)	4.43 (0.15)
0.145	51.3 (0.5)	3.71 (0.03)	50.7 (0.5)	3.76 (0.04)	51.3 (1.2)	3.71 (0.09)
0.124	62.0 (0.8)	3.08 (0.04)	62.0 (0.8)	3.08 (0.04)	62.0 (0.8)	3.08 (0.04)
0.094	83.3 (0.9)	2.29 (0.03)	81.3 (0.5)	2.34 (0.01)	80.0 (0.8)	2.38 (0.02)
0.069	113.3 (2.0)	1.68 (0.03)	112.7 (0.5)	1.69 (0.01)	109.7 (1.2)	1.74 (0.02)
0.049	173.7 (4.5)	1.10 (0.03)	168.3 (2.6)	1.13 (0.02)	163.0 (0.8)	1.17 (0.01)

Pressure (atm)	Triton x100 1e-5 M		Triton x100 1.6 mM		Glycerol 30 wt%	
	Average Pumping time (± s.d.) (s)	*Q* (± s.d.) (μL/min)	Average Pumping time (± s.d.) (s)	*Q* (± s.d.) (μL/min)	Average Pumping time (± s.d.) (s)	*Q* (± s.d.) (μL/min)
0.199	38.0 (0.8)	5.02 (0.11)	38.0 (0.8)	5.02 (0.11)	82.0 (0.8)	2.33 (0.02)
0.174	44.7 (0.5)	4.27 (0.05)	43.3 (0.5)	4.40 (0.05)	95.7 (0.5)	1.99 (0.01)
0.145	52.0 (0.8)	3.67 (0.06)	52.0 (0.8)	3.67 (0.06)	111.0 (0.8)	1.72 (0.01)
0.124	62.0 (1.6)	3.08 (0.08)	61.7 (1.2)	3.09 (0.06)	136.3 (3.8)	1.40 (0.04)
0.094	81.3 (1.2)	2.34 (0.04)	78.3 (1.2)	2.43 (0.04)	180.7 (8.8)	1.06 (0.05)
0.069	115.7 (2.5)	1.65 (0.04)	107.3 (0.5)	1.78 (0.01)	248.0 (5.0)	0.77 (0.02)
0.049	169.3 (1.2)	1.13 (0.01)	155.7 (4.1)	1.22 (0.03)	379.0 (8.5)	0.50 (0.01)

Pressure (atm)	Glycerol 50 wt%		CsCl 3.66 M		CsCl 7.09 M	
	Average Pumping time (± s.d.) (s)	*Q* (± s.d.) (μL/min)	Average Pumping time (± s.d.) (s)	*Q* (± s.d.) (μL/min)	Average Pumping time (± s.d.) (s)	*Q* (± s.d.) (μL/min)
0.199	160.0 (2.1)	1.19 (0.02)	49.0 (1.4)	3.89 (0.11)	37.0 (1.4)	5.15 (0.20)
0.174	181.7 (2.0)	1.05 (0.01)	56.3 (1.7)	3.38 (0.10)	42.0 (1.4)	4.54 (0.15)
0.145	217.7 (3.1)	0.88 (0.01)	68.3 (1.9)	2.79 (0.08)	51.0 (1.4)	3.74 (0.10)
0.124	269.7 (6.3)	0.71 (0.02)	82.3 (0.5)	2.32 (0.01)	61.7 (0.9)	3.09 (0.05)
0.094	349.0 (5.7)	0.55 (0.01)	105.3 (0.5)	1.81 (0.01)	83.3 (1.9)	2.29 (0.05)
0.069	462.3 (5.2)	0.41 (0.01)	146.0 (2.2)	1.31 (0.02)	110.7 (1.9)	1.72 (0.03)
0.049	727.7 (21.5)	0.26 (0.01)	231.0 (4.2)	0.83 (0.02)	164.0 (2.1)	1.16 (0.02)

Generating droplets

Droplet generation experiments were performed using two geometries: flow focusing[8] and T-junction.[9] These devices were produced in PDMS by replica molding, bonded onto a flat layer of PDMS, and incubated at 110 °C for at least 24 h to recover the hydrophobic properties of PDMS. Prior to each experiment, the device was loaded with the inert, water-immiscible carrier fluid—a solution of perfluorodecaline (Acros Organics) and perfluorooctanol (Alfa Aesar), 9:1 volume ratio, as described previously.[10]

Flow focusing

The geometry for flow focusing had two inlets (one for water and the other for the carrier fluid). Channels in the junction were 100 μm wide and 35 μm tall. The device included a serpentine channel (100 μm wide and 10.5 cm long) between each inlet and the junction, to increase fluidic resistance. A separate cup was glued at each inlet. To generate droplets, a 100 μL sample of 0.5M FeSCN was placed in the cup at the water inlet and 100 μL of carrier fluid were placed in the other cup (Figure 2.4A). The pumping lids were then placed on the cups and pushed into final positions to generate flow. Pressures generated were 0.2 atm for the carrier fluid and 0.07 atm for the aqueous solution.

T-junction

The channel system for the T-junction included four inlets: three for water (in place of the single water inlet in Figure 4A) and one for the carrier fluid. The three water channels were composed of serpentine, measured 50 μm tall and 10.5 cm long and merged just before the T-junction (Figure 2.4B, Right). The channel used for the carrier fluid is 100 μm wide and 50 μm tall, and included a 10.5 cm long serpentine between the junction and the inlet. To generate droplets, 100 μL of one of the three solutions (0.5M FeSCM, pure water, and green food dye) were placed at the channel inlet in each of the three sample cups, and 100 μL of the carrier fluid were placed in the fourth cup. The three sample inlets were controlled with the composite lid used in laminar flow experiments (composite lid 1, Figure 2.5C), and the pressure applied to each of these inlets was 0.16 atm. The carrier fluid was controlled by a separate lid, producing a pressure of 0.2 atm.

Laminar flow experiments

PDMS devices that were used for the laminar flow experiments had a constant channel height of 40 µm (Figure 2.4C). Three inlets were included in each device, and each inlet was controlled by a separate cup (12 mm external diameter). We monitored the laminar flow patterns at the junction where the three channels (each 500 µm wide) merged into a single 1,500 µm wide channel. Between each of the three inlets and this junction, the device design included a serpentine channel (100 µm wide and 10.5 cm long) to increase hydraulic resistance. Experiments were performed by placing up to 300 µL of sample in each of the three cups (0.5M FeSCM, pure water, and green food dye solution). Pressure could be produced by placing a different lid on each cup or by using a composite lid containing three apertures that align to each cup. For the experiments shown in Figure 4C, three separate lids were used, each producing a pressure of 0.16 atm.

Five different composite lids were used to produce the five flow profiles shown in Figure 5C. Based on the pressure applied to each inlet, the predicted flow profile can be calculated for each of the three streams (Figure 2.5C; Table TS2.4). The device geometry was such as the fluidic resistance of the channel between each of the three inlets and the junction (R) was significantly bigger than the fluidic resistance between the junction and the outlet. Under this condition, the flow rate in each branch can be calculated as $Q_i \approx \frac{P_i}{R}$.

Table TS2.4 Calculated flow rates for the five lids used in the laminar flow experiments. The pressure generated at each inlet was used to calculate the flow rate for each channel. The hydraulic resistances R and r were $3.419 * 10^{14}$ Pa s /m^3 and $8.745 * 10^{12}$ Pa s /m^3, (values calculated according to the hydraulic resistance formula[2]). For each lid, the flow rate ratio (Q_1/Q_{tot}) was calculated to plot the predicted flow profile in Figure 2.5C.

Lid Number	P_1 (atm)	P_2 (atm)	P_3 (atm)	Q_1 (µL/min)	Q_2 (µL/min)	Q_3 (µL/min)	Flow Ratio 1	Flow Ratio2	Flow Ratio 3
1	0.160	0.160	0.160	2.61	2.61	2.61	0.33	0.33	0.33
2	0.068	0.347	0.068	1.00	5.88	1.00	0.13	0.75	0.13
3	0.347	0.036	0.347	5.77	0.32	5.77	0.49	0.03	0.49
4	0.347	0.068	0.068	5.88	1.00	1.00	0.75	0.13	0.13
5	0.068	0.068	0.347	1.00	1.00	5.88	0.13	0.13	0.75

SlipChip devices fabrication and experimental procedure

The SlipChip device used by the 6-year-old volunteer was produced by injection molding using polycarbonate and was provided by SlipChip Corp. The glass device used for vacuum loading was produced by wet-etching of soda lime glass, using the protocol described in previous work.[11] The surfaces of these devices were treated with silane vapor to render them hydrophobic, using a protocol described in previous work.[12] The particular glass device with multivolume wells that we used is described in previous work.[13] Wells were etched at two different depths (40 µm and 100 µm) to obtain four different volumes: 1 nL, 5 nL, 25 nL, and 125 nL. The device also included a circular ring (100 µm deep and 4 mm wide), surrounding all the wells. Two through-holes were drilled in the top layer: the cup used for generating the vacuum was glued with 5-min epoxy (ITW Devcon, Danvers, MA, USA) on the outlet hole, and a pierced PDMS piece (silicone rubber with adhesive back, 1.5 mm thick, McMaster-Carr) was placed on the inlet hole to contain the sample during loading. Prior to device assembly, the pumping lid was placed on the cup, and the etched rings surrounding the wells were filled with high vacuum grease (Dow Corning) to ensure complete sealing of the active region of the device. Device assembly was performed in silicone oil (5 cSt, Sigma Aldrich). A 50 µL drop of 0.5 M FeSCN aqueous solution was then placed at the device inlet, and the pumping lid was pulled to produce ~ 0.1 atm of negative gauge pressure and initiate the device loading. After loading by dead end filling was complete, a slipping step was performed to separate the sample into discrete droplets.

Vapor-liquid equilibrium experiments

To harness vapor pressure for pumping, we designed a different set of lids and cups (vapor pressure pump) shown in Figure 2.7A. The geometry and materials used are similar to the pumping lids described earlier, but in this case the cup is partitioned into separate compartments for liquid and gas. The gas compartment has an opening on the bottom that allows pumping through a PDMS device once the cup is bonded to it with 3M 468MP double-sided tape. The lid was designed with a pressure-sensor nozzle. It also has a top opening for loading and pressure equilibration with the atmosphere. Once the lid is put onto the cup, it can be turned to control the connection between different compartments and the atmosphere. The system was designed so that lid rotation did not induce compression in either compartment. We used the 5 psi differential pressure sensor (PXCPC-005DV, Omega Engineering) for real-time pressure monitoring.

The liquid compartment was filled completely with perfluorohexane (FC-72, Sigma Aldrich) (224 µL), sealed by the lid, and exposed to the gas compartment when the lid was twisted. To illustrate the broad range of sample volumes compatible with this method, we show results for 20 µL and 2 mL. Samples were loaded into the gas compartment of the vapor pressure pump, at the inlet of the PDMS channel. In the case of the 2 mL experiment, a larger gas compartment was used, because the volume has to be large enough to accommodate the sample, and to reduce the pressure drop caused by pumping. The microfluidic channel was opened after the pressure equilibrated, although pumping can begin before equilibrium is reached. The equilibrium pressure for FC-72 at room temperature (21.5 °C), calculated using Eq. 2.14b, is 1.252 atm (corresponding to 0.252 atm gauge pressure).

To show that this approach can be used with a variety of pressures, and to illustrate one convenient way of tuning the equilibrium pressure, a modified device was utilized. In this case, the gas compartment was printed without an outlet on the bottom. Mixtures of FC-72/FC-40 liquids of different molar ratios were used for these experiments, which were carried out by loading the compartmentalized cup, sealing with the lid without compression, and twisting the lid to connect the liquid and gas compartments, N=3 (Figure 2.7E, Table TS2.5). Pressure equilibration was monitored with the 5 psi differential pressure sensor (PXCPC-005DV, Omega Engineering).

Table TS2.5 Experimental values for equilibrium pressures obtained with mixtures of FC-72 and FC-40 (N=3).

Molar Fraction of FC-72	Average Equilibrium Gauge Pressure (atm)	Standard Deviation (atm)
1.0	0.240	0.003
0.8	0.190	0.002
0.6	0.143	0.0005
0.4	0.095	0.001
0.2	0.047	0.002

The dependence of equilibrium pressure on temperature was tested using the same device. After loading and sealing the device, we removed the inner partition between the gas and liquid compartments by twisting the lid. All loading and sealing steps were done at 21.5 °C. Then the device was placed in an incubator with an adjustable temperature, which was monitored in real time using a thermocouple (5TC-TT-K-36-36, Omega Engineering). Both pressure and temperature were recorded through the same LabVIEW script at 2 Hz. Once VLE was reached at one temperature, we re-adjusted the incubator to a new temperature, and allowed the VLE to re-establish itself (Table TS2.6). Data were compared to the predicted pressure calculated using Eq. 2.16 (Figure 2.7F, Table TS2.7).

Table TS2.6 Experimental gauge pressures at different temperatures.

Data set 1		Data set 2	
T **(°C)**	**Gauge Pressure (atm)**	***T*** **(°C)**	**Gauge Pressure (atm)**
21.06	0.2372	20.72	0.2360
23.30	0.2750	23.22	0.2698
25.38	0.3089	24.87	0.2980
27.36	0.3425	26.65	0.3292
		28.25	0.3575
		30.06	0.3893

Table TS2.7 Predicted gauge pressures at different temperatures for FC-72, using Eq. 2.16.

T **(°C)**	***P*** **gauge (atm)**	***T*** **(°C)**	***P*** **gauge (atm)**	***T*** **(°C)**	***P*** **gauge (atm)**
19	0.216	24	0.290	29	0.375
20	0.230	25	0.306	30	0.393
21	0.244	26	0.322	31	0.412
22	0.259	27	0.339	32	0.432
23	0.274	28	0.357		

Supplementary References

1. D. C. Duffy, J. C. McDonald, O. J. A. Schueller, and G. M. Whitesides, "Rapid Prototyping of Microfluidic Systems in Poly(dimethylsiloxane)," *Analytical Chemistry*, **1998**, 70, 4974-4984.
2. H. Bruus, *Theoretical microfluidics*, Oxford university press Oxford, **2008**.
3. L. Li, M. A. Karymov, K. P. Nichols, and R. F. Ismagilov, "Dead-End Filling of SlipChip Evaluated Theoretically and Experimentally as a Function of the Surface Chemistry and the Gap Size between the Plates for Lubricated and Dry SlipChips," *Langmuir*, **2010**, 26, 12465-12471.
4. M. Niño and J. M. R. Patino, "Surface tension of bovine serum albumin and tween 20 at the air-aqueous interface," *Journal of the American Oil Chemists' Society*, **1998**, 75, 1241-1248.
5. N. Wu, J. Dai, and F. J. Micale, "Dynamic Surface Tension Measurement with a Dynamic Wilhelmy Plate Technique," *Journal of Colloid and Interface Science*, **1999**, 215, 258-269.
6. R. W. Gallant, *Hydrocarbon Processing*, **1967**, 46, 201-215.
7. N. Matubayasi, H. Matsuo, K. Yamamoto, S.-i. Yamaguchi, and A. Matuzawa, "Thermodynamic Quantities of Surface Formation of Aqueous Electrolyte Solutions: I. Aqueous Solutions of NaCl, MgCl2, and LaCl3," *Journal of Colloid and Interface Science*, **1999**, 209, 398-402.

8. S. L. Anna, N. Bontoux, and H. A. Stone, "Formation of dispersions using “flow focusing” in microchannels," *Applied Physics Letters*, **2003**, 82, 364-366.
9. T. Thorsen, R. W. Roberts, F. H. Arnold, and S. R. Quake, "Dynamic Pattern Formation in a Vesicle-Generating Microfluidic Device," *Physical Review Letters*, **2001**, 86, 4163-4166.
10. H. Song and R. F. Ismagilov, "Millisecond kinetics on a microfluidic chip using nanoliters of reagents," *Journal of the American Chemical Society*, **2003**, 125, 14613-14619.
11. W. Du, L. Li, K. P. Nichols, and R. F. Ismagilov, "SlipChip," *Lab on a Chip*, **2009**, 8, 2286-2292.
12. F. Shen, W. Du, J. E. Kreutz, A. Fok, and R. F. Ismagilov, "Digital PCR on a SlipChip," *Lab on a Chip*, **2010**, 10, 2666-2672.
13. F. Shen, B. Sun, J. E. Kreutz, E. K. Davydova, W. Du, P. L. Reddy, L. J. Joseph, and R. F. Ismagilov, "Multiplexed quantification of nucleic acids with large dynamic range using multivolume digital RT-PCR on a rotational SlipChip tested with HIV and Hepatitis C viral load," *Journal of the American Chemical Society*, **2011**, 133, 17705-17712.

CHAPTER 3

Reading out single-molecule digital RNA and DNA isothermal amplification in nanoliter volumes with unmodified camera phones

Abstract

Digital single-molecule technologies are expanding diagnostic capabilities, enabling the ultrasensitive quantification of targets, such as viral load in HIV and hepatitis C infections, by directly counting single molecules. Replacing fluorescent readout with a robust visual readout that can be captured by any unmodified cell phone camera will facilitate the global distribution of diagnostic tests, including in limited-resource settings where the need is greatest. This paper describes a methodology for developing a visual readout system for digital single-molecule amplification of RNA and DNA by (i) selecting colorimetric amplification-indicator dyes that are compatible with the spectral sensitivity of standard mobile phones, and (ii) identifying an optimal ratiometric image-process for a selected dye to achieve a readout that is robust to lighting conditions and camera hardware and provides unambiguous quantitative results, even for colorblind users. We also include an analysis of the limitations of this methodology, and provide a microfluidic approach that can be applied to expand dynamic range and improve reaction performance, allowing ultrasensitive, quantitative measurements at volumes as low as 5 nL. We validate this methodology using SlipChip-based digital single-molecule isothermal amplification with λDNA as a model and hepatitis C viral RNA as a clinically relevant target. The innovative combination of isothermal amplification chemistry in the presence of a judiciously chosen indicator dye and ratiometric image processing with SlipChip technology allowed the sequence-specific visual readout of single nucleic acid molecules in nanoliter volumes with an unmodified cell phone camera. When paired with devices that integrate sample preparation and nucleic acid amplification, this hardware-agnostic approach will increase the affordability and the distribution of quantitative diagnostic and environmental tests.

Introduction

This paper shows that single nucleic acid molecules confined in nanoliter volumes in microfluidic devices can be detected and counted by an unmodified cell phone camera, in combination with isothermal amplification chemistry, a judiciously chosen indicator dye and ratiometric image processing. We describe a novel methodology that can be used to develop a visual readout for digital single-molecule amplification of sequence-specific RNA and DNA that can be used with any camera phone, without modifications or attachments. Single-molecule visual readout has never been achieved before with an unmodified cell phone camera. Diagnostic tests that incorporate such a visual readout will greatly expand the applicability of emerging digital single-molecule technologies, including in limited resource settings (LRS). Ultrasensitive and quantitative detection of nucleic acid molecules is of particular interest for infectious disease diagnosis in LRS, such as the quantification of viral load for human immunodeficiency virus (HIV) and hepatitis C virus (HCV),[1-3] as many of these infections occur far from centralized laboratories where diagnostic tests are routine. Increasing diagnoses in these locations will lead to faster and more appropriate treatment and have a major impact on disease burden.[4,5] Most point of care (POC) tests are not amenable to LRS because they do not meet the World Health Organization's ASSURED criteria of being affordable, sensitive, specific, user-friendly, rapid, robust, equipment-free, and deliverable.[5] The tests that do meet the requirements for LRS (*e.g.*, immunochromatography to detect antigens or antibodies in a dipstick or lateral-flow format; or the visualization of antigen–antibody lattice formation) have poor reported sensitivities and thus are unable to detect and quantify analytes at low concentrations.[4,6] Nucleic acid amplification tests (NAATs), such as PCR, have the desired high sensitivity and target specificity, providing accurate quantification, but these technologies are costly, time-consuming, and require skilled technicians and laboratory settings.[7]

Of the NAATs, isothermal amplification methods (*e.g.*, loop-mediated isothermal amplification, LAMP) are among the most attractive for LRS because they do not require thermocycling or capital equipment and can be run in water baths, using simple heaters or with exothermic chemical heating that does not require electricity.[8-11] Still, acquiring quantitative and ultrasensitive measurements outside of the lab remains challenging because the methods are not robust to variability in reaction

conditions and readouts rely on precise measures of fluorescence intensity. Running isothermal amplification chemistries in a digital, single-molecule format maintains the high sensitivity and quantification capabilities typically achieved only in lab settings.[12-15] In digital single-molecule isothermal amplification, single, stochastically confined DNA or RNA molecules are randomly distributed among discrete nanoliter or picoliter volumes and amplified under controlled conditions.[16-18] This creates relatively high local concentrations of target DNA or RNA, making digital amplification more efficient and robust compared to bulk reactions with the same number of starting target molecules. Nucleic acid amplification of even a single target molecule produces a clear fluorescent signal and the results of digital amplification can be read by a modified cell phone (*e.g.*, a phone camera with an optical filter) under dim lighting.[14]

Microfluidic technology has been an instrumental tool in developing single nucleic acid molecule capabilities,[19-27] and the integration of sample-preparation modules into portable microfluidic devices will further enable their use by untrained users in any setting.[28-30] To bring these emerging technological capabilities to LRS, however, such devices capable of ultrasensitive, quantitative measurements should provide a rapid, visual readout that can be captured easily, *e.g.*, by any mobile phone without modifications or attachments. Cell phone cameras provide a convenient, nearly universal tool to pair with emerging diagnostic technologies to transform global healthcare as ~7 billion mobile cellular subscribers exist worldwide and 70% of users live in developing countries.[31] Mobile devices are emerging as a powerful platform to create cost-effective alternatives for molecular diagnostics in LRS[32-42] and colorimetric diagnostics based on unmodified cell phones have been used before,[38,43-46] but not in a digital format, where the short path lengths and nanoliter volumes have constrained visual-based methods. Here, we describe an approach that enables visual readout of single nucleic acid molecule amplification by (i) selecting an appropriate colorimetric indicator dye based on spectral properties that align well with the RGB sensitivities of common cell phone camera sensors and (ii) identifying the optimal ratiometric image-processing for the selected dye to achieve a readout that is robust to lighting conditions and camera hardware. With this approach, after sequence-specific single-molecule isothermal amplification, a visual readout is captured by an unmodified camera phone and the resulting image is analyzed using a ratiometric approach, wherein the measured intensities of two of the three RGB color channels are divided to provide a binary result

(a positive or negative reaction) for each well. The automation of this ratiometric analysis provides a clear, reliable digital readout without requiring the user to differentiate color change by eye or manipulate lighting (Figure 3.1a). We further show how limitations related to reaction inhibition by the readout dye can be solved with SlipChip microfluidics technology to decouple the amplification and readout steps. We validated our visual readout method with SlipChip-based digital single-molecule isothermal amplification reactions using phage lambda DNA (λDNA) as a model and HCV RNA as a clinically relevant target, in reaction volumes as low as 5 nL, using a variety of common cell phones and a range of illumination conditions.

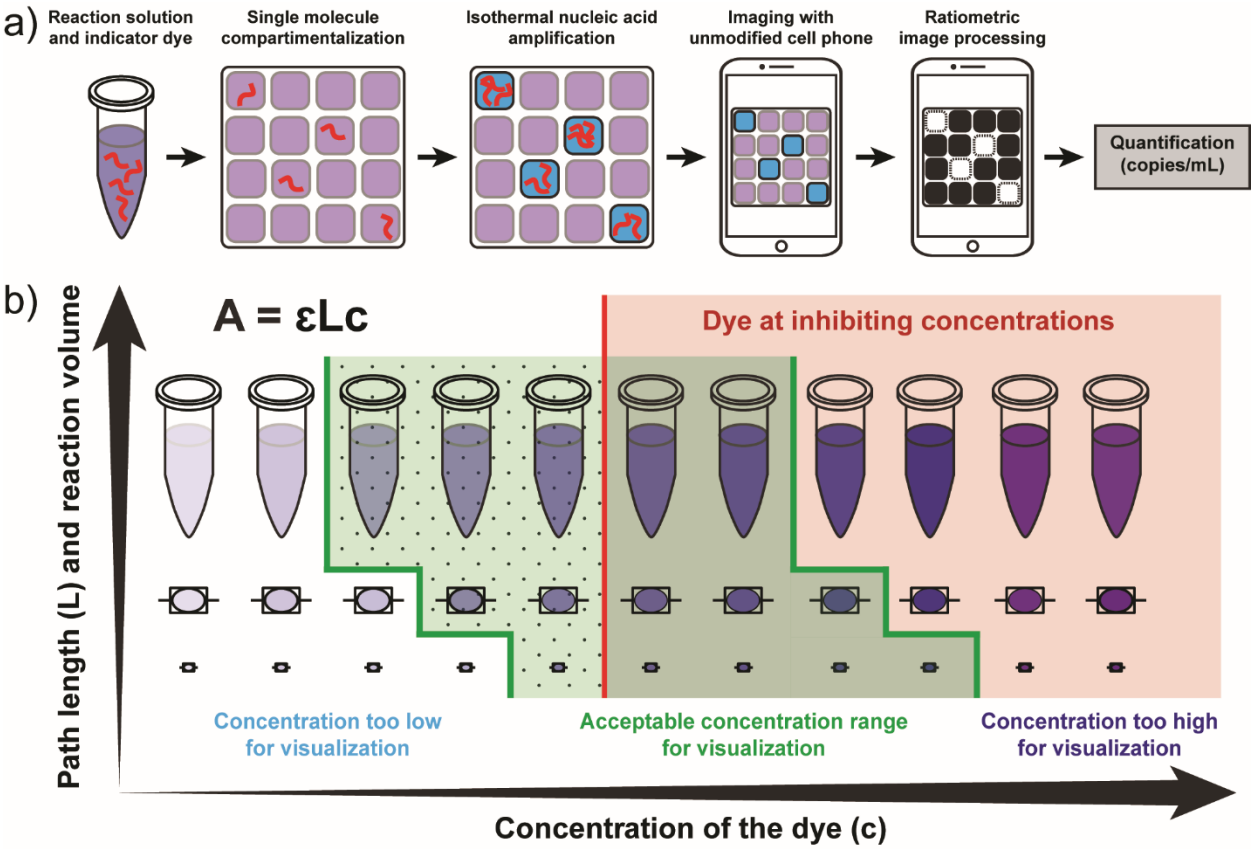

Figure 3.1 A visual readout approach for digital single-molecule isothermal amplification for use with an unmodified cell phone camera. (a) A workflow for visual readout of digital single-molecule amplification. Single nucleic acid molecules are compartmentalized on a microfluidic device with indicator dye and followed by isothermal nucleic acid amplification. Positive reaction solutions are blue; negative reactions are purple. After ratiometric image processing, positive

reactions become white and negative reactions become black, an unambiguous binary result. The number of positive wells is then used to quantify the concentration of the input target. (b) A diagram for delineating the optimal range of dye concentrations as a factor of path length (reaction volume) and the threshold for reaction inhibition. The green-shaded region indicates the range of acceptable dye concentrations for visualization with an unmodified cell phone camera. Concentrations to the left of the green region are too low for visualization; concentrations to the right of the green region are too high. Within this green region, the dotted area indicates dye concentrations that both enable readout with an unmodified cell phone camera and do not inhibit the amplification reaction. The area to the right of the red line indicates dye concentrations that interfere with amplification making accurate quantification based on real-time data challenging.

Results and Discussion

Selecting an Indicator Dye

To eliminate the need for a fluorescent readout in single-molecule amplification and produce a readout that can be imaged by any cell phone camera under various illumination conditions, one can use a nucleic acid amplification-indicator dye that changes color in response to amplification. A robust colorimetric readout balances two opposing requirements: the indicator dye must be sufficiently concentrated (or present in a large enough volume) to provide readable absorbance (*i.e.*, smaller volumes and shorter path lengths require greater concentrations of dye for sufficient absorbance to be detected), but not so concentrated that the dye interferes with the amplification reaction. To optimize a visual readout system for single-molecule counting with an unmodified cell phone camera, we first identified the factors that contribute to hypothetical limitations of a visual readout system, including the range of reaction volumes (or path lengths) at which a particular indicator could be used to monitor amplification and the range of indicator concentrations that would not interfere with the amplification reaction. Where these ranges overlap are the optimal volumes and dye concentrations at which a reaction is not inhibited and can provide a change in absorbance that is sufficient for readout with an unmodified camera phone (dotted green region of Figure 3.1b).

We validated this visual readout approach using loop-mediated isothermal amplification (LAMP)[47,48] (Supporting Information Tables TS3.1 and TS3.2) because this method has been well characterized and validated previously for single-molecule analyses.[12,14-17,49] LAMP chemistry is based on an autocycling strand displacement reaction performed at a constant temperature to synthesize large amounts of amplified product; a LAMP reaction generates more than 10^9 copies of template within 1 h of incubation at 60–65 °C.[48] We used a cubic reaction volume of 8 nL (200 × 200 × 200 μm^3), which is in the range of volumes used in digital experiments.[12,14,15,17,49] We assume that an appropriate indicator of an amplification reaction will have a change in absorbance that equates to a change of extinction coefficient of ∼25 000 L mol^{-1} cm^{-1} upon reaction (this number approaches the maximum achievable change in absorbance for small-molecule dyes). We use the Beer–Lambert law ($A = \varepsilon Lc$), which describes the relevant parameters to consider for visualization, wherein A = absorbance; ε = extinction coefficient (L mol^{-1} cm^{-1}); L = length of the light's path through the solution (cm); c = concentration of absorbing species (mol/L). At a path length of 0.2 mm, an estimated ∼2 mM concentration of the dye is required to reach a change of absorbance of 1 unit. Given these parameters, to obtain a readout that can be captured by an unmodified mobile phone, we predicted that an appropriate indicator dye would be one that responds to the incorporation of each nucleotide (present in mM concentrations), as opposed to responding only to the number of produced molecules (amplicons), which would not exceed primer concentration (present in the μM range).

Colorimetric approaches to visual detection of nucleic acid amplification typically measure absolute changes in color intensity;[50-54] however, distinguishing color change, *e.g.*, purple *vs* blue, is difficult and therefore not an appropriate way to quantify readout under variable conditions, such as in LRS. Ratiometric measurements, which take the ratio of two independent measurements under the same conditions, improve the robustness of a colorimetric approach, converting results to a yes/no binary outcome, eliminating the need for the user to differentiate colors. We hypothesized that a cell phone camera's sensor, which reads in three color channels (red, green, and blue, RGB) could provide suitable information for using a ratiometric approach to read amplification reactions at the single molecule level. The example we considered here is the back-illuminated Exmor R CMOS image

sensor[55] used on popular cell phones such as the Samsung Galaxy 4, iPhone 4S, and iPhone 5, which has a sensitivity maxima of ~520 nm (green), ~459 nm (blue), and ~597 nm (red) (Figure 3.2a).

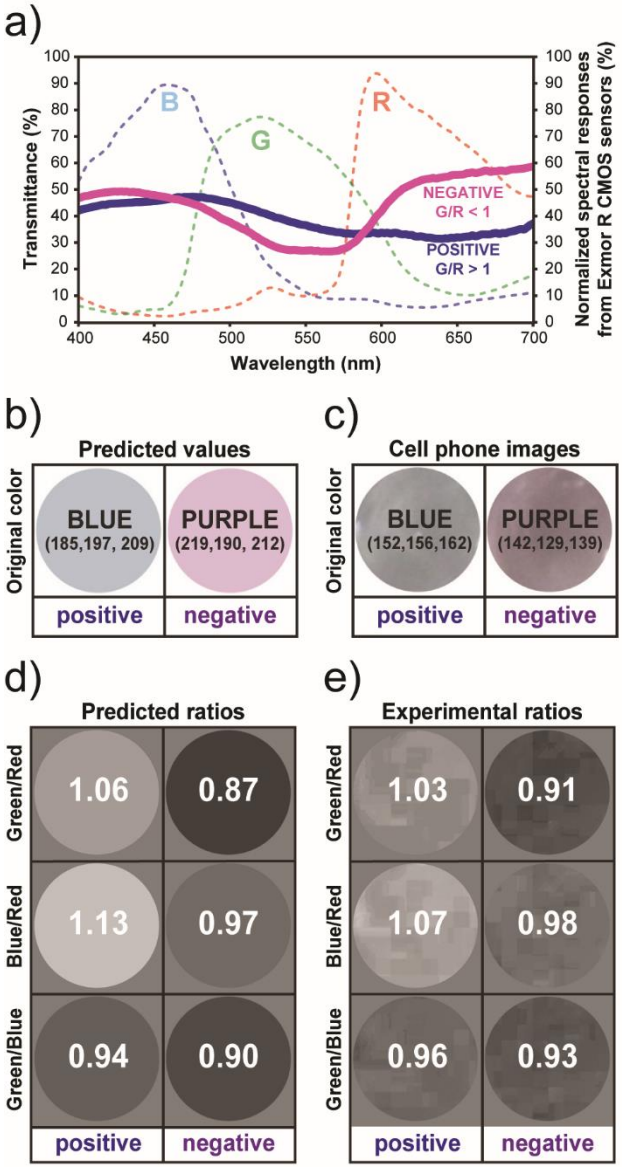

Figure 3.2 Predicted values and experimental validation of the first step of the ratiometric approach. (a) Measured spectral transmittance (%) in the range of visible light (400–700 nm) for positive (solid blue line) and negative (solid purple line) RT-LAMP reaction solutions, each containing 0.7 mM of eriochrome black T (EBT) as the amplification indicator dye. Dashed lines correspond to normalized spectral responses for red (R), green (G), and blue (B) channels of an

Exmor R CMOS sensor, a common sensor in cell phone cameras. (b–e) Analysis of the three possible RGB ratiometric combinations for positive and negative RT-LAMP reaction solutions. (b) The predicted RGB values and corresponding colors for positive and negative LAMP amplification reactions obtained by convoluting the transmittance spectrum and Exmor R spectral responses described in panel a. (c) The cropped and enlarged color images collected with an Apple iPhone 4S for positive and negative RT-LAMP reaction solutions containing 90 μM of EBT dye. (d) Predicted images and ratiometric values for positive and negative amplification reactions processed for each ratiometric combination, G/R, B/R, and G/B. (e) Experimental images and ratiometric values for positive and negative amplification reactions for each combination: G/R, B/R, and G/B. All experiments were performed with HCV RNA as template.

To illustrate our methodology for a hardware-agnostic visual readout with a ratiometric approach, we selected eriochrome black T (EBT), a magnesium ion indicator that meets the aforementioned dye specifications and has been used previously for visualization of LAMP products.[52,56] During an isothermal amplification reaction, as nucleotides are incorporated, protons and byproduct pyrophosphate ions ($P_2O_7^{4-}$) are produced, and these ions can strongly bind metal ions (*e.g.*, Mg^{2+} ions) and form insoluble salts, decreasing the concentration of metal ions in the reaction solution. Before the amplification reaction, EBT is bound to magnesium ions and the reaction solution is purple. As a LAMP reaction proceeds in the presence of target nucleic acid, it is suggested that EBT is deprived of Mg^{2+} by newly generated pyrophosphate ions, and the reaction solution turns blue.

We hypothesized that EBT would be amenable to colorimetric analysis with a cell phone camera because, in RGB terms, in a positive LAMP reaction containing EBT dye, there is a peak in the spectral transmittance in the blue channel (blue LAMP reaction solution), while in a negative LAMP reaction, transmittance remains high in the blue and red channels (purple LAMP reaction solution) (Figure 3.2a). These observed changes in transmittance between positive and negative reactions can be captured by the Exmor R optical sensor (Figure 3.2a), which matches well with the observed differences between positive and negative transmittance profiles of LAMP reactions containing EBT (Figure 3.2a).

Selecting the Optimal Ratiometric Approach

We tested whether the suitability of an indicator dye can be evaluated for a ratiometric approach prior to experimental validation by predicting the RGB values read by a cell phone camera for a positive and a negative reaction. First, we took the transmittance spectra for positive and negative amplification reactions containing EBT and convoluted them with the normalized spectral responses for each of the RGB channels in an Exmor R CMOS sensor[57] providing six curves (a positive and negative for each of the three color channels). Next, we calculated the area under each curve and took its square root (to account for the standard square-root scaling that occurs with nonscientific devices used for imaging), providing the predicted RGB values (Figure 3.2b) for positive (R = 185, G = 197, and B = 209) and negative (R = 219, G = 190, and B = 212) RT-LAMP reaction solutions in the presence of EBT at this particular concentration. These values can then be evaluated to select the optimal ratiometric approach for this particular indicator dye. In an RGB color scheme, there are three possible combinations for ratiometric analysis: G/R, B/R, or G/B. The predicted RGB values for a positive and a negative reaction are used to calculate the ratios for each channel combination (Figure 3.2d); the ratio with the greatest difference between positive and negative outcomes (G/R in this example) is predicted to be the most robust ratiometric analysis.

Using the approach described above, we predicted the RGB ratios for a positive and negative RT-LAMP reaction in the presence of two additional indicator dyes: hydroxynaphthol blue (HNB) and calmagite. HNB is being reported increasingly in the literature for LAMP visualization[50,58-61] and calmagite is an analogue of EBT dye with the nitro group absent (more stable version).[62] A side-by-side comparison showed that the greatest predicted difference between positive and negative RT-LAMP reaction, as captured by an unmodified cell phone camera, would be achieved using EBT as the indicator dye and G/R as the ratiometric combination (Figure S3.11). On the basis of these predicted ratios, we decided to validate our methodology using EBT as the indicator dye. We confirmed the storage stability of the EBT dye stock solution in the dried state (Figure S3.13), as this is a critical requirement for the use of a dye in real point-of-need diagnostic applications. EBT serves as our validation dye in this paper, however our methodology is designed to be applicable to alternative dyes.

To experimentally validate this approach of predicting an optimal ratiometric combination, we performed an RT-LAMP reaction for HCV RNA containing EBT as the indicator dye and captured an image of the readout with an unmodified camera phone (iPhone 4S) (Figure 3.2c). We processed the readout image; color channels of the original image were split and all three channel ratios (G/R, B/R, G/B) were calculated to derive a ratiometric image for each ratiometric combination. These experimental ratios obtained with an unmodified cell phone camera (Figure 3.2e) matched well with the predicted values (Figure 3.2d) for each of the three ratiometric combinations, confirming the predictive power of this approach. The G/B ratio was identified as less appropriate for distinguishing positive and negative reactions because the values for positive and negative reactions were similar; G/R and B/R ratios were identified as suitable because there was sufficient contrast between the values for positive and negative reactions. For the G/R combination, the ratio obtained after a negative reaction was 0.91 and the ratio from a positive reaction was 1.03, a difference of 0.12 (Figure 3.2e). For the B/R combination, the ratios for negative and positive reactions were 0.98 and 1.07, a difference of 0.09 (Figure 3.2e). Therefore, we selected the G/R combination for our subsequent validation experiments. Counting positives is a more intuitive approach, so the B/R ratio (where the positive ratio had the greatest difference from the background) can be a useful and attractive method. However, it is generally more desirable to select a ratio that includes the green channel because most single-chip digital image sensors used in digital cameras, including cell phones, utilize a Bayer filter mosaic pattern that is composed of 50% green, 25% red, and 25% blue pixels.[63]

To test the robustness of our approach to different hardware and illumination conditions, we used HCV RNA amplified by RT-LAMP at 2-fold increasing concentrations of indicator dye ranging from 10.9 μM to 1.4 mM (for a total of eight dye concentrations). After RT-LAMP amplification, 50 μL of each reaction solution was transferred to 96-well plates (path length of ~1.5 mm) and the readout was imaged with cameras from four common cell phone models: Apple iPhone 4S (Figure 3.3a), HTC inspire 4G (Figure 3.3b), Motorola Moto G (Figure 3.3c), and Nokia 808 PureView (Figure 3.3d). Under fluorescent light and using the G/R ratiometric process (green channel divided by red channel followed by a threshold adjustment to generate a binarized black and white image), we determined that EBT concentrations lower than 0.175 mM provided an insufficient color change

for detection with a cell phone camera (Figure 3.3, region I, white background), while concentrations of 1.4 mM inhibited the amplification reaction (Figure 3.3, region III, red background). For this particular indicator dye, the range of concentrations at which color change could be detected by an unmodified cell phone camera and no inhibition was observed at the end point of the reaction (Supporting Information Figure S3.1) was identified to be 0.175–0.7 mM (Figure 3.3, region II, green background). Some cell phone cameras were more sensitive (*e.g.*, HTC inspire 4G was able to distinguish a positive result at EBT concentrations as low as 0.0875 mM) (Figure 3.3b), but all four cell phone models distinguished a positive reaction at concentrations between 0.175 and 0.7 mM (Figure 3.3, region II, green background). We then chose one cell phone with the most representative performance (Apple iPhone 4S) to test the robustness of the G/R approach to different lighting conditions. Under all conditions tested: incandescent light (Figure 3.3e), direct sunlight (Figure 3.3f) and indirect sunlight (Figure 3.3g), the optimal EBT concentration range that we identified under fluorescent light (0.175–0.7 mM) could be read clearly, confirming the robustness of the ratiometric approach to variations in illumination.

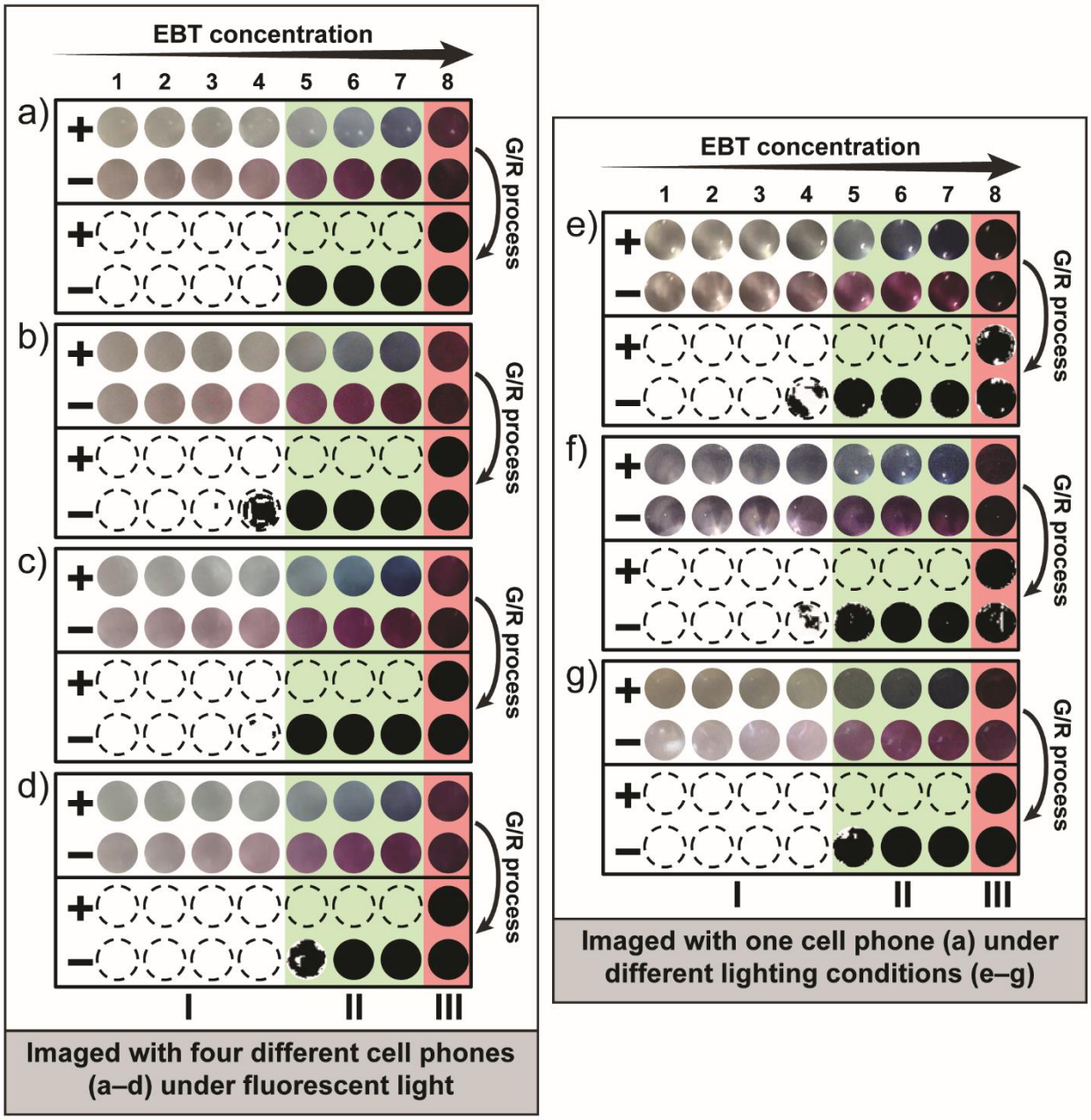

Figure 3.3 Validation of the robustness of the G/R ratiometric approach to different hardware (cell phone cameras) and lighting conditions. (a–g) Enlarged and cropped color images (top two rows of each individual panel) captured by an unmodified cell phone camera from positive (+) and negative (−) RT-LAMP reactions at 2-fold increases in EBT concentration from 10.9 μM to 1.4 mM (1 = 0.011 mM; 2 = 0.022 mM; 3 = 0.044 mM, 4 = 0.088 mM, 5 = 0.175 mM; 6 = 0.35 mM; 7 = 0.7 mM; 8 = 1.4 mM). Positive wells are blue and negative wells are purple. After G/R ratiometric

processing (bottom two rows of each individual panel), negative wells are black. Regions I, II, III in each panel indicate the effect of dye concentration: (II) acceptable concentration range for visualization (green regions); (I) concentrations too low for visualization (white regions); and (III) concentrations too high for visualization (red regions). (a–d) Images captured by four common cell phones under fluorescent light: (a) Apple iPhone 4S, (b) HTC inspire 4G, (c) Motorola Moto G, and (d) Nokia 808 PureView. (e–g) Images captured by an Apple iPhone 4S under three additional light conditions: (e) incandescent light, (f) direct sunlight, and (g) indirect sunlight. All experiments were performed with HCV RNA as a clinically relevant target. All images were acquired with unmodified cell phone cameras. Detailed information for the G/R ratiometric process (Figure S3.2) and additional cell phone camera images (Figure S3.3) are provided in the Supporting Information.

One-Step Method for Digital Visual Readout

Microfluidic devices enable ultrasensitive digital quantification. Small well volumes are valuable because they enable faster reactions (because concentrations are high in single wells), minimize the effects of inhibitory materials (due to their isolation into wells) and expand the upper limit of the dynamic range (because single molecules can be confined from samples containing high template concentrations).[18,64,65] However, as well volumes (and path lengths) decrease, color visualization becomes challenging for a mobile phone. To compensate, the concentration of the indicator dye can be increased; however, high concentrations of some dyes inhibit amplification reactions. Thus, there are inherent physical limits to a colorimetric approach. To validate that this visual readout approach could be applied to single-molecule amplification at nanoliter volumes, we used digital LAMP (dLAMP) and phage λDNA as a target. We specifically aimed to resolve three questions: (i) Can we obtain a visual readout for amplified single molecules that can be captured by an unmodified cell phone camera? (ii) Is volume a factor in achieving a digital visual readout? (iii) Does ratiometric processing work for small volumes?

To answer these questions, we designed a multivolume rotational SlipChip device containing 1240 wells of eight volumes ranging from 15 to 50 nL (Figures S3.4 and S3.5). We loaded these devices

with LAMP reaction solution containing an appropriate target concentration in the middle of the device's dynamic range, a fluorescent DNA-detecting intercalation dye (Syto 9), and EBT dye at 0.7 mM (the highest noninhibiting concentration identified in Figure 3.3). We imaged this device with a house-built real-time fluorescence imager, with a Leica stereoscope (optimal imaging conditions) and with an Apple iPhone 4S. The number of positive counts based on fluorescence was 261, while 260 positives were counted using the indicator dye and G/R process both with the stereoscope and the cell phone (Figure 3.4). This experiment showed that the G/R method could be used in place of fluorescence readout to count amplified single molecules and that the readout capture and G/R processing performed on an unmodified cell phone matched the results obtained under optimal lighting conditions (stereoscope). Additionally, using a device containing 800 wells of 27 nL, we observed excellent correlation among positive counts obtained from the stereoscope, fluorescence imager and cell phone camera (Figure S3.6).

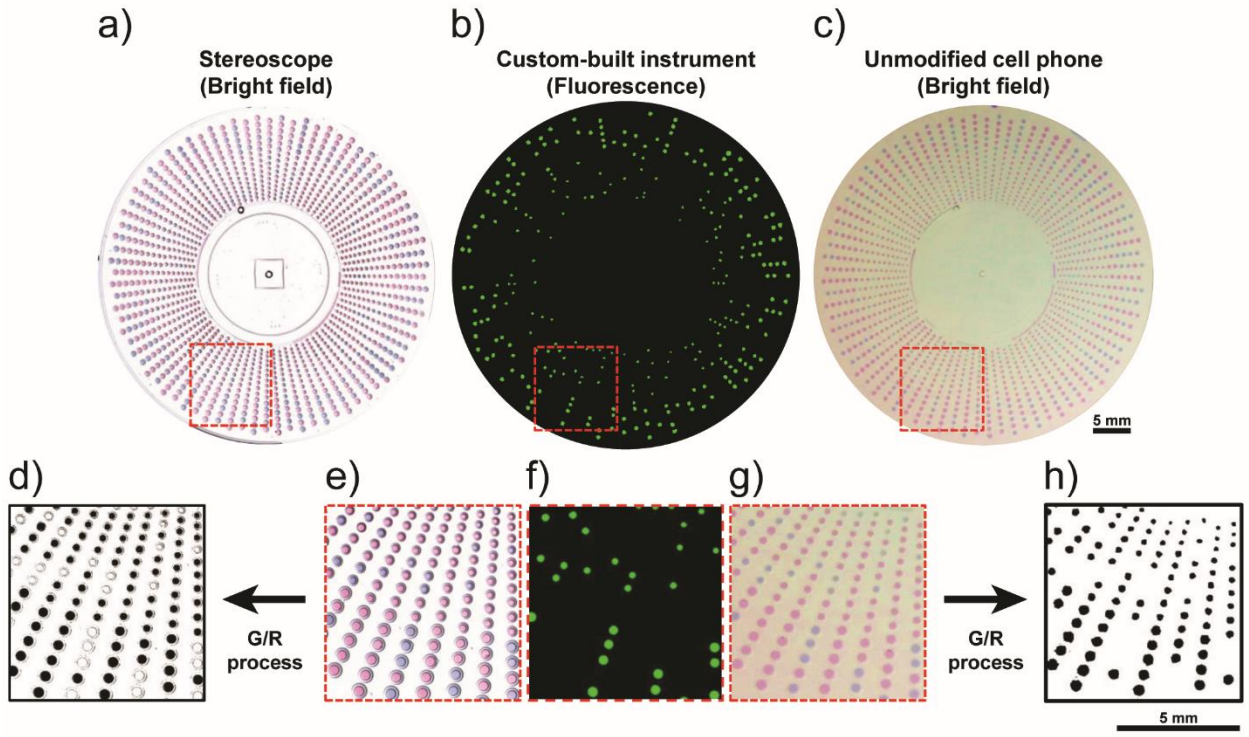

Figure 3.4 Readout from single-molecule digital LAMP reactions performed with λDNA on a multivolume rotational SlipChip device imaged by (a) a stereoscope, (b) a fluorescence microscope, and (c) an unmodified cell phone camera. (e–g) Callouts are magnified to show visual

correlation among the three imaging methods. (d) The results of the ratiometric processing for the stereoscope G/R-processed image and (h) the cell phone G/R-processed image. Colors were enhanced in these figures for clarity of publication; raw images were used in all ratiometric analyses. These devices contained 1240 wells of eight volumes ranging from 15 to 50 nL.

While investigating the limits that reaction volume may impose on visual readout, we observed that the estimated template concentration determined from each of the eight well volumes produced similar Most Probable Numbers (MPN) of molecules (mean 8500 ± 1500 copies/mL) (Figure 3.5a) (estimated concentration from all volumes are within 95% confidence interval at each volume, detailed in Figure S3.7). In addition, all SlipChip devices, analyzed independently, gave similar target concentrations (8400 ± 500 copies/mL) (Figure 3.5b), suggesting that the selected indicator dye did not impair quantification of single molecules in well sizes 15–50 nL and that these well volumes can be imaged reliably with either a stereoscope or an unmodified cell phone camera. However, the cell phone camera images of well volumes of 15 nL were less clear than those obtained from the stereoscope, suggesting that volumes of ~15 nL may approach the limit of colorimetric imaging with current camera phone sensors, although as higher quality sensors are integrated into commercial cell phones, this limit would change.

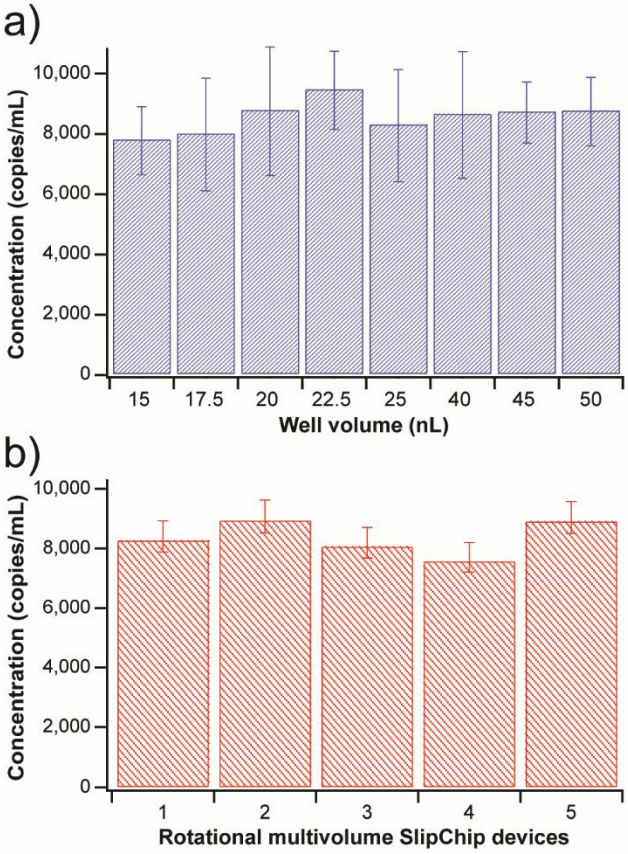

Figure 3.5 Robustness of digital visual readout at different well volumes. Concentration of λDNA was estimated by digital LAMP using five multivolume rotational SlipChip devices, each of which contained eight well volumes ranging from 15 to 50 nL. (a) Measured template concentration for each well volume averaged over five devices. (b) Mean template concentration for each of five rotational SlipChip devices. Concentrations were calculated using MPN theory[64] and error bars represent standard deviation. Images were captured by a stereoscope and processed with the ratiometric approach (G/R process).

Two-Step Method for Digital Visual Readout

We next developed a method to apply the visual readout approach to digital devices that contain smaller well volumes. To be able to image at small volumes (*e.g.*, 5 nL) on a microfluidic device,

one must balance the need for greater indicator color intensity for visualization with the need to keep dye concentrations below the level of inhibition (Figure 3.3, region III) for an amplification reaction. High concentrations of indicator dye can completely halt an amplification reaction, and we knew from performing real-time bulk experiments that even when reactions are positive, an indicator dye can still interfere to some extent with isothermal nucleic acid amplification—for both RNA and DNA, we observed delays in the time-to-positive, and this delay increased at greater concentrations of the indicator dye, even though reactions were positive (Figure S3.8). We hypothesized that we could prevent inhibition completely by decoupling the amplification step from the readout step. To do this, we designed a two-step SlipChip device (based on previous SlipChip designs)[13] (Figures S3.9 and S3.10) in which the amplification solution and the detection solution are loaded into separate wells (Figure 3.6a). We validated this two-step protocol with a clinically relevant target, purified HCV RNA, using digital reverse transcription-LAMP (dRT-LAMP). First, we performed digital isothermal amplification in the set of small (5 nL) amplification wells (in the absence of the indicator dye) (Figure 3.6a(i)). After amplification, a "slip" was performed and the amplification wells came into contact with a second set of larger (9.5 nL) wells, which contained the indicator dye, for a total well volume of 14.5 nL (Figure 3.6a(ii)). After mixing, negative wells lacking target molecules are purple and wells containing positive reactions are blue (Figure 3.6a(iii)). Counts obtained by a house-built real-time imaging instrument (to read fluorescence), and counts obtained by G/R processing from an image captured by an unmodified cell phone camera were significantly correlated (Pearson's Corr = 0.9998; R^2 = 0.9996) (Figure 3.6h), showing that this two-step SlipChip-based protocol provides a suitable visual readout for digital single-molecule amplification for devices containing wells of small volumes.

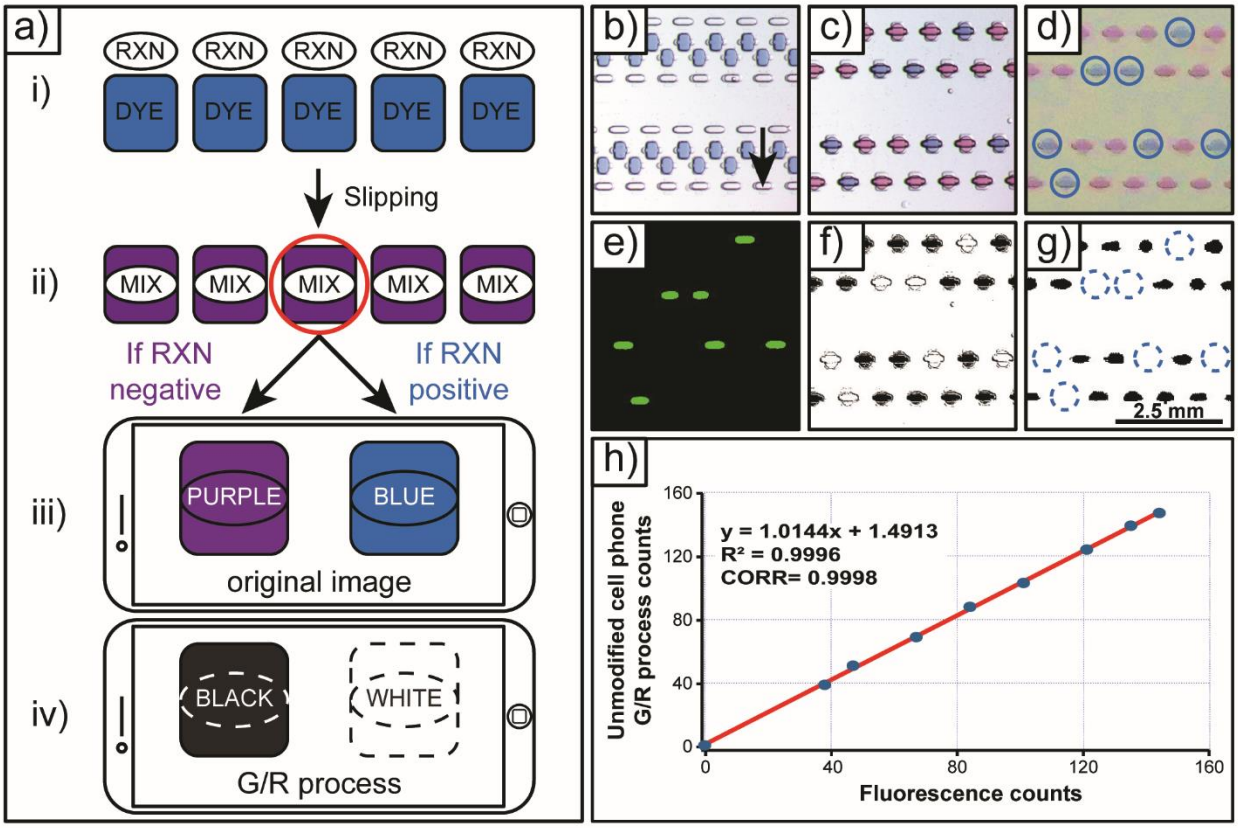

Figure 3.6 Experimental validation of two-step SlipChip devices for single molecule counting with an unmodified cell phone camera. (a) A flow-chart of detection of single molecules in two-step SlipChip: (i) 5 nL amplification wells are loaded with amplification reaction solution (RXN) and 9.5 nL detection wells are loaded with indicator dye (DYE). (ii) After amplification, a slip is performed and the RXN and DYE wells are combined. (iii) Immediately after mixing, positive reaction solutions become blue, while negative reactions remain purple. The readout is imaged by an unmodified cell phone camera. (iv) Ratiometric image processing (G/R process) provides a single binary result (positive or negative). (b) Stereoscope image of the device before the amplification and readout wells are merged (arrow designates direction of slip). (c) Stereoscope, (d) cell phone camera and (e) fluorescent images after the device is slipped and the wells are merged. (f) Stereoscope and (g) cell phone camera images after G/R image processing. (h) Correlation between fluorescence counts and cell phone (G/R processed) counts. Colors were enhanced in figure panels b–d, and f for clarity of publication; raw images were used in all ratiometric analyses. In these experiments, HCV RNA was amplified by dRT-LAMP.

Devices shown in this manuscript were not designed to achieve clinically relevant concentrations in the lower detection limit of quantification (LDL) because larger well volumes do not represent a challenge when imaging with a mobile phone. Instead, we studied the performance of our approach with wells of small volumes to ensure that this method meets the upper limit of quantification (ULQ) required for clinical relevance. The ULQ is determined by the smallest well volume and the total number of wells at that volume. As an example, for SlipChip devices with 800 wells of 5 nL, the ULQ is 1 162 413 copies/mL, while a SlipChip device with 10 000 wells of 5 nL, the ULQ is 1 622 660 (calculations performed according to Kreutz *et al.* 2011).[64]

Conclusions

Here we show that single nucleic acid molecules can be detected and counted with an unmodified cell phone camera by employing microfluidic technology, sequence-specific isothermal amplification, and a judiciously chosen amplification-indicator dye. We further show that ratiometric processing of the cell phone image enables robust quantification without the need for a user to differentiate colors. The general methodology we developed can be used as a guideline to enable others to develop their own cell phone based single-molecule counting approach. The methodology includes the following steps: First, an appropriate amplification indicator should be selected. Indicators should respond optically to each nucleotide incorporation event (as opposed to responding to the number of produced molecules) resulting in a change in the transmittance profile in the wavelength range of visible light (400–700 nm). The indicator dye should have a change in absorbance matched to the spectral sensitivity of the image sensor in an unmodified cell phone; for ratiometric processing, the solution should have a large relative change in transmittance in color channels for which the camera's image sensor is most sensitive.

Second, the color ratio used in the ratiometric approach is chosen based on the spectral sensitivity of the image sensor in an unmodified cell phone. This step can be done *in silico* to identify the dye with the ratio that provides an unambiguous binary readout of positive and negative reactions that is robust to illumination and hardware conditions. We hope others will use this algorithm to identify even

better dyes that will move this field forward. Third, the selected dye and ratiometric approach should be validated using the desired amplification chemistry. Experiments should be performed to establish the range of dye concentrations and well volumes at which an amplification reaction is not inhibited and at which imaging can be done with an unmodified cell phone. For some indicator dyes, the range of suitable well volumes and concentrations will be too narrow. In such situations, an alternative approach is to use a two-step device that separates the amplification and readout steps. Processing can be done directly on a cell phone or uploaded wirelessly to a cloud server to swiftly communicate results, as we have shown previously.[14] We anticipate that the capabilities of visual readout for counting single molecules will extend further as cell phone camera technology advances, as additional indicators are available (*e.g.*, metal ions, pH indicators) and as additional types of amplification reactions are developed. Devices that integrate sample preparation, nucleic acid amplification, and a visual digital readout that can be captured easily will be a critical breakthrough toward bringing quantitative, ultrasensitive measurements outside of central laboratories, a key step for *in vitro* diagnostics, pandemic surveillance, and environmental monitoring. We hope this work will stimulate regulatory agencies such as the FDA to consider the use of cell phones as valuable diagnostic components.

Methods

Chemicals and Materials

All chemicals were purchased from commercial sources. The LoopAmp RNA amplification kit (Eiken Chemical Co., Ltd., Japan) was purchased from SA Scientific (San Antonio, TX, USA). The LoopAmp RNA amplification kit contains 2× Reaction Mix (RM) (40 mM Tris-HCl, pH 8.8, 20 mM KCl, 16 mM $MgSO_4$, 20 mM $(NH_4)_2SO_4$, 0.2% Tween 20, 1.6 M betaine, and dNTPs 2.8 mM each), Enzyme Mix (EM) (mixture of Bst DNA polymerase and AMV reverse transcriptase), and distilled water (DW). Bovine serum albumin (BSA) was purchased from Roche Diagnostics (Indianapolis, IN, USA). Phage λDNA (500 μg), SUPERase In RNase Inhibitor (20 U/μL), Eriochrome Black T (EBT) dye, mineral oil (DNase, RNase, and Protease free), tetradecane, Costar Clear Polystyrene 96-Well Plates, Corning Universal Optical Microplate Sealing Tape, and DEPC-treated nuclease-free water were purchased from Thermo Fisher Scientific (Hanover Park, IL, USA).

Chelex 100 resin was purchased from Bio-Rad (Hercules, CA, USA). Trehalose solution (1 M) was purchased from Amersham Life Science (Cleveland, OH, USA). Tris-HCl buffer stock solution (1 M, pH 8.0) was purchased from Affymetrix (Santa Clara, CA, USA). All primers were produced by Integrated DNA Technologies (Coralville, IA, USA). Dichlorodimethylsilane was purchased from Sigma-Aldrich (St. Louis, MO, USA). SYTO 9 Stain and AcroMetrix HCV High Control were purchased from Life Technologies (Grand Island, NY, USA). Nucleic acid extraction kit QIAamp Viral RNA Mini kit was purchased from QIAGEN, Inc. (Valencia, CA, USA). Eppendorf Mastercycler Gradient PCR Themal Cycler was purchased from Eppendorf (Hamburg, Germany). POLARstar Omega microplate reader was purchased from BMG Labtech (Durham, NC, USA). Leica MZ Fl III stereoscope with PLAN 0.5× lens was purchased from Leica Microsystems (Bannockburn, IL, USA). Photomasks were designed in AutoCAD 2013 and ordered from CAD/Art Services, Inc. (Bandon, OR, USA). Soda-lime glass plates coated with layers of chromium and photoresist were ordered from the Telic Company (Valencia, CA, USA).

SlipChip Device Design

The multivolume rotational SlipChip device design was used to demonstrate the one-step method for digital visual readout; this device was composed of 1240 microfluidic wells, with the following volumes: 160 wells × 15 nL, 160 × 17.5 nL, 160 × 20 nL, 160 × 22.5 nL, 160 × 25 nL, 160 × 40 nL, 160 × 45 nL, 120 × 50 nL (Figure S3.4). The total combined volume of all wells was 35.6 μL. For loading, one inlet hole (in the middle ring structure) and four oil escape holes (in the outer ring structure) were drilled in the top plate. The two-step SlipChip device was used to demonstrate a two-step method for digital visual readout; this device was based on previously published SlipChip designs.[13] For the two-step SlipChip design used in this study, the device was modified in the following ways: (i) the number of each type of well was reduced to 800; (ii) space was added between the arrays to allow for the incubation conformation; (iii) the sequence of well loading was reversed (the smaller 5 nL wells are loaded before the larger 9.5 nL wells). See Figure S3.9 for more details. Examples of SlipChip multivolume designs for HCV and HIV viral load quantification at clinically relevant dynamic ranges[66-68] are provided in the Supporting Information (Table TS3.3).

SlipChip Device Fabrication

The procedure for fabricating the multivolume rotational SlipChip and two-step SlipChip devices was based on previous work.[69] The device features were etched to a depth of ~100 μm for the multivolume rotational SlipChip devices and ~67 μm for the two-step SlipChip devices. After etching and drilling through-holes, both devices were subjected to the same glass silanization process, previously described,[65] where the glass plates were first thoroughly cleaned with piranha solution and dried sequentially with 200 proof ethanol and nitrogen gas, and then oxidized in a plasma cleaner for 2 min and immediately transferred into a vacuum desiccator for 1.5 h for silanization with dimethyldichlorosilane. After silanization, the devices were rinsed thoroughly with chloroform, acetone, and ethanol, and dried with nitrogen gas before use. When a glass SlipChip device needed to be reused, it was first cleaned with acid piranha solution and then subjected to the same silanization and rinsing procedure described above.

Assembling and Loading SlipChips

The SlipChips used for both the dLAMP and the dRT-LAMP reactions were assembled under degassed oil (mineral oil/tetradecane 1:4 v/v). Both top and bottom plates were immersed in the oil phase and placed face to face. The two plates were aligned under a stereoscope (Leica, Germany) and stabilized using binder clips. Through-holes were drilled into the top plate to serve as fluid inlets and oil outlets in dead-end filling. The reagent solutions were loaded through the inlets by pipetting.

HCV Viral RNA Purification from AcroMetrix HCV High Control

A total of 200 μL of plasma containing HCV RNA (viral load estimate provided by AcroMetrix: 1.1–3.5 IU/mL) was extracted using the QIAamp Viral RNA Mini Kit (QIAGEN, Inc., Valencia, CA, USA) according to the manufacturer's instructions. The elution volume was 60 μL. The purified HCV viral RNA was analyzed immediately or stored at −80 °C until further analysis.

Preparation of EBT Solution

The EBT stock solutions were prepared by dissolving EBT dye in deionized water. The aqueous solution was sonicated for 10–20 min and the free volume was filled with argon gas and mixed on a rotator at 65 °C for 1 h. To remove any potential impurities from the EBT dye, Chelex 100 ion-exchange resin was added to the resulting solution (5% w/v) and placed on rotator for 1 h. Resin was centrifuged at 3000 rpm for 5 min and the top fraction was collected in a Falcon tube, flushed with argon, and stored at room temperature for no more than 2 days. A comparison of EBT, HNB, and calmagite indicator dye stock solutions before and after treatment with Chelex 100 is provided in the Supporting Information (Figure S3.12).

Storage Stability of Amplification Indicator Dyes by Drying in the Presence of Stabilizer Trehalose

EBT, HNB, and calmagite stock solutions at 0.7 mM were prepared by dissolving the dyes in 20 mM Tris-HCl buffer (pH 8.8) and adding 30 mM of trehalose. The solutions were sonicated for 10 min and mixed on a rotator at room temperature for 1 h. Chelex 100 ion-exchange resin was added (5% w/v) and placed on rotator for 1 h. Resin was centrifuged at 3000 rpm for 5 min and the top fraction was collected in a Falcon tube. The resulting stock solutions were transferred to a Costar Clear Polystyrene 96-Well Plate (40 μL per well) and sealed with Corning Universal Optical Microplate Sealing Tape before spectrophotometric analysis (time 0 h). Immediately after analysis, the sealing cover was removed and the plate was placed in a desiccator under vacuum overnight until the dye stock solutions were completely dry. Then, at 24-h time points over the next 120 h (for a total of 5 time points), three wells of each dried amplification indicator solution were resuspended with 40 μL of deionized water and spectrophotometric analyses were performed. After each measurement, the plate was sealed again (to prevent hydration of the dried solutions in the other wells) and kept in the dark at room temperature. The absorption spectra analyses were performed using the POLARstar Omega microplate reader with Omega Data analysis software. Absorbance in the range of 400–700 nm was recorded at 2 nm intervals. Blank solutions (20 mM Tris-HCl buffer with 30 mM trehalose) were also loaded at time 0 h, desiccated after the first measurement, and

treated as the rest of the solutions. The measured spectral absorbance from these control solutions was subtracted at each time point from the plotted data (Figure S3.13).

RT-LAMP Amplification of HCV RNA in-Tube

The purified HCV RNA described above was used for in-tube RT-LAMP amplification. The RT-LAMP mix contained the following: 20 μL of RM, 2 μL of EM, 2 μL of SYTO 9 Stain from a 40 μM stock, 4 μL of LAMP primer mixture (20 μM BIP/FIP, 10 μM LB/LF, and 2.5 μM B3/F3), 1 μL of SUPERase In RNase Inhibitor (20 U/μL), EBT solutions of various concentrations and with various amounts of RNA template solution, and enough nuclease-free water to bring the volume to 40 μL. The solution was loaded into 0.2 mL PCR tubes and heated at 63 °C for 50 min and 85 °C for 5 min (heat inactivation) on an Eppendorf Mastercycler Gradient PCR Themal Cycler.

Spectrophotometric Analysis for Positive and Negative RT-LAMP Reactions

Fifty microliters of positive and negative RT-LAMP reaction solutions containing 0.7 mM of EBT, HNB, and calmagite dyes was transferred to a Costar Clear Polystyrene 96-Well Plate, the plate was sealed with a Corning Universal Optical Microplate Sealing Tape and then used for spectrophotometric analysis. An absorption spectra analysis was performed using the POLARstar Omega microplate reader with Omega Data analysis software. The instrument was first set to zero at 700 nm for distilled water, and absorbance in the range of 400–700 nm was recorded at 2 nm intervals. Transmittance was calculated from absorbance values using the following equation: $T = 10^{(2-A)}$.

Prediction of RGB Values

Predicted RGB values for a positive and negative LAMP amplification reaction containing EBT were calculated as follows: (i) The spectral response curves for an Exmor R CMOS image sensor were available only in a graphical format, so data was extracted using Plot Digitizer (ver. 2.6.6) and new plots were generated. (ii) The area under the curve for each of the three color channel spectra was normalized (selecting 1000 arbitrary values under each curve). Uniform white-balanced light source was assumed. (iii) Convolution of the spectral transmittance spectral profiles of the indicator

dye for a positive and a negative LAMP reaction solution (experimentally obtained) with the normalized spectral responses from the Exmor R CMOS image sensor was performed. We ignored the light scattering caused by pyrophosphate release during the amplification reaction. As a result, six curves were generated (a positive and negative for each of the three color channels). (iv) The area under each curve was calculated and its square root taken, providing the predicted RGB values for positive and negative RT-LAMP reaction solutions in the presence of EBT at this particular concentration.

dLAMP Amplification of Phage λDNA on Multivolume Rotational SlipChip Devices

To amplify λ phage DNA using dLAMP method, the LAMP mix contained the following: 20 μL of RM, 2 μL of EM, 2 μL of SYTO 9 Stain from 40 μM stock, 4 μL of primer mixture (20 μM BIP/FIP, 10 μM LB/LF, and 2.5 μM B3/F3), 2 μL of BSA (20 mg/mL), various amounts of DNA template solution, 4.7 μL of 6 mM EBT dye (0.7 mM final concentration), and enough nuclease-free water to bring the volume to 40 μL. The solution was loaded onto a multivolume rotational SlipChip device and heated at 63 °C for 50 min on flat block PCR machine (Eppendorf Mastercycler). Five minutes of heating at 85 °C was used to stop the reaction.

Real-Time dRT-LAMP of HCV RNA on Two-Step SlipChip Devices

To amplify HCV viral RNA using dRT-LAMP method on house-built real-time instrument, the RT-LAMP mix contained the following: 20 μL of RM, 2 μL of EM, 2 μL of SYTO 9 Stain from 40 μM stock, 4 μL of primer mixture (20 μM BIP/FIP, 10 μM LB/LF, and 2.5 μM B3/F3), 2 μL of BSA (20 mg/mL), 1 μL of SUPERase In RNase inhibitor, various amounts of RNA template solution, and enough nuclease-free water to bring the volume to 40 μL. The solution was loaded into the 5 nL wells of two-step SlipChip devices. Other set of wells (9.5 nL) were loaded with 2.4 mM solution of EBT solution (1.57 mM final concentration). SlipChips were heated at 63 °C for 50 min on a house-built real-time instrument; reactions were stopped by heating to 85 °C for 5 min.

House-Built Real-Time Instrument Imaging

Experiments were performed on a Bio-Rad PTC-200 thermocycler with a custom machined block. The block contains a flat 3 × 3 $in.^2$ portion onto which the devices are placed ensuring optimal thermal contact. The excitation light source used was a Philips Luxeon S (LXS8-PW30) 1315 lm LED module with a Semrock filter (FF02-475). Image acquisition was performed with a VX-29MG camera and a Zeiss Macro Planar T F2-100mm lens. A Semrock filter (FF01-540) was used as an emission filter. Images acquired were analyzed using LabVIEW software.

House-Built Real-Time Instrument Data Analysis

Fluorescent images were analyzed using self-developed LabVIEW software. The data were analyzed by first creating a binary mask that defined the location of each reaction volume within the image. The masked spots were then overlaid on the stack of images collected over the course of the experiment and the average intensity of each individual masked spot was tracked over the course of the stack. Background subtraction of the real-time trace was performed by creating a least mean square fit of each individual trace. Threshold was then manually set at the half height of the averaged maximum intensity, and the time-to-positive of each reaction was then determined as the point at which the real-time curve crossed the defined threshold.

Bright-Field Image Acquisition

A mobile phone was used to capture the readout under standard fluorescent light, using the camera's default autofocus and autoexposure settings. Photographs of the 96-well plate were also taken using alternate commercial cell phones and under different lighting conditions (Figure 3.3 and Figure S3.3). Stereoscope imaging was done using Leica MZ Fl III stereoscope with a PLAN 0.5× lens. The stereoscope was equipped with a Diagnostic Instruments color mosaic model 11.2-megapixel camera and images were acquired using Spot imaging software. An automatic white-balance adjustment was done for each image using Spot software. Multiple images were acquired to capture all wells in the device, and assembled to form a complete image of the device to compare with the image acquired from the cell phone camera by using the freeware Image Composite Editor (ver. 2.0).

Bright Field Image Processing and Data Analysis

Images acquired with cell phone and stereoscope were processed using open source ImageJ software (ver.1.49) according to the standard procedure. Briefly: (i) white balance was corrected as needed, (ii) color channels of the original image were split, (iii) one channel was divided by a second channel (*e.g.*, green channel divided by the red channel in the G/R approach) to derive a ratiometric image, and (iv) automatic thresholding was applied to make a binary (black and white) image. Semiautomatic counting on the two-step SlipChip images was accomplished using a freeware Fiji image processing. Acquired bright field images for the multivolume rotational SlipChips were counted manually.

References

1. A. Calmy, N. Ford, B. Hirschel, S. J. Reynolds, L. Lynen, E. Goemaere, F. G. de la Vega, L. Perrin, and W. Rodriguez, "HIV viral load monitoring in resource-limited regions: Optional or necessary?," *Clinical Infectious Diseases*, **2007**, 44, 128-134.
2. A. Johannessen, "Where we are with point-of-care testing," *Journal of viral hepatitis*, **2015**, 22, 362-365.
3. S. Wang, F. Xu, and U. Demirci, "Advances in developing HIV-1 viral load assays for resource-limited settings," *Biotechnology Advances*, **2010**, 28, 770-781.
4. P. Yager, T. Edwards, E. Fu, K. Helton, K. Nelson, M. R. Tam, and B. H. Weigl, "Microfluidic diagnostic technologies for global public health," *Nature*, **2006**, 442, 412-418.
5. R. W. Peeling, K. K. Holmes, D. Mabey, and A. Ronald, "Rapid tests for sexually transmitted infections (STIs): the way forward," *Sex Transm Infect*, **2006**, 82 Suppl 5, v1-6.
6. P. Yager, G. J. Domingo, and J. Gerdes, "Point-of-Care Diagnostics for Global Health," *Annual Review of Biomedical Engineering*, **2008**, 10, 107-144.
7. A. Niemz, T. M. Ferguson, and D. S. Boyle, "Point-of-care nucleic acid testing for infectious diseases," *Trends Biotechnol*, **2011**, 29, 240-250.

8. N. K. Thom, K. Yeung, M. B. Pillion, and S. T. Phillips, "“Fluidic batteries” as low-cost sources of power in paper-based microfluidic devices," *Lab on a Chip*, **2012**, 12, 1768-1770.

9. P. LaBarre, J. Gerlach, J. Wilmoth, A. Beddoe, J. Singleton, and B. Weigl, "*Non-instrumented nucleic acid amplification (NINA): instrument-free molecular malaria diagnostics for low-resource settings*," 2010 Annual International Conference of the IEEE Engineering in Medicine and Biology, IEEE, **2010**.

10. K. A. Curtis, D. L. Rudolph, I. Nejad, J. Singleton, A. Beddoe, B. Weigl, P. LaBarre, and S. M. Owen, "Isothermal amplification using a chemical heating device for point-of-care detection of HIV-1," *PLoS One*, **2012**, 7, e31432.

11. C. Liu, M. G. Mauk, R. Hart, X. Qiu, and H. H. Bau, "A self-heating cartridge for molecular diagnostics," *Lab on a Chip*, **2011**, 11, 2686-2692.

12. B. Sun, F. Shen, S. E. McCalla, J. E. Kreutz, M. A. Karymov, and R. F. Ismagilov, "Mechanistic evaluation of the pros and cons of digital RT-LAMP for HIV-1 viral load quantification on a microfluidic device and improved efficiency via a two-step digital protocol," *Analytical Chemistry*, **2013**, 85, 1540-1546.

13. F. Shen, E. K. Davydova, W. B. Du, J. E. Kreutz, O. Piepenburg, and R. F. Ismagilov, "Digital isothermal quantification of nucleic acids via simultaneous chemical initiation of recombinase polymerase amplification reactions on SlipChip," *Analytical Chemistry*, **2011**, 83, 3533-3540.

14. D. A. Selck, M. A. Karymov, B. Sun, and R. F. Ismagilov, "Increased robustness of single-molecule counting with microfluidics, digital isothermal amplification, and a mobile phone versus real-time kinetic measurements," *Analytical Chemistry*, **2013**, 85, 11129-11136.

15. B. Sun, J. Rodriguez-Manzano, D. A. Selck, E. Khorosheva, M. A. Karymov, and R. F. Ismagilov, "Measuring fate and rate of single-molecule competition of amplification and restriction digestion, and its use for rapid genotyping tested with hepatitis C viral RNA," *Angewandte Chemie-International Edition*, **2014**, 53, 8088-8092.

16. Q. Y. Zhu, Y. B. Gao, B. W. Yu, H. Ren, L. Qiu, S. H. Han, W. Jin, Q. H. Jin, and Y. Mu, "Self-priming compartmentalization digital LAMP for point-of-care," *Lab on a Chip*, **2012**, 12, 4755-4763.
17. A. Gansen, A. M. Herrick, I. K. Dimov, L. P. Lee, and D. T. Chiu, "Digital LAMP in a sample self-digitization (SD) chip," *Lab on a Chip*, **2012**, 12, 2247-2254.
18. D. Witters, B. Sun, S. Begolo, J. Rodriguez-Manzano, W. Robles, and R. F. Ismagilov, "Digital biology and chemistry," *Lab on a Chip*, **2014**, 14, 3225-3232.
19. J. M. Sidorova, N. Li, D. C. Schwartz, A. Folch, and R. J. Monnat Jr, "Microfluidic-assisted analysis of replicating DNA molecules," *Nature protocols*, **2009**, 4, 849.
20. H.-P. Chou, C. Spence, A. Scherer, and S. Quake, "A microfabricated device for sizing and sorting DNA molecules," *Proceedings of the National Academy of Sciences*, **1999**, 96, 11-13.
21. J. S. Marcus, W. F. Anderson, and S. R. Quake, "Microfluidic single-cell mRNA isolation and analysis," *Analytical Chemistry*, **2006**, 78, 3084-3089.
22. E. A. Ottesen, J. W. Hong, S. R. Quake, and J. R. Leadbetter, "Microfluidic digital PCR enables multigene analysis of individual environmental bacteria," *Science*, **2006**, 314, 1464-1467.
23. N. R. Beer, B. J. Hindson, E. K. Wheeler, S. B. Hall, K. A. Rose, I. M. Kennedy, and B. W. Colston, "On-chip, real-time, single-copy polymerase chain reaction in picoliter droplets," *Analytical Chemistry*, **2007**, 79, 8471-8475.
24. M. M. Kiss, L. Ortoleva-Donnelly, N. R. Beer, J. Warner, C. G. Bailey, B. W. Colston, J. M. Rothberg, D. R. Link, and J. H. Leamon, "High-Throughput Quantitative Polymerase Chain Reaction in Picoliter Droplets," *Analytical Chemistry*, **2008**, 80, 8975-8981.
25. S. O. Sundberg, C. T. Wittwer, C. Gao, and B. K. Gale, "Spinning Disk Platform for Microfluidic Digital Polymerase Chain Reaction," *Analytical Chemistry*, **2010**, 82, 1546-1550.
26. E. Lagally, I. Medintz, and R. Mathies, "Single-molecule DNA amplification and analysis in an integrated microfluidic device," *Analytical chemistry*, **2001**, 73, 565-570.
27. F. Shen, W. Du, J. E. Kreutz, A. Fok, and R. F. Ismagilov, "Digital PCR on a SlipChip," *Lab on a Chip*, **2010**, 10, 2666-2672.

28. C. D. Chin, V. Linder, and S. K. Sia, "Lab-on-a-chip devices for global health: Past studies and future opportunities," *Lab on a Chip*, **2007**, 7, 41-57.
29. C. D. Chin, T. Laksanasopin, Y. K. Cheung, D. Steinmiller, V. Linder, H. Parsa, J. Wang, H. Moore, R. Rouse, and G. Umviligihozo, "Microfluidics-based diagnostics of infectious diseases in the developing world," *Nature Medicine*, **2011**, 17, 1015.
30. C. D. Chin, V. Linder, and S. K. Sia, "Commercialization of microfluidic point-of-care diagnostic devices," *Lab on a Chip*, **2012**, 12, 2118-2134.
31. International Telecommunication Union. "ICT Facts and Figures - the World in 2015," http://www.itu.int/en/ITU-D/Statistics/Pages/facts/default.aspx, **2015**.
32. G. M. Whitesides, "A Glimpse into the Future of Diagnostics," *Clinical Chemistry*, **2013**, 59, 589-591.
33. B. Berg, B. Cortazar, D. Tseng, H. Ozkan, S. Feng, Q. Wei, R. Y.-L. Chan, J. Burbano, Q. Farooqui, and M. Lewinski, "Cellphone-based hand-held microplate reader for point-of-care testing of enzyme-linked immunosorbent assays," *ACS Nano*, **2015**, 9, 7857-7866.
34. Q. Wei, W. Luo, S. Chiang, T. Kappel, C. Mejia, D. Tseng, R. Y. L. Chan, E. Yan, H. Qi, F. Shabbir, H. Ozkan, S. Feng, and A. Ozcan, "Imaging and Sizing of Single DNA Molecules on a Mobile Phone," *ACS Nano*, **2014**, 8, 12725-12733.
35. T. Laksanasopin, T. W. Guo, S. Nayak, A. A. Sridhara, S. Xie, O. O. Olowookere, P. Cadinu, F. Meng, N. H. Chee, J. Kim, C. D. Chin, E. Munyazesa, P. Mugwaneza, A. J. Rai, V. Mugisha, A. R. Castro, D. Steinmiller, V. Linder, J. E. Justman, S. Nsanzimana, and S. K. Sia, "A smartphone dongle for diagnosis of infectious diseases at the point of care," *Science Translational Medicine*, **2015**, 7, 273re271-273re271.
36. A. K. Yetisen, M. S. Akram, and C. R. Lowe, "Paper-based microfluidic point-of-care diagnostic devices," *Lab on a Chip*, **2013**, 13, 2210-2251.
37. J. D. Besant, J. Das, I. B. Burgess, W. Liu, E. H. Sargent, and S. O. Kelley, "Ultrasensitive visual read-out of nucleic acids using electrocatalytic fluid displacement," *Nature Communications*, **2015**, 6, 6978.
38. A. W. Martinez, S. T. Phillips, E. Carrilho, S. W. Thomas, H. Sindi, and G. M. Whitesides, "Simple telemedicine for developing regions: Camera phones and paper-

based microfluidic devices for real-time, off-site diagnosis," *Analytical Chemistry*, **2008**, 80, 3699-3707.

39. A. W. Martinez, S. T. Phillips, G. M. Whitesides, and E. Carrilho, "Diagnostics for the Developing World: Microfluidic Paper-Based Analytical Devices," *Analytical Chemistry*, **2010**, 82, 3-10.
40. T. S. Park, W. Y. Li, K. E. McCracken, and J. Y. Yoon, "Smartphone quantifies Salmonella from paper microfluidics," *Lab on a Chip*, **2013**, 13, 4832-4840.
41. S. K. Vashist, O. Mudanyali, E. M. Schneider, R. Zengerle, and A. Ozcan, "Cellphone-based devices for bioanalytical sciences," *Analytical and Bioanalytical Chemistry*, **2014**, 406, 3263-3277.
42. D. J. You, T. S. Park, and J. Y. Yoon, "Cell-phone-based measurement of TSH using Mie scatter optimized lateral flow assays," *Biosensors & Bioelectronics*, **2013**, 40, 180-185.
43. L. Shen, J. A. Hagen, and I. Papautsky, "Point-of-care colorimetric detection with a smartphone," *Lab on a Chip*, **2012**, 12, 4240-4243.
44. E. A. Tyburski, S. E. Gillespie, W. A. Stoy, R. G. Mannino, A. J. Weiss, A. F. Siu, R. H. Bulloch, K. Thota, A. Cardenas, W. Session, H. J. Khoury, S. O'Connor, S. T. Bunting, J. Boudreaux, C. R. Forest, M. Gaddh, T. Leong, L. A. Lyon, and W. A. Lam, "Disposable platform provides visual and color-based point-of-care anemia self-testing," *The Journal of Clinical Investigation*, **2014**, 124, 4387-4394.
45. A. Garcia, M. M. Erenas, E. D. Marinetto, C. A. Abad, I. de Orbe-Paya, A. J. Palma, and L. F. Capitan-Vallvey, "Mobile phone platform as portable chemical analyzer," *Sensors and Actuators B-Chemical*, **2011**, 156, 350-359.
46. S. Q. Wang, X. H. Zhao, I. Khimji, R. Akbas, W. L. Qiu, D. Edwards, D. W. Cramer, B. Ye, and U. Demirci, "Integration of cell phone imaging with microchip ELISA to detect ovarian cancer HE4 biomarker in urine at the point-of-care," *Lab on a Chip*, **2011**, 11, 3411-3418.
47. K. Nagamine, T. Hase, and T. Notomi, "Accelerated reaction by loop-mediated isothermal amplification using loop primers," *Molecular and Cellular Probes*, **2002**, 16, 223-229.

48. T. Notomi, H. Okayama, H. Masubuchi, T. Yonekawa, K. Watanabe, N. Amino, and T. Hase, "Loop-mediated isothermal amplification of DNA," *Nucleic Acids Research*, **2000**, 28.

49. G. Nixon, J. A. Garson, P. Grant, E. Nastouli, C. A. Foy, and J. F. Huggett, "Comparative Study of Sensitivity, Linearity, and Resistance to Inhibition of Digital and Nondigital Polymerase Chain Reaction and Loop Mediated Isothermal Amplification Assays for Quantification of Human Cytomegalovirus," *Analytical Chemistry*, **2014**, 86, 4387-4394.

50. M. Goto, E. Honda, A. Ogura, A. Nomoto, and K.-I. Hanaki, "Colorimetric detection of loop-mediated isothermal amplification reaction by using hydroxy naphthol blue," *BioTechniques*, **2009**, 46, 167-172.

51. N. A. Tanner, Y. Zhang, and T. C. E. Jr., "Visual detection of isothermal nucleic acid amplification using pH-sensitive dyes," *BioTechniques*, **2015**, 58, 59-68.

52. D. G. Wang, "Visual detection of Mycobacterium tuberculosis complex with loop-mediated isothermal amplification and Eriochrome Black T," *Materials, Machines and Development of Technologies for Industrial Production*, **2014**, 618, 264-267.

53. A. K. Yetisen, J. L. Martinez-Hurtado, A. Garcia-Melendrez, F. D. Vasconcellos, and C. R. Lowe, "A smartphone algorithm with inter-phone repeatability for the analysis of colorimetric tests," *Sensors and Actuators B-Chemical*, **2014**, 196, 156-160.

54. M. Safavieh, M. U. Ahmed, E. Sokullu, A. Ng, L. Braescu, and M. Zourob, "A simple cassette as point-of-care diagnostic device for naked-eye colorimetric bacteria detection," *Analyst*, **2014**, 139, 482-487.

55. Sony Corp. "2010 Sony "Exmor R" Cmos Image Sensors Achieve a Dramatic Increase in Performance," http://www.sony.net/Products/SC-HP/cx_news_archives/img/pdf/vol_59/featuring_Exmorr.pdf, **2010**.

56. S. J. Oh, B. H. Park, J. H. Jung, G. Choi, D. C. Lee, and T. S. Seo, "Centrifugal loop-mediated isothermal amplification microdevice for rapid, multiplex and colorimetric foodborne pathogen detection," *Biosensors and Bioelectronics*, **2016**, 75, 293-300.

57. Sony Corp. "2011 High Picture Quality Cellular Phone CMOS Image Sensors Feature Full HD Video," http://www.sony.net/Products/SC-HP/cx_news_archives/img/pdf/vol_65/imx081_091_111pq.pdf, **2011**.

58. X.-J. Ma, Y.-L. Shu, K. Nie, M. Qin, D.-Y. Wang, R.-B. Gao, M. Wang, L.-Y. Wen, F. Han, and S.-M. Zhou, "Visual detection of pandemic influenza A H1N1 Virus 2009 by reverse-transcription loop-mediated isothermal amplification with hydroxynaphthol blue dye," *Journal of Virological Methods*, **2010**, 167, 214-217.

59. K. Nie, X. Zhao, X. Ding, X. Li, S. Zou, J. Guo, D. Wang, R. Gao, X. Li, and W. Huang, "Visual detection of human infection with influenza A (H 7 N 9) virus by subtype-specific reverse transcription loop-mediated isothermal amplification with hydroxynaphthol blue dye," *Clinical Microbiology and Infection*, **2013**, 19, E372-E375.

60. Y.-B. Duan, C.-Y. Ge, X.-K. Zhang, J.-X. Wang, and M.-G. Zhou, "Development and evaluation of a novel and rapid detection assay for Botrytis cinerea based on loop-mediated isothermal amplification," *PLoS One*, **2014**, 9, e111094.

61. B.-Y. Yang, X.-L. Liu, Y.-M. Wei, J.-Q. Wang, X.-Q. He, Y. Jin, and Z.-J. Wang, "Rapid and sensitive detection of human astrovirus in water samples by loop-mediated isothermal amplification with hydroxynaphthol blue dye," *BMC Microbiology*, **2014**, 14, 38.

62. F. Lindstrom and H. Diehl, "Indicator for the titration of calcium plus magnesium with (ethylenedinitrilo) tetraacetate," *Analytical Chemistry*, **1960**, 32, 1123-1127.

63. B. E. Bayer, *"*Color imaging array,*" US Pat.* 3,971,065, **1976**.

64. J. E. Kreutz, T. Munson, T. Huynh, F. Shen, W. B. Du, and R. F. Ismagilov, "Theoretical design and analysis of multivolume digital assays with wide dynamic range validated experimentally with microfluidic digital PCR," *Analytical Chemistry*, **2011**, 83, 8158-8168.

65. F. Shen, B. Sun, J. E. Kreutz, E. K. Davydova, W. B. Du, P. L. Reddy, L. J. Joseph, and R. F. Ismagilov, "Multiplexed quantification of nucleic acids with large dynamic range using multivolume digital RT-PCR on a rotational SlipChip tested with HIV and hepatitis C viral load," *Journal of the American Chemical Society*, **2011**, 133, 17705-17712.

66. M. Arnedo, E. Alonso, N. Eisenberg, L. Ibáñez, C. Ferreyra, A. Jaén, L. Flevaud, S. Khamadi, P. Roddy, J. M. Gatell, D. Dalmau, and O. R. S. G. Busia, "Monitoring HIV viral load in resource limited settings: still a matter of debate?," *PloS One*, **2012**, 7, e47391-e47391.

67. E. R. Feeney and R. T. Chung, "Antiviral treatment of hepatitis C," *BMJ: British Medical Journal*, **2014**, 349, g3308.

68. B. Cobb, P. J. Pockros, R. A. Vilchez, and J. M. Vierling, "HCV RNA Viral Load Assessments in the Era of Direct-Acting Antivirals," *American Journal of Gastroenterology*, **2013**, 108, 471-475.

69. W. B. Du, L. Li, K. P. Nichols, and R. F. Ismagilov, "SlipChip," *Lab on a Chip*, **2009**, 9, 2286-2292.

Supplementary Information

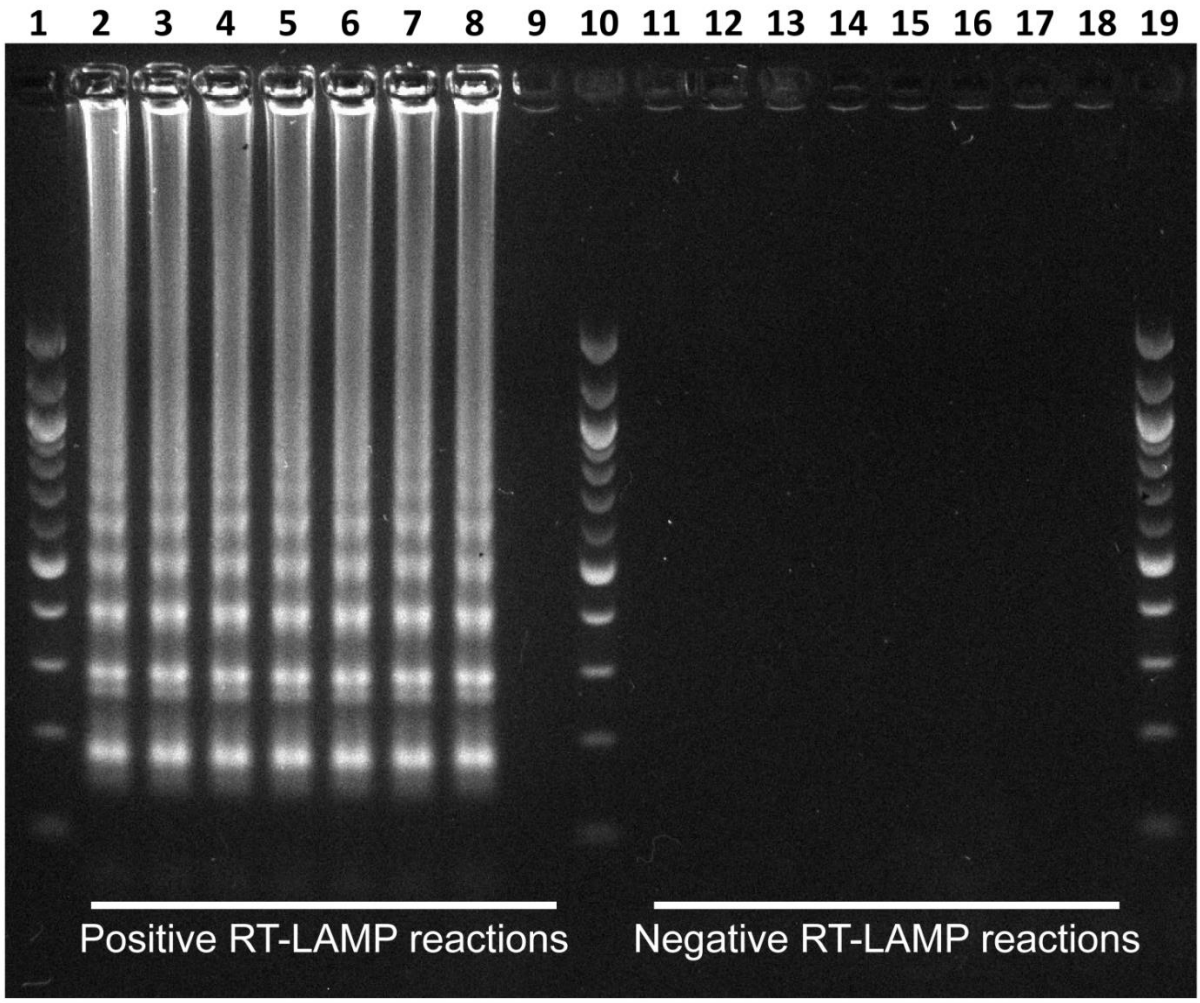

Figure S3.1 DNA gel electrophoresis for RT-LAMP product. Lanes 1, 10 and 19 are 100 bp DNA ladders. Lanes 2–9 are positive (HCV RNA) RT-LAMP reactions at two-fold increased EBT solution concentration (from 0.011 to 1.4 mM). Lanes 11–18 are negative RT-LAMP reactions at two-fold increased EBT solution concentration (from 0.011 to 1.4 mM). Lane 9 shows an inhibited RT-LAMP reaction in the presence of 1.4 mM EBT solution.

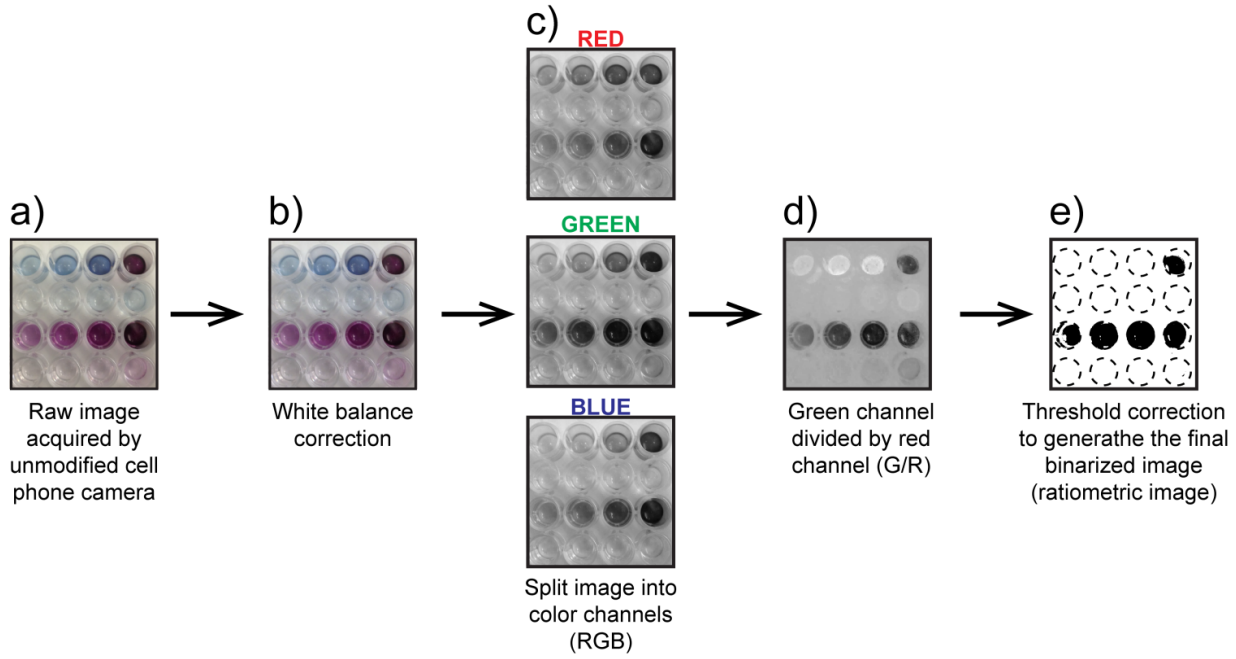

Figure S3.2 Each step of the G/R process algorithm. This experiment was performed with HCV RNA as a clinically relevant target and the raw image was acquired with an Apple iPhone 4S under fluorescent light. The top row of each panel (eight wells) shows a positive RT-LAMP reaction containing EBT solution at two-fold increasing concentrations from 10.9 µM to 1.4 mM (from left to right). The bottom row of each panel (eight wells) shows negative RT-LAMP reactions containing EBT solution at two-fold increasing concentrations from 10.9 µM to 1.4 mM. a). A raw image acquired by a cell phone camera. b) The same image after white balance correction. c) Red, green and blue color channels separated. d) Resulting image after green channel is divided by red channel. e) The binary image after a threshold correction. Positive reactions (originally blue) are white and negative reactions (originally purple) are black. Image processing was performed with Image J (ver. 1.49).

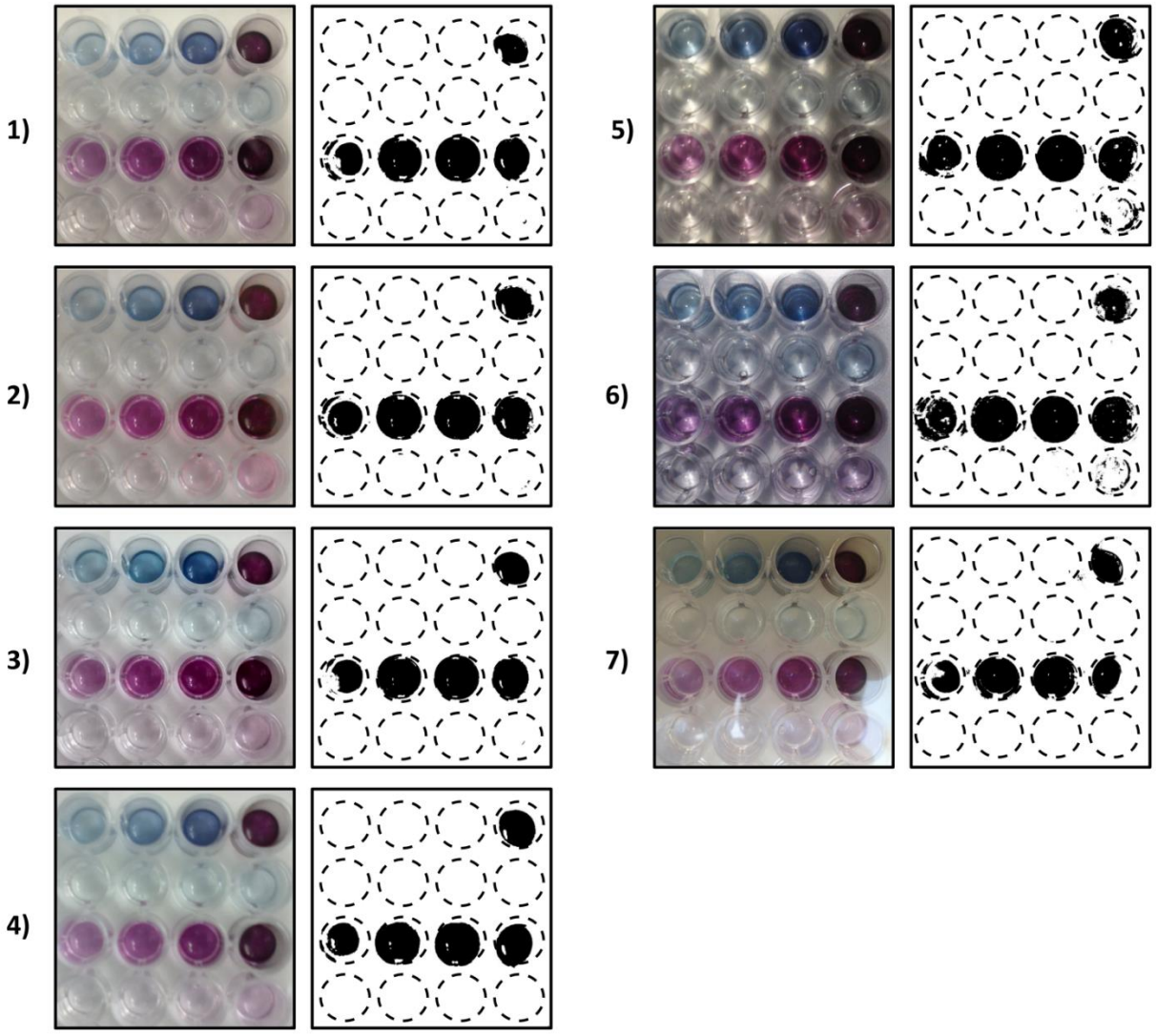

Figure S3.3 Original and G/R-processed images acquired with unmodified cell phone cameras. Original color images show negative (bottom two rows) and positive (top two rows) RT-LAMP reactions. From left to right, EBT concentration is increased in two-fold increments between 10.9 µM to .088mM (bottom row) and .175mM to 1.4mM (second row from the bottom). Positives contained HCV RNA and the same EBT concentration pattern was repeated. Negative wells are purple and positive wells are blue. Ratiometric G/R-processed images show the binary result in which the negative wells become black and the positive wells become white. (1–4) Images collected with four common cell phones under fluorescent light: (1) Apple iPhone 4S, (2) HTC inspire 4G, (3) Motorola Moto G and (4) Nokia 808 PureView. (5–7) Images collected with Apple iPhone 4S under

different light conditions: (5) incandescent light, (6) direct sunlight and (7) indirect sunlight. Image processing was performed with ImageJ (ver. 1.49).

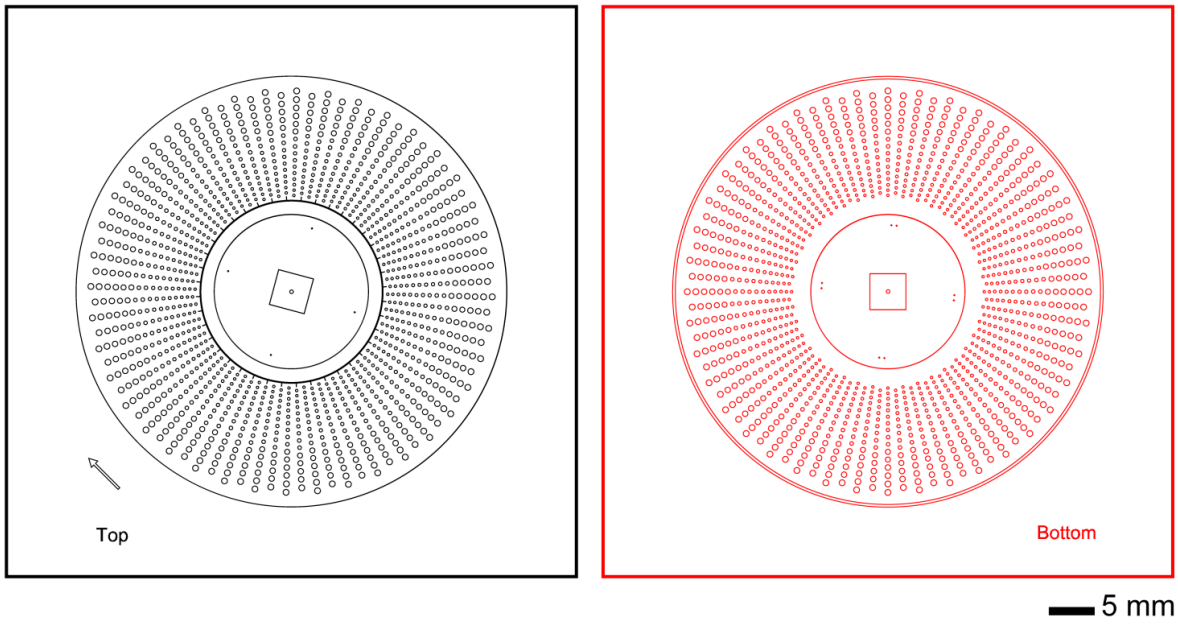

Figure S3.4 Schematic of the top (left) and bottom (right) plates of the multivolume rotational SlipChip device used in the one-step digital LAMP experiments before being assembled. The top plate shows the direction of the rotational 4.5° slip.

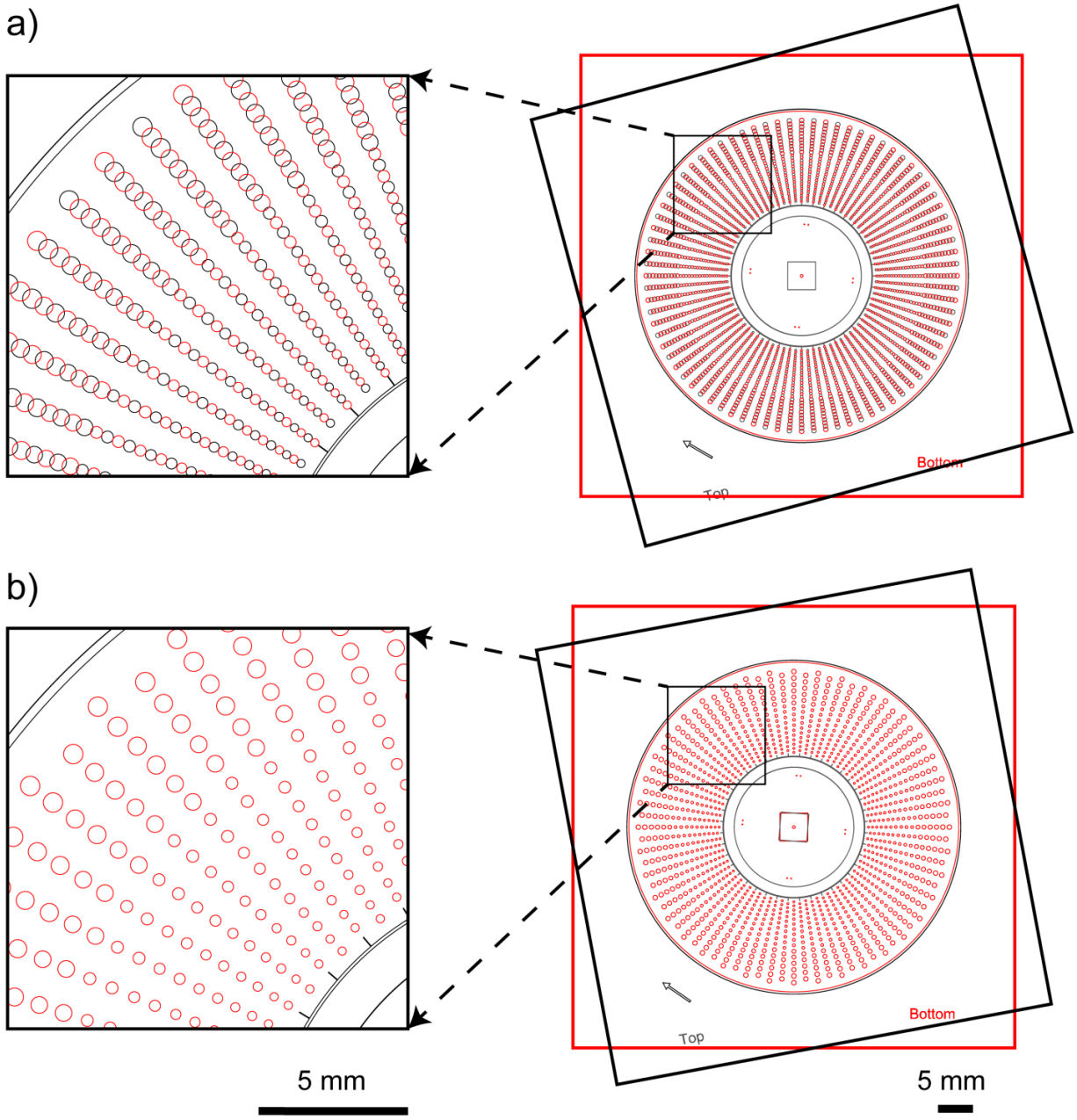

Figure S3.5 Schematic of the multivolume rotational SlipChip device used for one-step digital LAMP experiments after being assembled. Drawing shows the layout of top and bottom pieces of the entire device on the right and a zoomed-in region (black box) on the left. a) Relative position of the two pieces when they are aligned to allow loading of solution through the channel, and b) the

relative position of the two pieces when they are slipped (top slide rotated 4.5°) to separate droplets from one another and form compartments. Features shown are before isotropic glass etching.

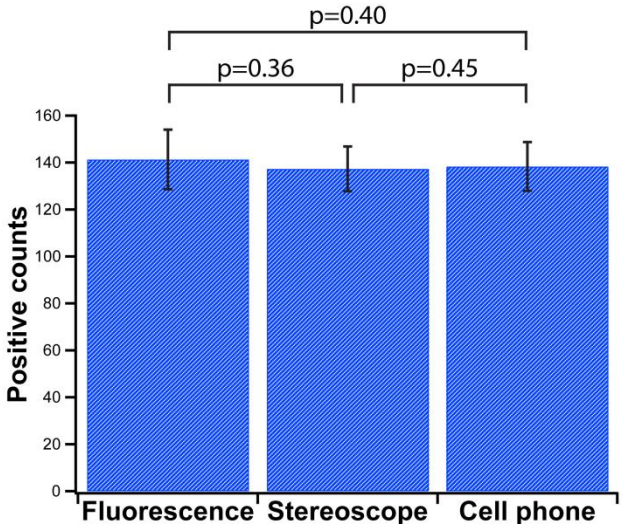

Figure S3.6 Positive counts obtained from single-molecule digital LAMP reactions performed with lambda DNA on a one-step SlipChip device imaged by a house-built real-time fluorescence microscope, a Leica MZ Fl III stereoscope, and an unmodified cell phone camera (Apple iPhone 4S) under fluorescent light. One-step visual readout was performed on SlipChip devices composed of 800 wells of 27 nL volumes. LAMP amplification mix contained 0.7 mM eriochrome black T dye solution, SYTO® 9 Stain and phage lambda DNA. Automated counting was performed by self-developed LabVIEW software for fluorescent images and freeware Fiji image processing for bright field G/R processed images. Data are mean positive counts and error bars are S.D. (N = 3). Student's t-tests were used for statistical comparisons, showing no significant differences among counts obtained by the three imaging methods (*P* values > 0.05).

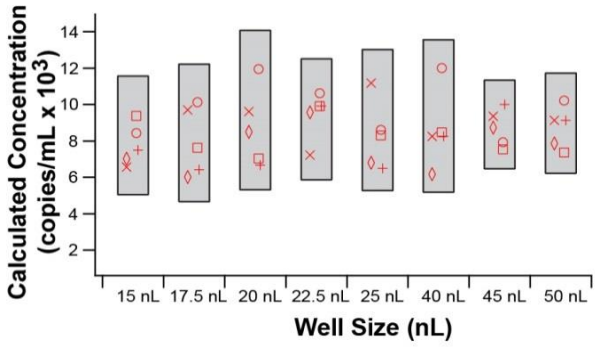

Figure S3.7 Five multivolume experiments were performed, and the concentration of each volume was calculated based on the methods of Kreutz *et al*.[1] Gray boxes denote the 95% confidence interval for the set of experiments at each volume. Concentrations calculated at each volume are consistent, and there is no bias based on the volume in which the reaction is performed.

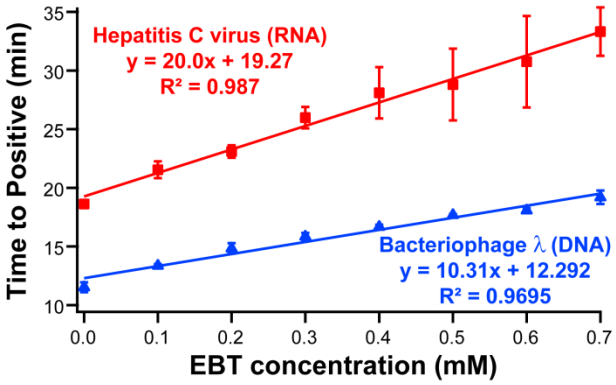

Figure S3.8 Performance of bulk LAMP reactions at increasing concentrations of the amplification indicator dye eriochrome black T (EBT). All reactions performed in 10 μL volumes with concentrations of EBT solution ranging from 0.0 to 0.7 mM, SYTO® 9 Stain and either 1,000 copies of HCV RNA (red) or 1,000 copies of phage lambda DNA (blue). All reactions were run in triplicate.

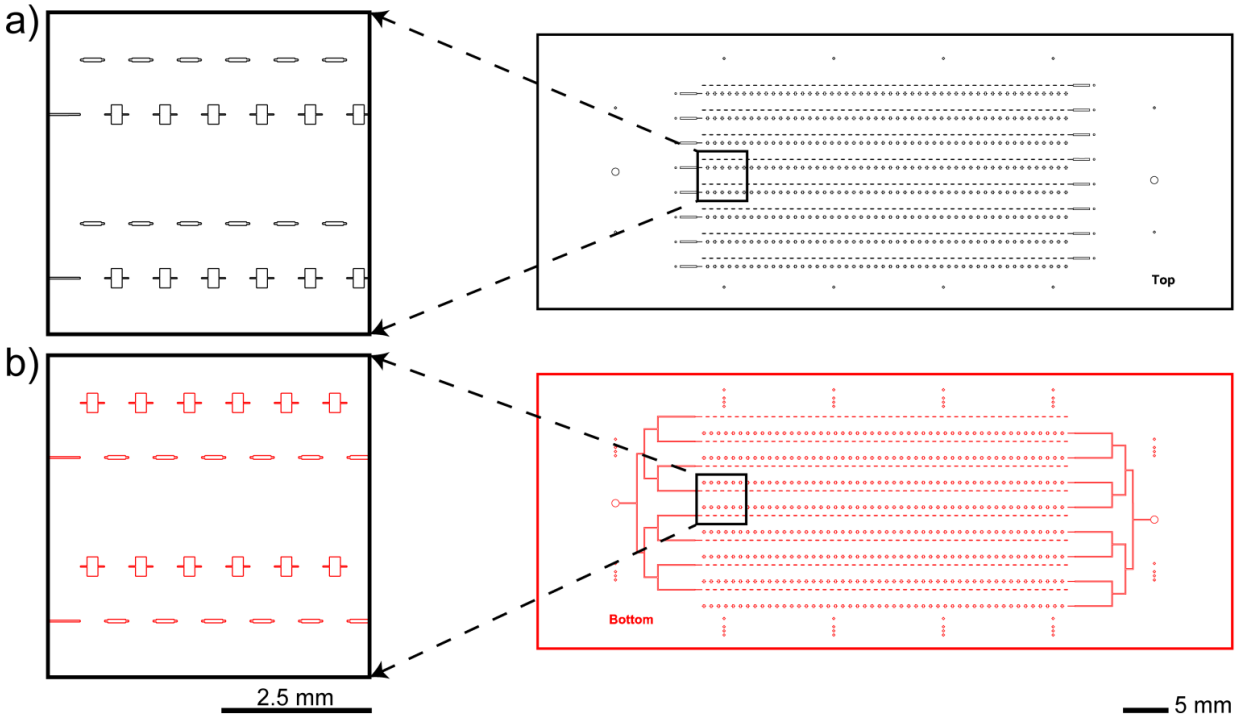

Figure S3.9 Schematic of the two-step SlipChip device before assembly. Drawings show the top (a) and bottom (b) device plates with a selected region (black box) magnified on the left to show locations of the 5 nL and 9.5 nL wells. Features are shown before isotropic glass etching. The design of the two-step SlipChip device was based on previously published SlipChip designs.[2]

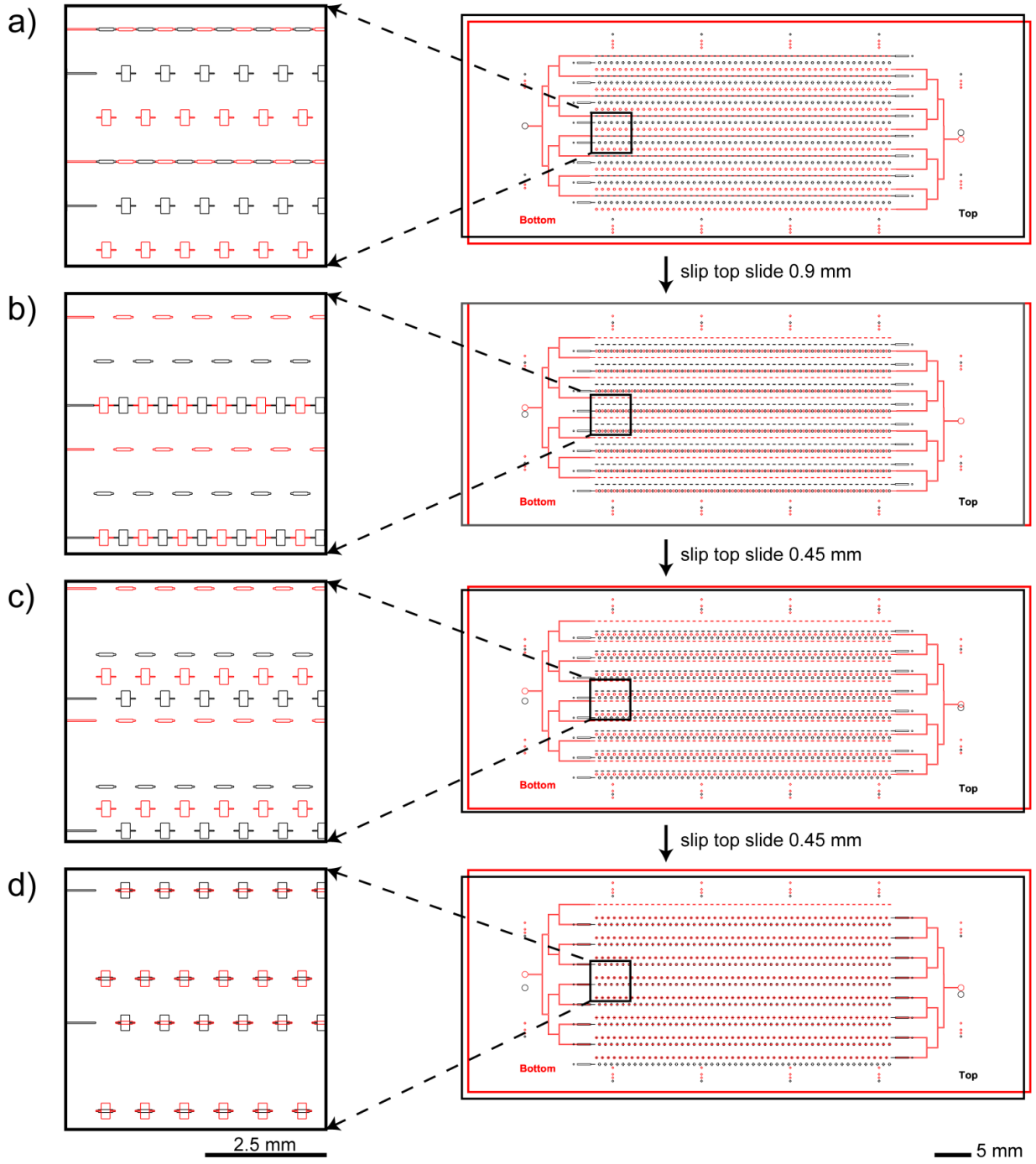

Figure S3.10 Schematic of the two-step SlipChip device after assembly and its operation. Drawings show the layout of the top and bottom plates on the right and a magnified region (black box) on the left. (a) Loading conformation for the first set of wells (5 nL each). (b) Loading conformation for the

second set of wells (9.5 nL each). (c) Incubation conformation. (d) Final mixing conformation ready for imaging with a cell phone camera. Features are shown before isotropic glass etching.

Table TS3.1 Sequence of primers used in RT-LAMP experiments for detection of hepatitis C RNA.[3]

Primer	sequence (5'-3')
F3	CCTCCCGGGAGAGCCATAG
FIP	TCCAAGAAAGGACCCIGTCTTTTTCTGCGGAACCGGTGAGTAC
LF	TTICCGGIAATTCCGGT
B3	GCACTCGCAAGCACCITATC
BIP	TTGGGCGTGCCCCCGCIAGATTTTTCAGTACCACAAGGCCITTCGCIACC
LB	CTGCTAGCCGAGTAGIGTTG

Table TS3.2 Sequence of primers used in LAMP experiments for detection of phage lambda DNA.[4]

primer	sequence (5'-3')
F3	GAATGCCCGTTCTGCGAG
FIP	CAGCATCCCTTTCGGCATACCAGGTGGCAAGGGTAATGAGG
LF	GGCGGCAGAGTCATAAAGCA
B3	TTCAGTTCCTGTGCGTCG
BIP	GGAGGTTGAAGAACTGCGGCAGTCGATGGCGTTCGTACTC
LB	GGCAGATCTCCAGCCAGGAACTA

Table TS3.3 Multivolume device designs for viral load quantification.

Volumetric step	Number of well volumes	Well volume range (nL)	Number of wells per device	LDL – ULQ (copies/mL)	DR (log)
2	6	5 – 160	2,700	500 – 1,000,000	3.3
2	6	5 – 160	2,700	50 – 1,000,000	4.3
5	3	5 – 125	1,350	500 – 1,000,000	3.3
5	3	5 – 125	1,350	50 – 1,000,000	4.3
25	2	5 – 125	900	500 – 1,000,000	3.3
25	2	5 – 125	940	50 – 1,000,000	4.3

The lower detection limit (LDL) is defined as the concentration which would have a 95% probability of generating at least one positive well. The upper limit of quantification (ULQ) is defined as the concentration where the probability of all wells being positive is 5%. DR: dynamic range. Calculations were performed according to the equations and algorithms found in *Kreutz JE, Munson T, Huynh T, Shen F, Du W, Ismagilov RF. "Theoretical design and analysis of multivolume digital assays with wide dynamic range validated experimentally with microfluidic digital PCR." Anal Chem. 2011 83(21):8158-68.*

a)

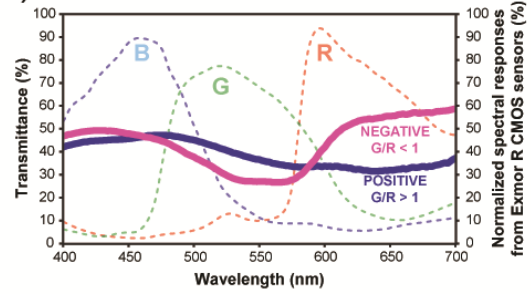

b)

Predicted ratiometric values and difference between positive and negative LAMP reactions in the presence of Eriochrome Black T indicator dye

Process	positive	negative	positive-negative (%)
Green/Red	1.06	0.87	0.19 (17.9)
Blue/Red	1.13	0.97	0.16 (14.2)
Green/Blue	0.94	0.90	0.04 (4.3)

c)

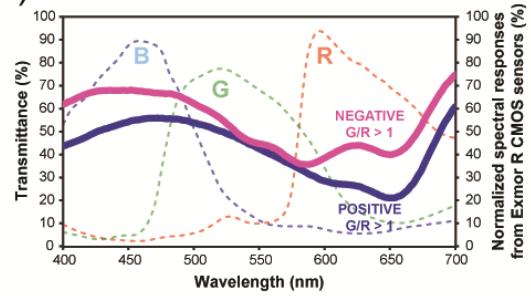

d)

Predicted ratiometric values and difference between positive and negative LAMP reactions in the presence of Hydroxynaphthol Blue indicator dye

Process	positive	negative	positive-negative (%)
Green/Red	1.17	1.06	0.11 (9.4)
Blue/Red	1.25	1.17	0.08 (6.4)
Green/Blue	0.94	0.90	0.04 (4.3)

e)

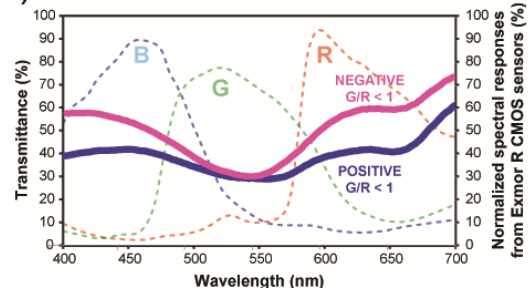

f)

Predicted ratiometric values and difference between positive and negative LAMP reactions in the presence of Calmagite indicator dye

Process	positive	negative	positive-negative (%)
Green/Red	0.92	0.86	0.06 (6.5)
Blue/Red	0.98	0.95	0.03 (3.1)
Green/Blue	0.94	0.91	0.03 (3.2)

Figure S3.11 (a, c and e) Measured spectral transmittance (%) in the range of visible light (400–700 nm) for positive (solid blue line) and negative (solid purple line) RT-LAMP reaction solutions, each containing 0.7 mM of eriochrome black T, hydroxynaphthol blue or calmagite as the amplification indicator dye. Dashed lines correspond to normalized spectral responses for red (R), green (G) and blue (B) channels of an Exmor R CMOS sensor, a common sensor in cell phone cameras. (b, d and f) Predicted ratiometric values for positive and negative LAMP amplification reactions processed for each ratiometric combination, Green/Red, Blue/Red and Green/Blue. Tables show absolute differences (positive – negative) and the relative difference (in %) between positive and negative ratiometric values are shown. All experiments were performed with HCV RNA as a template. Dye stock solutions were prepared as described in the Methods section "Preparation of EBT solution."

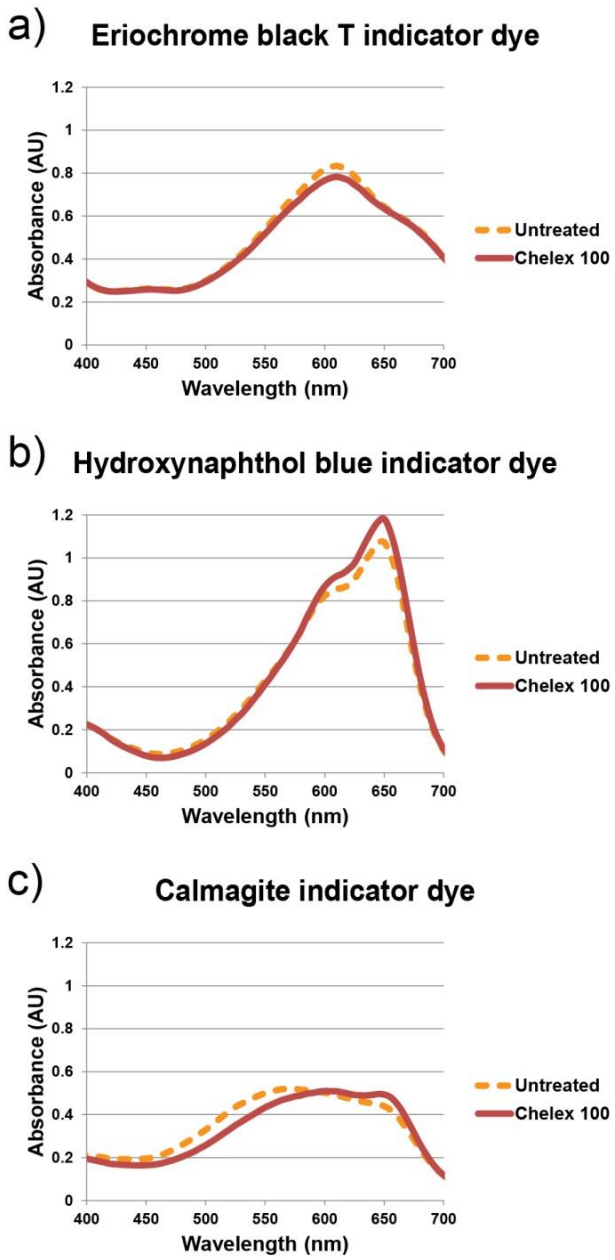

Figure S3.12 Comparison of the spectral absorbance (Absorbance Units) of untreated indicator dye stock solutions (dashed orange lines) and solutions treated with Chelex® 100 resin (solid red lines) for (a) eriochrome black T (EBT), (b) hydroxynaphthol blue (HNB) and (c) calmagite indicator dyes. The EBT, HNB and calmagite stock solutions were prepared by dissolving the dyes in 20 mM Tris-HCl buffer (pH 8.8) at 0.7 mM. The solutions were sonicated for 10 min and mixed on a rotator at

room temperature for 1 h. The solutions were split into two equal volumes for the comparison; one volume was treated with Chelex® 100 ion exchange resin (5% w/v).

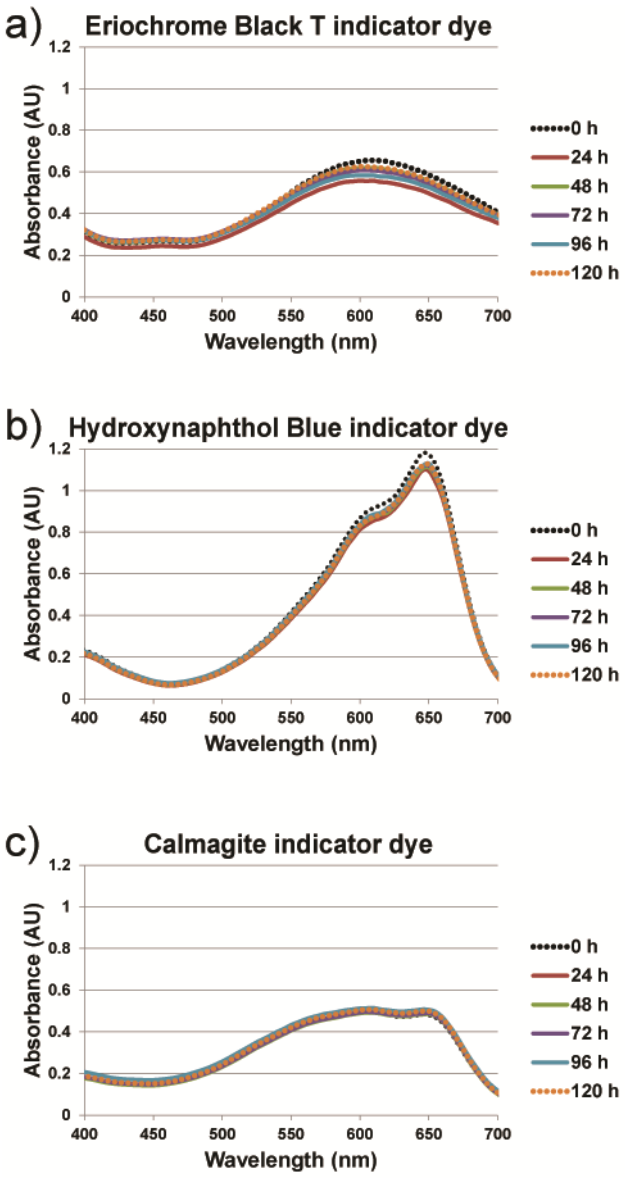

Figure S3.13 Storage stability of amplification indicator dyes by drying the stock solutions in the presence of stabilizer trehalose. Measured spectral absorbance (Absorbance Units) in the range of visible light (400–700 nm) for (a) eriochrome black T (EBT), (b) hydroxynaphthol blue (HNB) and (c) calmagite indicator dyes solutions. Time "0 h" is the spectral absorbance of the dye stock solution prior to drying in a desiccator under vacuum. The following time points correspond to the length of

time the dye stock solution was maintained in its dried state before being resuspended in distilled water. Full protocol is in Methods in the section “Storage stability of amplification indicator dyes by drying in the presence of stabilizer trehalose.”

Supplementary References

1. J. E. Kreutz, T. Munson, T. Huynh, F. Shen, W. B. Du, and R. F. Ismagilov, "Theoretical design and analysis of multivolume digital assays with wide dynamic range validated experimentally with microfluidic digital PCR," *Analytical Chemistry*, **2011**, 83, 8158-8168.
2. F. Shen, E. K. Davydova, W. B. Du, J. E. Kreutz, O. Piepenburg, and R. F. Ismagilov, "Digital isothermal quantification of nucleic acids via simultaneous chemical initiation of recombinase polymerase amplification reactions on SlipChip," *Analytical Chemistry*, **2011**, 83, 3533-3540.
3. B. Sun, J. Rodriguez-Manzano, D. A. Selck, E. Khorosheva, M. A. Karymov, and R. F. Ismagilov, "Measuring fate and rate of single-molecule competition of amplification and restriction digestion, and its use for rapid genotyping tested with hepatitis C viral RNA," *Angewandte Chemie-International Edition*, **2014**, 53, 8088-8092.
4. A. Gansen, A. M. Herrick, I. K. Dimov, L. P. Lee, and D. T. Chiu, "Digital LAMP in a sample self-digitization (SD) chip," *Lab on a Chip*, **2012**, 12, 2247-2254.

CHAPTER 4

Microfluidic SlipChip device for multistep multiplexed biochemistry on a nanoliter scale

Abstract

We have developed a multistep microfluidic device that expands the current SlipChip capabilities by enabling multiple steps of droplet merging and multiplexing. Harnessing the interfacial energy between carrier and sample phases, this manually operated device accurately meters nanoliter volumes of reagents and transfers them into on-device reaction wells. Judiciously shaped microfeatures and surface-energy traps merge droplets in a parallel fashion. Wells can be tuned for different volumetric capacities and reagent types, including for pre-spotted reagents that allow for unique identification of original well contents even after their contents are pooled. We demonstrate the functionality of the multistep SlipChip by performing RNA transcript barcoding on-device for synthetic spiked-in standards and for biologically derived samples. This technology is a good candidate for a wide range of biological applications that require multiplexing of multistep reactions in nanoliter volumes, including single-cell analyses.

Introduction

This paper explores a versatile microfluidic SlipChip that performs multistep biochemical reactions in a multiplexed format on a nanoliter scale. Combining reagents is a basic unit operation in chemistry, yet controlled multistep merging of nanoliter droplets has remained a challenge. To move the field of microfluidics forward and increase the adoption of miniaturized platforms, we need to expand the arsenal of methods for performing this operation. The ability to perform multistep biochemical reactions will be of particular benefit for many protocols and biological assays,[1] such as nucleic acid[2] and biomarker[3] detection/quantification, time-sensitive and autocatalytic[4] reactions, as well as particle synthesis.[5] Multistep reactions in very small volumes are also needed for low-input applications such as tissue-extracted rare-cell studies,[6] where controlled mixing of two or more reagents is often required to start/quench reactions or to dilute solutions. Specifically, temporal control over several sequential, parallelized reactions is important in complex biochemical procedures, such as singe-cell analyses.

Current solutions for merging of nanoliter droplets, such as integrated fluidic circuits and automated pipetting systems, require complex microfluidics and control systems (e.g. pumps, pneumatic valves, multilayer soft lithography, surface acoustic waves, microsolenoid dispensers, electrowetting-on-dielectric technology, *etc.*), especially when there are multiple steps.[5,7-13] Although droplet-encapsulation methods[14] provide virtually unlimited scalability to the number of compartments, and have progressed greatly in high-throughput detection,[15-17] washing,[18] and sorting,[19] they have limitations with respect to reagent additions to the originally encapsulated volumes, imaging, and reaction parallelization.

SlipChip[20] is an attractive platform on which to build multistep capabilities. In addition to offering the general, well-established benefits of a miniaturized platform (*e.g.*, small reagent volumes, high relative concentrations of analytes),[21-23] SlipChip devices give the user the capability to program a complex protocol of fluidic manipulations and to execute it by simply "slipping" the plates of the device among different conformations. SlipChip devices have been well characterized;[20,24-26] briefly, a SlipChip is composed of two glass plates with microfabricated features such as wells, channels, and ducts. The volumes and shapes of these features can be tuned by photolithography. The

fabricated plates are rendered hydrophobic and oleophilic with silane, and assembled with oil coating all features. Thus, when an aqueous solution is loaded into a SlipChip, it does not wet the surfaces (*i.e.*, a thin layer of oil remains between the aqueous phase and the glass surfaces). By slipping one plate with respect to the other plate (along *x* and/or *y* axes), numerous pre-programmed configurations can be accessed and transient well-channel networks can be used to create and merge droplets. Multistep SlipChip protocols involving serial dilutions have been demonstrated. [27,28] This work adds a capability to perform complete droplet transfer (previously droplets were split by slipping and retained in the wells) in addition to the option to retrieve samples after reaction without cross-contamination. SlipChips have also been demonstrated for multiplexing.[25,27,29]

Building on the SlipChip platform, we designed a device that accurately meters and manipulates nanoliter volumes of reagents and adds them to reaction wells in a multiplexed, parallel fashion. This multistep device facilitates complete droplet transfer between microwells by controlling the shape of the interface between two immiscible fluids[26,30] *via* judiciously selected geometries. The parallelization of the reactions is enabled by three features: (1) surface-energy traps[31-33] that immobilize an array of droplets while the next set of droplets is being merged with it, (2) differences in the depths (along *Z*-dimension) of the device's microfeatures that provide the driving force for the fluid transfer,[26] and (3) well shapes (in *XY*-plane) that prevent droplet break-up and guide droplets to merge. Importantly, the device contains a set of features into which the user can pre-spot reagents that can be used to uniquely identify the contents of any one well from any other well after they are pooled. So instead of offering on-device readout only as demonstrated previously,[8,27,28] this device is designed for the user to be able to extract the products of on-device reactions for further analysis. We demonstrate the utility of this multistep device to perform multiplexed reactions by performing a seven-step workflow: transcript barcoding for multiplexed cDNA sequencing library preparation for total RNA sequencing (RNAtag-Seq).[34]

Results

Sequential drop-in of reagents is driven by capillary (Laplace) pressure

To sequentially add ("drop-in") and mix multiple rounds of reagent droplets from carrier wells into mixing wells, we harnessed the driving force of capillary (Laplace) pressure by confining the interface between two immiscible fluids. One basic requirement for drop-in to work is that mixing wells must be deeper than carrier wells (Figure 4.1). A droplet's surface energy is proportional to its interfacial area, which is at a minimum when the droplet is spherical. Droplets are first loaded into shallow carrier wells (Figure 4.1A) with a micropipette. These carrier wells shape the interface of the droplets and have high surface energy. Once these flattened droplets are slipped into the more spacious geometric region (mixing wells), they become more spherical (Figure 4.1C), thereby attaining lower surface energy. Droplets are thus energetically incentivized to fully transfer to and remain inside the larger mixing wells as the plates are slipped back into the original conformation (Figure 4.1D). Specifically, the driving force for this transfer arises from the imbalance in capillary pressures created by non-equal feature dimensions in the front and back of the droplet, as we have described previously.[26]

$$\Delta P_{\text{cap,back}} - \Delta P_{\text{cap,front}} = 2\gamma\cos\theta_{\text{R}}\left(\frac{1}{h_{\text{W}}}+\frac{1}{w}\right) - 2\gamma\cos\theta_{\text{A}}\left(\frac{1}{h_{\text{C}}}+\frac{1}{w}\right) \quad \text{(Eq. 4.1)}$$

$\Delta P_{\text{cap,back}}$ = capillary pressure at the back of the droplet [Pa]

$\Delta P_{\text{cap,front}}$ = capillary pressure at the front of the droplet [Pa]

γ = liquid-liquid interfacial tension [N/m]

θ_{R} = receding contact angle [rad]

θ_{A} = advancing contact angle [rad]

h_{W} = height of the mixing wells [m]

h_{C} = height of the carrier wells [m]

w = width dimension, assumed constant for both types of wells [m]

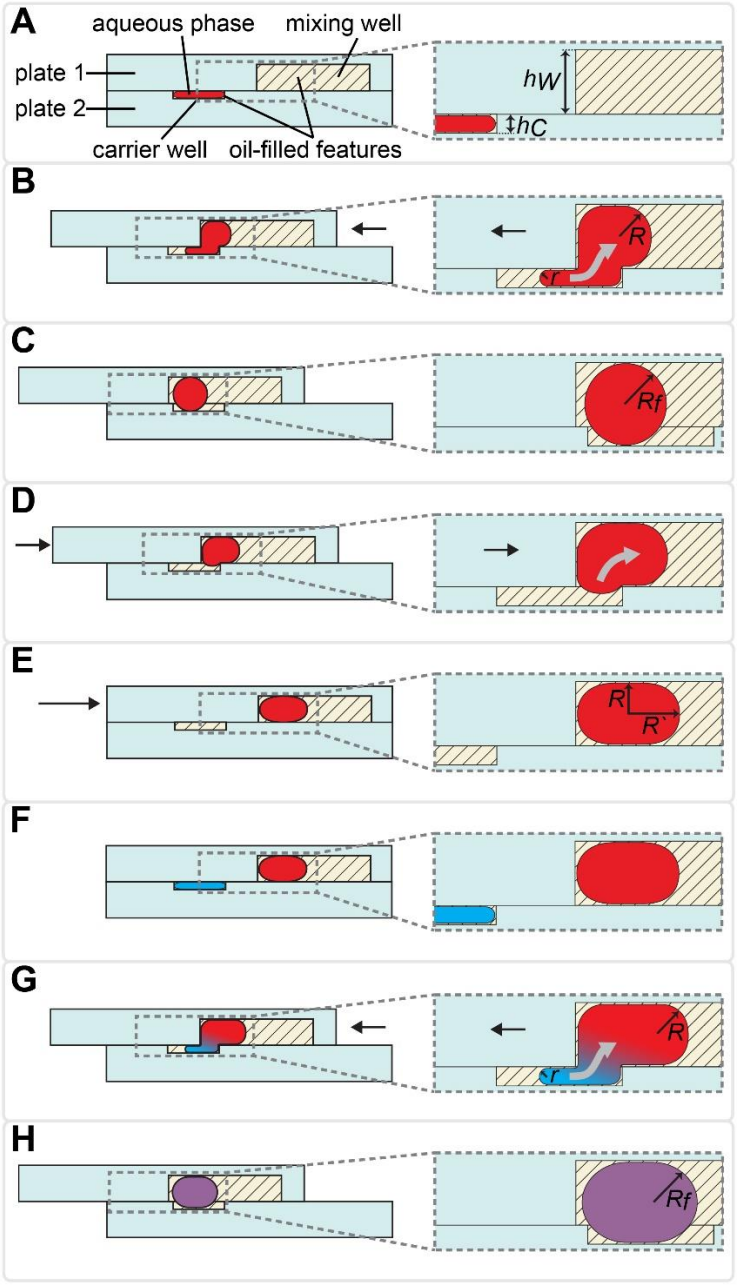

Figure 4.1 Diagram of the multistep SlipChip device illustrating the drop-in approach using back-and-forth slipping in which the interfacial energy between two immiscible phases drives fluid transfer. (A) The carrier wells are loaded with the first solution through connecting channels, which are located in a different plane (not shown). In the carrier wells, the radius of curvature of the interface in the plane shown is restricted by well height (h_C). Mixing wells are deeper than carrier

wells ($h_W > h_C$) and are less restricting. (B) As plate 1 is slipped relative to plate 2, the droplet is transferred to the mixing well and is free to assume higher radius of curvature. The oil from the mixing well replaces the droplet in the carrier well. (C) Slipping is complete and the first solution is dropped-in, it is now contained in the volume created by aligned carrier and mixing wells. (D) Plate 1 is slipped back into loading position. The droplet remains in the deeper mixing well where it can assume a more energetically favorable conformation. (E) Slipping is complete and the droplet remains in the mixing well. (F) Loading carrier wells with the second solution. (G) Slipping plate 1 relative to plate 2 drops in the second solution into mixing wells, where it merges with the droplet of the first solution. (H) The slipping is complete and both solutions are mixed and contained in the volume that the aligned carrier and mixing wells create.

This drop-in approach may be performed using the same carrier well multiple times (as described in Figure 4.1), or by using different carrier wells, as we describe below. Using the same carrier well is convenient when the same volume needs to be loaded for each reagent. To load different volumes of reagents, additional carrier wells of different volumes can be added to plate 2 and loaded/slipped sequentially. Note that the actual volume and the viscosities of both fluid phases are not a part of the above equation for the driving force. However, they are important factors in the viscous drag force that will be slowing the fluid transfer and should be carefully considered by the chip designer, since the resulting flowrate may become unacceptably slow for some applications. For reference, in rectangular channels *i* ($h_i < w$) that are connected in series, the total flow resistance can be calculated by equation 4.2:[26,35]

$$P_{\text{drag}}/Q = \sum_i \frac{\pi^4 \mu_i L_i}{8 h_i^3 w_i \left(1 - \frac{2h_i}{\pi w_i} \tanh\left(\frac{\pi w_i}{2h_i}\right)\right)} \quad \text{(Eq. 4.2)}$$

P_{drag}/Q = viscous drag force [N]

μ_i = viscosity of fluid *i* [Pa·s]

L_i = length of channel *i* [m]

h_i = height of channel *i* [m]

w_i = width of channel i [m].

Because the aqueous phase does not come into direct contact with surfaces in this SlipChip design, the loss of material to adsorption or sticking is minimized, which is important for applications where there is low input of materials. One such application is handling nucleic acids originating from small numbers of, or even single, cells.

We used the drop-in approach from Figure 4.1 to design a device (Figure S4.1) to perform multistep transcript barcoding for multiplexed RNA sequencing library preparation, described in more detail below. Briefly, we wanted to test whether we could use the multistep device to facilitate sensitive recovery of barcoded RNA transcripts. As the starting point for the workflow, we selected and modified the published RNAtag-Seq method[34] for total RNA sequencing. To block/dilute the undesired components of preceding reactions (*e.g.*, to avoid inhibition in an additive protocol), we sequentially added reagents in a range of volumes that changed the composition of the reaction buffer between steps. Because this biochemical workflow required carrier wells of different volumes, we chose to use a sequential drop-in approach rather than the back-and-forth approach described in Figure 4.1.

In the multistep SlipChip device, the user first loads the sample (Figure 4.2A-[4 and 5]). When the device is slipped (Figure 4.2B), the sample is compartmentalized and transferred from the carrier wells (Figure 4.2A-[5]) into the mixing wells (Figure 4.2A-[2]). Note that the fluid remaining in the connecting channels (Figure 4.2A-[4]) does not get transferred into mixing wells, which means that these connecting channels can be of arbitrary length (the spacing of carrier wells will have to match this length). For the device shown, we chose a length of 0.75 mm, which was convenient for manual slipping, while keeping the total footprint of the device low (Figure S4.1). The mixing wells (Figure 4.2A-[2]) contain surface-energy traps (Figure 4.2A-[3]) that help position the droplets for downstream reagent additions (these traps are explained in detail in the next section). The device is designed so that when it is slipped into the drop-in position for one carrier well, the device is also configured into the loading position for the next carrier well. For example, Figure 4.2B represents conformation for both dropping-in the sample from the first set of carrier wells (Figure 4.2A-[5]), and for loading of the first reagent into the second set of carrier wells (Figure 4.2A-[6]). The next

three mixes of reagents are loaded, compartmentalized, and transferred into the mixing well in the same fashion (Figure 4.2C-F) with the next three arrays of carrier wells (Figure 4.2A-[6-8]). Note that wells of type 9 (Figure 4.2A-[9]) each contain a different dry reagent spotted on the surface and therefore do not need to be loaded through the connecting channels (Figure 4.2A-[4]). The wells are given an appropriate shape to avoid contact with these channels during slipping (as shown in the configuration Figure 4.2E), and are made large enough for the user to be able to spot either manually or robotically. Once the pre-dried reagents are dissolved in the contents of the mixing wells, the next two reagent additions (Figure 4.2F-H) are performed using the same drop-in principle as in Figure 4.2A-E. Although there is not a strict rule on the shape of the carrier wells in the *XY*-plane, we observed that making them wider in the middle streamlines the drop-in process by "scooping" the fluid being carried inside the larger mixing wells towards the droplet anchored by the surface-energy trap (Figure 4.2A-[3]), especially in the early steps of the protocol, when the volumes in the mixing wells are still small. Thus, we made the wells of types 10 and 11 (Figure 4.2A-[10 and 11]) oval, whereas we made carrier wells of types 5–8 quadrilateral (Figure 4.2A-[5–8]). Wells of type 11 (Figure 4.2A-11) serve a dual purpose: they are carrier wells and they form a channel that connects the samples for pooling and extraction of the final products off-device (Figure 4.2I). To speed up this pooling step and to maximize sample recovery, the wells of type 11 (Figure 4.2A-[11]) were etched to the same depth as the mixing wells to reduce the flow resistance.

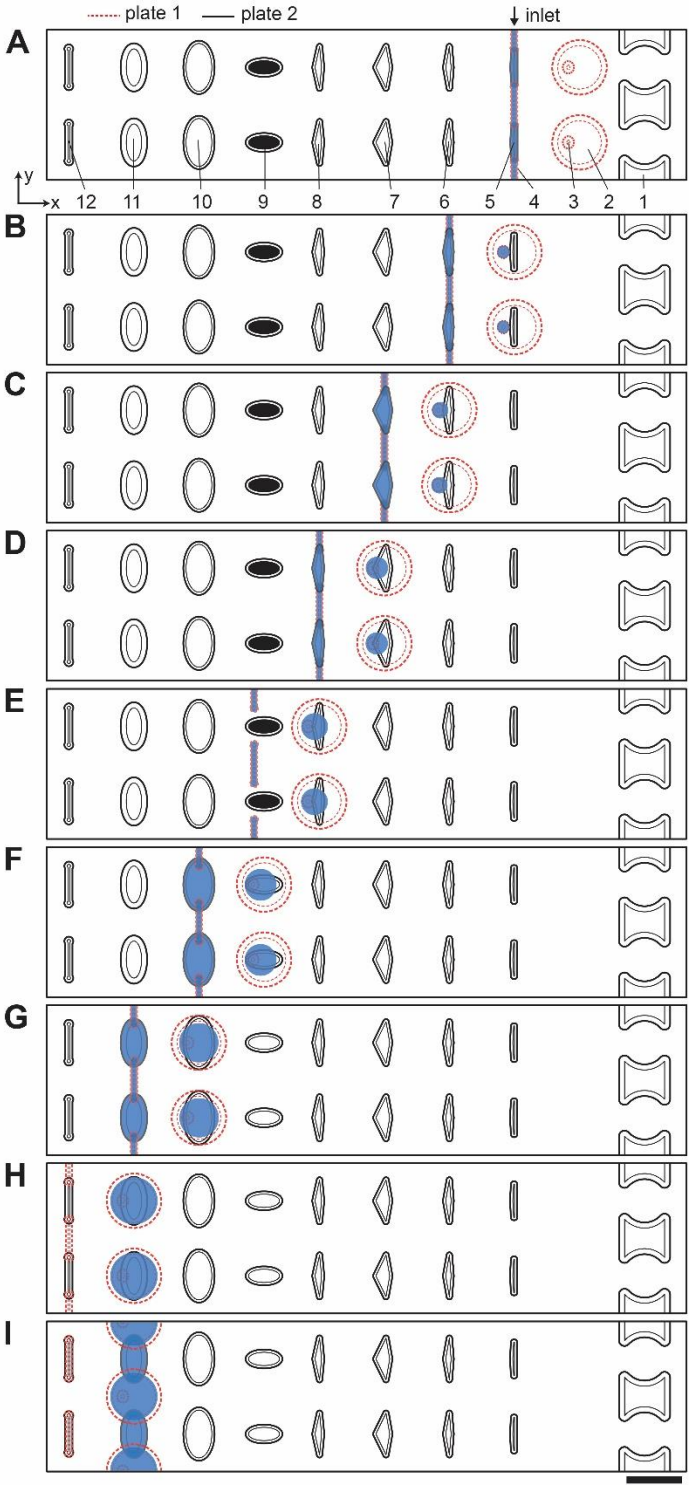

Figure 4.2 Top-down view of a two-row section of the multistep SlipChip device. (A) The two plates of the multistep device are assembled and aligned. Features and their corresponding depths:

[1] evacuation channels (100 μm); [2] mixing wells (100 μm); [3] surface-energy traps at the bottom of mixing wells (70 μm), mixing wells have a capacity of 71 nL together with the surface-energy traps; [4] connecting channels (40 μm); [5] carrier wells, 3 nL (50 μm); [6] lysis solution wells, 5 nL (50 μm); [7] RNA 3′-end repair solution wells, 7.4 nL (50 μm); [8] denaturing agent loading wells, 5.4 nL (50 μm); [9] barcode wells (50 μm); [10] ligation mix wells, 20 nL (50 μm); [11] crowding agent wells, 28.6 nL (100 μm); [12] channels for optional clearing of the connecting channels shown in feature [4]. First set of wells (type [5]) is shown being loaded through the inlet. Inlet and outlet holes for loading/unloading are drilled in plate 1 (Figure S4.1). (B) A sample drop-in into mixing wells and subsequent loading of the lysis solution. (C) Drop-in of lysis solution into the mixing wells and heat-treating the device to lyse cells and fragment RNA. Loading of the RNA 3′-end repair solution occurs in the same conformation. (D) Drop-in of 3′-end repair solution and loading of the denaturing agent. (E) Drop-in of denaturing agent. (F) Addition of the pre-spotted barcodes and loading of the ligase solution. (G) Drop-in of the ligase solution and loading of the crowding agent solution. (H) Drop-in of the crowding agent. Optionally, the loading channels can be drained and reloaded with carrier fluid in this conformation. (I) Plate 1 is shifted up to form a channel out of overlapping mixing wells and crowding agent wells. Using this newly formed channel, the user can pool and extract the contents of the wells with a pipette. Scale bar: 1 mm.

High viscosity continuous fluids have been reported to minimize the thinning and rupture of the wetting layer (which can lead to aqueous phase sticking) in SlipChip devices[26] and have been shown to speed up mixing after coalescence of dispersed-phase droplets.[36,37] We also observed that lower viscosity oils may wash away the pre-spotted reagents during device assembly as the extra oil is pushed out when the device plates are forced together (due to higher Reynolds number). Therefore, we chose to use 50 mPa*s silicone oil with 0.01 mg/mL Span-80 for continuous phase. This fluid has been previously tested with dichlorodimethyl-silanized glass devices.[26] A more viscous carrier fluid was undesirable because the flow resistance becomes too high during oil draining, and high viscosities have been demonstrated to slow droplet coalescence.[36,37]

Device designs that enable drop-in

We next determined which device dimensions would enable drop-in of droplets in parallel. Some applications, especially those involving biology or time-sensitive reactions, require parallelized reagent addition in a single multiplexed experiment. In the case of RNAtag-Seq with live cells,[34] one such example is the addition of the lysis buffer to all device wells, immediately before heating up the device to 72 °C for actual lysis (Figure 4.2C). If this addition is performed unevenly across the device, the non-uniform exposure of the cells to non-ionic detergent and EDTA (without heat-killing them) could affect transcription. Another example is adding ligase mixture right after the RNA denaturation step (Figure 4.2F). Denaturation is performed at 65 °C and the device needs to be immediately cooled on ice. The ligase mixture should be added while the device is still cold, so the 3′ and 5′ ends of the nucleic acids do not recover their secondary structures before they are stabilized by the ligase.

We selected a combination of 50 μm and 100 μm well depths to test drop-in. These depths produced convenient dimensions and the nanoliter-scale volumes desired for our miniaturized reactions. Even though the densities of our continuous and dispersed phases are slightly different (0.96 g cm^{-3} and 1.0 g cm^{-3}, respectively), capillary forces dominate over gravity at these dimensions,[38] and drop-in works regardless of the relative orientation of plates 1 and 2. Our goal was parallel merging across the device, and although we saw successful droplet transfer with these dimensions, merging did not take place in all wells in parallel. Because the droplets are much lower in volume than the volume capacity of the mixing wells, the droplets to be merged may not always be in contact inside the mixing wells. Merging across all wells can be achieved by additional slipping of plates, however we wanted a fast drop-in with a narrow distribution of merging times.

To accelerate drop-in and achieve uniform merging, we integrated two features that control the droplet position during slipping and inside the mixing wells. To localize the droplets inside the mixing wells, we equipped these wells with surface-energy traps (Figure 4.2A-[3]).[31-33] These traps are auxiliary wells that provide increased dimensions that allow lower surface-energy conformations of the droplets, thus anchoring them. We tested several depths and locations of the traps. We made the traps 70 μm at the bottom of the 100 μm mixing wells because an initial droplet of 3 nL will have

a diameter of ~180 μm^3 if allowed to assume a spherical shape. We also observed that placing the trap closer to the mixing well drop-in side enhanced merging (Figure 4.2A-[3]). Importantly, with the surface-energy traps, the droplets are in a regularly spaced array (Figure 4.3), which allows us to automate imaging.

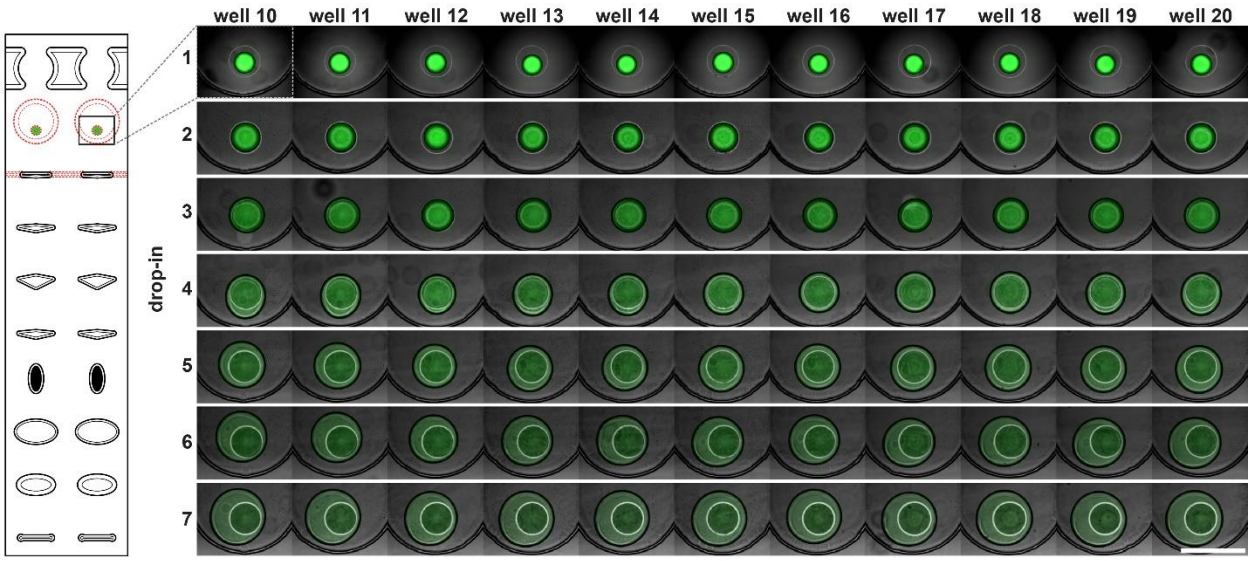

Figure 4.3 A subset of the multistep SlipChip device (wells 10–20) showing overlaid fluorescence and bright-field images after each of seven drop-in and merging events of 3 nL 50 μM Alexa Fluor 488 droplets. Scale bar: 500 μm.

Occasionally, a carrier well may not be loaded to capacity; in such cases, it is preferable for the well to contain a single volume (instead of multiple unmerged droplets) to facilitate further merging. To minimize the chance of droplet breakup during slipping, we made the carrier wells wider in the middle (Figure 4.2A-[5–8]). This way, smaller droplets are scooped toward the middle of the carrier wells during slipping and are aligned with the surface-energy traps of the mixing wells. Using microscopy, we confirmed that the multistep drop-in worked—each device slip transferred a new droplet from carrier well into each mixing well (Figure 4.3).

Additional device features

To enhance volumetric metering, we introduced a slight difference in depth between the connecting channels (Figure 4.2A-[4]) and carrier wells (Figure 4.2A-[5]). In loading conformation, the fluidic path is made of carrier wells in one plate and connecting channels in the opposite plate, in an alternating sequence. When an aqueous sample is loaded, it fills both the carrier wells and the connecting channels. Only the volumes filling the carrier wells will be transferred into the mixing wells. To ensure carrier wells are fully filled, we made the connecting channels shallower than the carrier wells (40 μm vs. 50 μm). Driven by capillary pressure (the same principle that enables the drop-in approach), the non-wetting aqueous phase will preferentially occupy the deeper carrier wells (Figure 4.1). This driving force is positively correlated with the difference in depth between the two features and can be estimated by using equation 4.1.[26] However, the flow resistance is inversely proportional to the cube of channel height equation 4.2,[26,35] and we observed that making the connecting channels less than 40 μm resulted in prohibitively high resistance to flow with the oil viscosity that we used (50 mPa s).

To test the ability of these geometries to yield reproducible drop-in and merging, we made a device according to the specifications in Figure 4.2, and used it to merge arrays of 50 3 nL droplets seven times using a back-and-forth slipping motion (moving between the conformations seen in Figure 4.2A and B). We observed successful droplet merging, which resulted in regular arrays of droplets after each addition (Figure 4.3).

We next added the ability to unload and reload samples during a single experiment. In addition to the obvious need for extracting the mixing-well contents from the device at the end of the procedure, we wanted to be able to restart an experiment without having to re-assemble and re-spot the device. For example, applications where samples are loaded before imaging with only a crude estimate of concentration (e.g. cell cultures), the user may unknowingly over- or under-load the device. In this case, it would be advantageous to be able to image and re-use the device without proceeding with the entire experiment. Evacuation channels (Figure 4.2A-[1]) provide the user the option to flush the contents of all mixing wells at any step before addition of the barcoded adaptors into the mixing wells (Figure 4.2F). By slipping device plate 1 in the opposite direction from the carrier wells of

plate 2, the mixing wells can be aligned with the evacuation channels to form a continuous channel (Figure S4.2C). In this conformation, the mixing wells can be emptied out with a pipette and re-filled with oil.

Next, we tested the reproducibility of volumetric metering in the device to confirm there was no spatial bias during loading. Deviations in the volumes delivered to mixing wells are due to errors in the loading of the carrier wells. To assess this variability, we loaded the device with 50 μM Alexa Fluor 488 (#A33077; Thermo Fisher) solution and slipped the carrier wells away from the connecting channels without dropping the contents into the mixing wells. We imaged these droplets using confocal microscopy and used the *Z*-stacks to calculate the droplet volumes (Figure S4.3). Using two different well sizes, we confirmed reproducible loading, both among wells within a single device, and among replicate trials (Figure 4.4). The coefficients of variation were of similar values for both well types: 0.093 for type 5 (Figure 4.4A) and 0.077 for type 7 (Figure 4.4B).

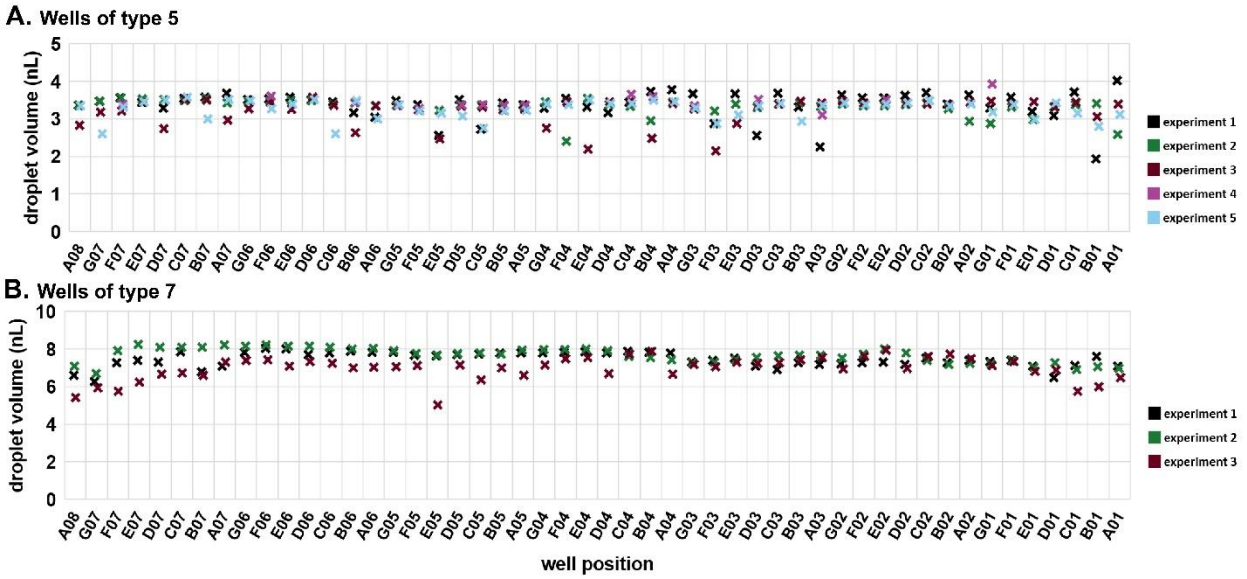

Figure 4.4 Reproducibility and spatial distribution of volume metering by carrier wells in the multistep SlipChip. (A) Wells of type 5, measured volumes of 3.30 ± 0.31 nL (mean ± S.D.); (B) wells of type 7 measured volumes of 7.36 ± 0.57 nL (mean ± S.D.).

Demonstration of the multistep device using RNA barcoding for RNA-Seq

To demonstrate the functionality of this device in performing complex biochemistry protocols, we chose to use it for RNA barcoding for multiplexed RNA sequencing (RNA-Seq). RNA-Seq is becoming an increasingly popular technology for transcriptomic studies, and any improvement in the sensitivity, accuracy and applicability for new types of samples would be of great benefit to the field. The published RNAtag-Seq method allows barcoding through direct ligation of RNA adaptors to fragmented and repaired total RNA. It is a strand-specific and full-length transcript-detection method that may be applied to any type of RNA, including RNA of prokaryotic and eukaryotic origins. We modified the barcoding protocol from the published RNAtag-Seq method to perform it in an additive fashion (as described in Supplementary Information). We specifically selected an extraction method that works for single eukaryotic cells and for Gram-negative bacteria[39] and incorporated this method into an additive biochemical protocol that provides compatible conditions for barcoding by ligation downstream.

The protocol consists of four sequential biochemical reactions: (i) template RNA fragmentation on-device under RNA extraction conditions; (ii) template RNA fragment ends repair; (iii) barcoded RNA adaptors & template RNA fragments denaturation; and (iv) ligating barcoded RNA adaptors to template RNA in every device well. These reactions were performed in a 7-step device workflow (Figure 4.5), starting from loading the RNA (Figure 4.5-2) and ending by pooling the barcoded transcripts from the device (Figure 4.5-10). As a result, we were able to generate and pool multiple barcoded intermediates for the subsequent RNA-Seq libraries preparations in a single device workflow.

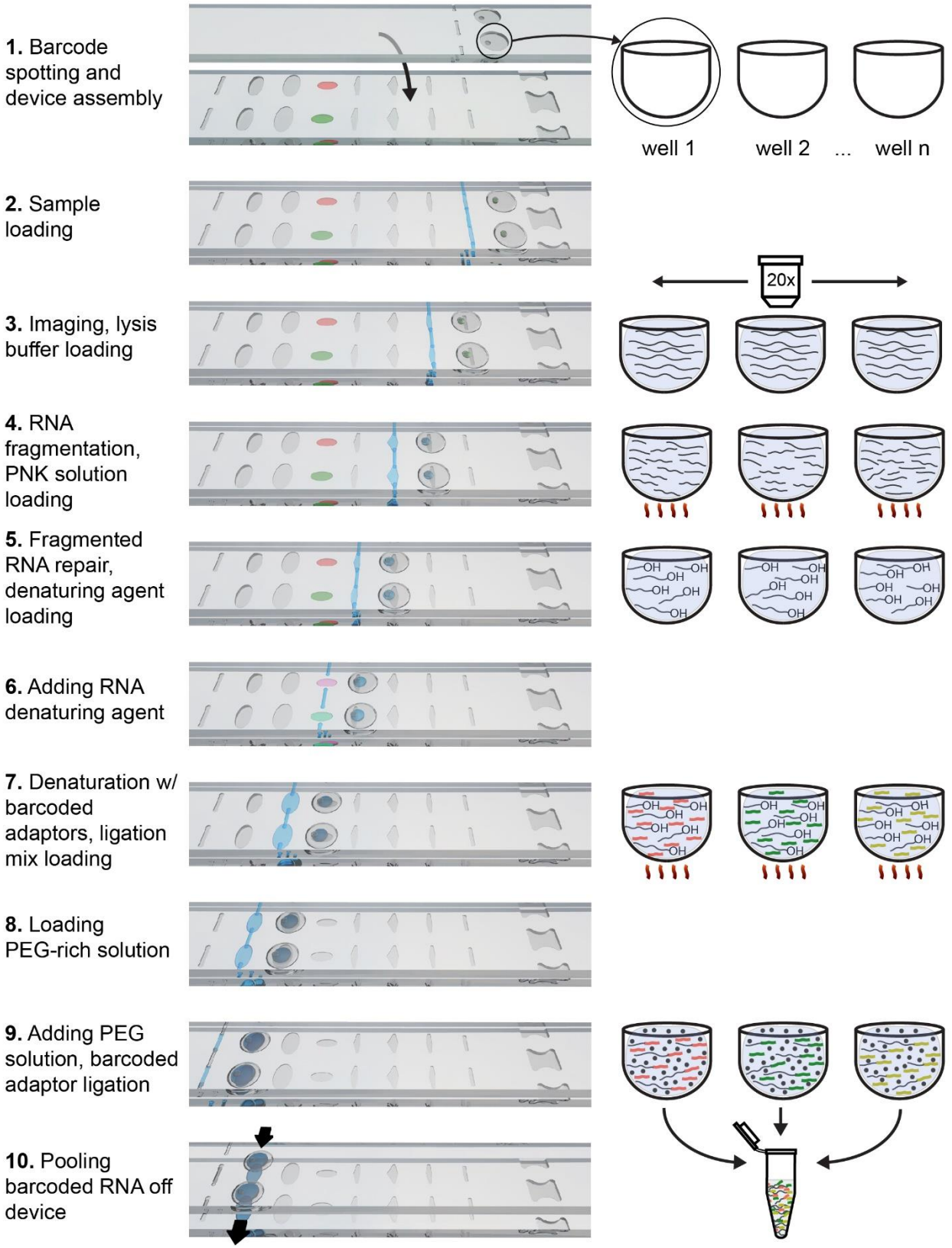
1. Barcode spotting and device assembly
well 1
well 2
...
well n
2. Sample loading
20x
3. Imaging, lysis buffer loading
4. RNA fragmentation, PNK solution loading
5. Fragmented RNA repair, denaturing agent loading
6. Adding RNA denaturing agent
7. Denaturation w/ barcoded adaptors, ligation mix loading
8. Loading PEG-rich solution
9. Adding PEG solution, barcoded adaptor ligation
10. Pooling barcoded RNA off device

Figure 4.5 Three-dimensional rendering of a two-well row section of the multistep SlipChip and a schematic illustrating the fragment barcoding process. Black lines represent RNA, and orange/green/yellow fragments represent barcodes. PEG crowding agent is represented by black dots.

Briefly, the barcoded RNA adaptors are spotted on plate 2 of the device and dried in the presence of trehalose before device assembly with silicone oil (Figure 4.2A-[9] and 4.5-1). Next, the sample containing RNA of interest is loaded into the device (Figure 4.2A and B and 4.5-2 and 3) through the drilled holes with a pipette and slipping the plates along x-axis. RNA can be loaded in Tris-EDTA buffer, water, PBS, or cell culture media. We then add a lysis buffer that contains EDTA and non-ionic detergents to mimic conditions of live cell lysis[39] and fragment RNA by heat (2 min at 72 °C, followed by an optional 3 min at 91 °C) (Figure 4.2B and C and 4.5-3 and 4). Next, T4 polynucleotide kinase (T4 PNK) is combined with the reaction mixture (Figure 4.2C and D and 4.5-4 and 5), it is added in the buffer that provides the optimal salts concentration in resulting reaction volume. T4 PNK removes occasional phosphates from the 3′ end of the RNA fragments. After the repair reaction, DMSO is added as an RNA denaturing agent (Figure 4.2D and E and 4.5-5 and 6), and the pre-spotted barcodes are combined with the repaired RNA fragments in the mixing well (Figure 4.2F and 4.5-7). Heating the device to 65 °C denatures RNA and inactivates T4 PNK. The last two steps are adding the T4 RNA Ligase (Figure 4.2F and G and 4.5-7 and 8) and a crowding agent solution (Figure 4.2G and H and 4.5-8 and 9). After allowing the ligation reaction to take place overnight, the contents of all mixing wells may be pooled off-device by slipping the plates along the y-axis and connecting the mixing wells (Figure 4.2A-[2]) and crowding agent wells (Figure 4.2A-[11]) to form a continuous channel for sample pooling (Figure 4.2I and 4.5-10). The contents of the device can now be extracted through drilled holes with a pipette. The rest of the cDNA library preparation takes place in a single tube, in a protocol similar to the published bulk RNAtaq-Seq method (see Supplementary Information).[34]

To test the accuracy and sensitivity of this workflow in our device, we used the device to barcode a dilution of External RNA Controls Consortium (ERCC) transcript spike-in kit, a standard tool used

in benchmarking of RNA-Seq methods (Thermo Fisher, Waltham, MA). After preparing and sequencing the cDNA library to approximately 0.6 million paired-end reads per barcode, we used published metrics[40] to evaluate the sensitivity (detection limit) (Figure 4.6A) and accuracy (Figure 4.6B) of our transcript quantification. We compare it to the published Drop-Seq method, which was sequenced to 2 million reads per barcode.[41] Our observed sensitivity and accuracy are on par with or outperform other published methods (Figure 4.6A and B).[40,42] The detection limit was 21 copies (the input level with detection probability >0.5), which is a competitive result at this sequencing depth, and is comparable to the performance of other methods (Figure 4.6A).[40,42] We believe this number can be brought even lower by increasing sequencing depth because in a comparison of RNA-Seq methods, sensitivity was more responsive than accuracy to sequencing depth.[40]

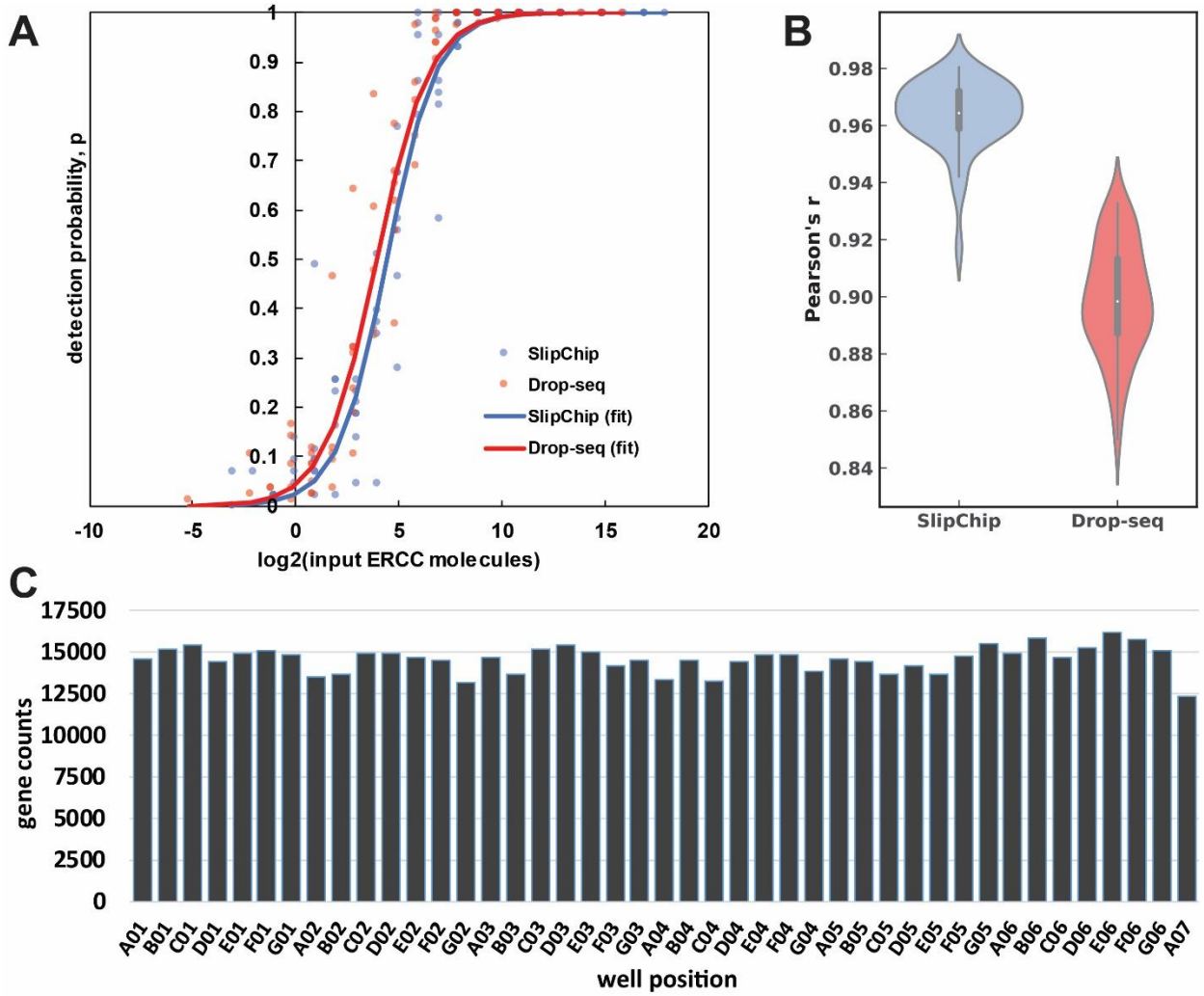

Figure 4.6 An overview of device-performance metrics. (A) To evaluate sensitivity, the ERCC transcript detection data was used to estimate binomial parameter p (detection probability) for various levels of input ERCC molecules. Logistic regression model was used to obtain a sigmoidal fit equation 4.3. Based on these regressions, the multistep device required 21 molecules for 50% probability of detection, whereas the Drop-seq method required 15.[41] (B) Distribution of Pearson correlation coefficient values (accuracy of quantification) between the detected expression units (TPM) of ERCC molecules and their input levels across the barcodes in our device and Drop-seq data set. The center of the box plot represents the median, the thick gray line represents the interquartile range, and the thin gray line represents the 1.5× interquartile range (the rest of the distribution, without outliers). (C) Gene count per barcode from repaired human RNA (loaded at 67.2 pg per well). Sequencing depth: 3.7×10^7 paired-end reads (0.85 million reads per barcode). Barcodes are shown according to spatial placement within device.

To assess the quantification accuracy, the median Pearson correlation coefficient between log2 (input molecules) and log2 (quantified expression values in transcripts per million (TPM)) was computed to be 0.96, which outperforms most competing barcoding methods.[40] We compared our accuracy to a 84 barcode data set published in 2015 by Macosko *et al.*,[41] with a median Pearson correlation coefficient value of 0.90 (Figure 4.6B).

We wanted to check for uniformity of gene detection across wells by loading the device with extracted RNA. We loaded repaired total human RNA at a concentration of 67.2 pg per well (equivalent to the RNA content of a large mammalian cell[43]) and barcoded it on-device. Next, we pooled the device contents and generated the cDNA library in a single tube. We sequenced this library to 0.85 million reads per barcode (Figure 4.6C), which produced 13 182 ± 514 (mean ± S.D.) feature counts per well. These results are encouraging at this sequencing depth[44-46] and importantly, we observed no spatial bias on-device in the distribution of reads among barcodes (Figure S4.4).

Experimental Section

Device fabrication

We used 700 μm thick soda-lime glass plates to fabricate the devices. The plates were coated with 125 Å Cr/1000 Å Au/10000 Å AZ1500 photoresist (TELIC, Valencia, CA). The features were fabricated in the plates with standard multi-step photolithography protocols. Photolithography masks (see ESI†) were designed in AutoCAD (Autodesk, San Rafael, CA) and printed by CAD/Art Services, Inc. (Bandon, OR). The volumes of features were also calculated, based on isotropic etching modeling in AutoCAD. Holes for loading/unloading were drilled in the plate with the mixing wells with a diamond drill bit (0.035″ diameter; Harvey Tool, Rowley, MA). The glass plates were then plasma treated and gas-phase silanized with dichlorodimethylsilane (Sigma, Cat.# 440272), as described in previous works.[25]

Reagent pre-spotting

For pre-spotting of oligo barcodes, we used trehalose solution (100 nL droplets of 20 mM trehalose), for its documented nucleic acid stabilization properties[47] as well as adhesive properties. Once dried for at least 15 min, trehalose-containing droplets result in sticky semi-crystalline spots that securely stay in wells during device assembly. Spotting was performed with automated BIODOT AD2000 aspirate/dispense platform (BIODOT, Irvine, CA), but may also be done by manual pipetting.

Device assembly

The plates were assembled by pipetting 0.5 mL of 50 cSt silicone oil (Clearco Products, Willow Grove, PA) on one of the plates and sandwiching the oil with the other plate. Aligning and slipping was performed manually under 2× magnification.

Device operation

Prior to loading, the oil was drained from an aligned fluidic channel by applying negative relative pressure at the device outlet. This was done by either a micropipette or with a syringe with an

attached micropipette plastic tip. Sample loading was performed with a micropipette at the device inlet, which can be sped-up by using a second pipette at the outlet to increase the pressure difference between inlet and outlet. This device may be slipped either before removing pipettes or after. Alternatively, the user can remove one pipette, slip one side, then remove the second pipette, and slip the other side of the device.

Epi-fluorescence imaging of drop-in/merging

Imaging of 50 μM Alexa Fluor 488 dye solution (Thermo Fisher, Waltham, MA) was performed on Leica DMI6000B with Leica A8 automated stage (Leica Microsystems, Buffalo Grove, IL), interfaced with MetaMorph software (MetaMorph, Nashville, TN).

Confocal microscopy for metering quantification

Imaging of 50 μM Alexa Fluor 488 dye solution (ThermoFisher, Waltham, MA) was performed on Zeiss LSM 800 interfaced with ZEN 2 blue edition software (Zeiss, Oberkochen, Germany). Up to 20x magnification was used, but higher resolution is possible with long working distance objectives. Calculation of volumes was performed using Imaris suite v9.1.0 (Bitplane, Concord, MA) (Figure S4.3). The Smooth/Surface Detail was set at 4 μm, and the absolute intensity threshold was selected automatically by the software.

In our analysis of the reproducibility and spatial distribution of volume metering (Figure 4.4), we investigated statistically the uniformity of volume metering in the edge wells. We used a two-tailed Welch's t test ($\alpha = 0.05$). For wells of type 5, the volumes of the edge wells (A08 and A01) were not significantly different from the volumes of the type 5 wells (P-values of 0.591 and 0.947, respectively). In wells of type 7, the volumes of the edge wells (A08 and A01) were also not statistically different from the rest of the type 7 well volumes (P-values of 0.179 and 0.114, respectively).

Using device for barcoding RNA transcripts (ERCC transcripts and repaired human RNA)

The device that was used for this validation was a prototype with 43 barcoded wells. Mix 1 of ERCC transcripts (Thermo Fisher, Cat.# 4456740) was diluted 220 times in PBS and dropped-in into the mixing wells using 3 nL carrier wells (this corresponds to 850 067 transcripts per well). Lysis buffer was added using 5 nL carrier wells (no heating steps were performed at this point). RNA fragments repair solution was added with 8 nL carrier wells, followed by 30-minute incubation at 37 °C. RNA denaturing agent dimethyl sulfoxide (DMSO) solution was added next in 5.4 nL carrier wells, and the pre-spotted ssRNA adaptors with barcodes (with blocking groups on their 3′ ends) in the next set of carrier wells were dissolved in the reaction mix. At this point, the device was incubated at 65 °C for 2.5 min to melt any secondary RNA structures, then immediately placed on ice. Next, T4 RNA Ligase solution was added in the 20 nL wells, followed by an addition of PEG solution in the 28.6 nL wells. The device was incubated at room temperature for at least 4 hours. After ligation, the device was frozen and stored at −20 °C before pooling samples. To pool barcoded nucleic acids, the device was thawed and slipped to the pooling position (Figure 4.2I) and the contents were collected with a pipette. To maximize recovery, the channel was washed two times with 10 μL of wash buffer containing EDTA (which chelates Mg^{2+} ions and stops enzyme activity), non-ionic detergent and RNase inhibitor. The eluent of these wash steps was combined with the pooled sample for subsequent off-device steps.

For the experiment with human total RNA (Figure 4.6C), we loaded water in 3 nL carrier wells and lysis buffer in 5 nL carrier wells to mimic lysis conditions. Next, repaired total human K562 RNA was loaded at 67.2 pg per well in 8 nL wells, along with the RNA fragments repair solution. The heating steps were omitted for this experiment, but the rest of the protocol was carried out as described above. The rest of the cDNA library preparation for 1 and 2 took place in a single tube, in a protocol similar to the one described in RNAtaq-Seq method,[34] starting from step 4, with some modifications (see Supplementary Information). Illumina paired-end sequencing was performed using 34 bp-long read 1 and 36 bp-long read 2.

Sequencing data analysis

Sequence alignment was performed using *STAR* (v. 2.6.1b) with default settings (option – *alignIntronMax* was set to 1 for ERCC spike-in reads). Human RNA reads were aligned to RefSeq human genome assembly GRCh38. UMIs were de-duplicated and counted using the *umi-tools* package (v. 0.5.5). Features were counted using *featureCounts* package (v. 1.6.3). For logistic regression model for sensitivity evaluation, we used a MATLAB built-in function *binofit* to fit the transcript-detection data as binomial trials and applied the regression method from Svensson *et al*. (2017) to estimate parameters a and b to obtain the detection limit (Figure 4.6A):[40]

$$P(\text{detected}_i) = \frac{1}{1+e^{-(a \times \log_2(M_i)+b)}} \quad \text{(Eq. 4.3)}$$

where M_i is the number of ERCC molecules i spiked in and where the detection limit $=2^{-\frac{b}{a}}$.

For dose–response Pearson correlation coefficient for accuracy evaluation, the de-duplicated reads (UMI counts) were converted into normalized units of expression of TPM and the Pearson correlation coefficient between log2 (TPM) and log2 (input ERCC molecules) was calculated for each barcode (Figure 4.6B).

Conclusions

We conceived and validated a device that combines several physical phenomena to provide a simple tool for encapsulation, imaging, and additive protocol execution in nanoliter-scale wells. The multistep SlipChip device allows the user to make repeated and complete droplet transfers that enable multistep processes with the option to retrieve the final products. The key innovation that was foundational to this technology was using the dimensions of device features to shape the interface between two immiscible fluids to facilitate droplet transfer. By adding geometric enhancements, we also improved reproducibility of the droplet merging. Importantly, the operation of the device does not require equipment other than micropipettes and a basic microscope, which makes it an attractive option for many applications.

To illustrate the capabilities of this device, we carried out a complex, 4-part biochemical scheme: transcript barcoding for multiplexed RNA-Seq library preparation. Using standard benchmarking metrics[40] to assess performance, we found that our method for transcript quantification had competitive sensitivity and better accuracy than many existing techniques. Given the multistep device's high performance, we envision that it will be well-suited for single-cell analyses or studies with small numbers of cells. The stochasticity of encapsulation (Poisson loading) will be advantageous to applications with arbitrary cell sizes and shapes. Moreover, because RNAtaq-Seq is an all-inclusive barcoding method, performing this method on the multistep device can be used to study gene expression in prokaryotes.[34] Other features of the multistep device that we believe will be advantageous to biological studies include its optical clarity for high-resolution imaging of loaded specimens and its thin construction for rapid and uniform temperature control, including freezing and thawing.

For applications where higher level of multiplexing is desired, the device can be expanded to have additional wells, or multiple devices can be used together. The devices tested in this work were multiplexed by up to 50 wells. To add more wells, the footprint can be compressed (e.g. features can be placed closer together), which may require higher-precision device slipping than manual operation can provide (e.g. by using a micromanipulator stage or by adding guiding features for manual slipping). Higher number of wells can also be achieved by increasing the total area of the device. In this case, the user may want to use carrier fluids of lower viscosities to reduce flow resistance in longer channels.

This technology is not limited to the surface chemistry and fluids described in this work. We demonstrated the addition of multiple liquids and a pre-spotted solid reagent, but this device can also be used to meter gas-phase reagents. It is worth noting that differences in droplet sizes and surfactant contents, as well as carrier fluid viscosities, can be modulated in this platform to further enhance droplet coalescence and mixing.[36,37,48]

For applications where immediate droplet merging is not desired (e.g., to create a stable emulsion of many co-encapsulated incompatible reagents), one can select a stabilizing combination of sample and carrier fluids and surfactants to create multiplexed emulsions of heterogeneous or homogeneous

combinations of droplets using this drop-in device. Simultaneous merging of such emulsions may be accomplished by heat, a freeze-thaw cycle, or the addition of a reagent.

In addition to single-cell RNA-Seq and other single-cell assays, we anticipate this technology to be useful in other applications that benefit from multistep processing on a nanoliter scale, such as single-molecule assays, cell–cell interaction studies, clonal micro-colony studies, combinatorial approaches to protein crystallization,[49] titrations, chemical synthesis, synthesis of monodispersed particles[50-52] and heterogeneous colloidal assemblies,[53,54] kinetics studies, batch and semibatch nanoliter reactors, and diagnostic assays.

References

1. T. Taniguchi, T. Torii, and T. Higuchi, "Chemical reactions in microdroplets by electrostatic manipulation of droplets in liquid media," *Lab on a Chip*, **2002**, 2, 19-23.
2. M. Srisa-Art, A. J. deMello, and J. B. Edel, "High-Throughput DNA Droplet Assays Using Picoliter Reactor Volumes," *Analytical Chemistry*, **2007**, 79, 6682-6689.
3. B. Hadwen, G. Broder, D. Morganti, A. Jacobs, C. Brown, J. Hector, Y. Kubota, and H. Morgan, "Programmable large area digital microfluidic array with integrated droplet sensing for bioassays," *Lab on a Chip*, **2012**, 12, 3305-3313.
4. C. J. Gerdts, D. E. Sharoyan, and R. F. Ismagilov, "A synthetic reaction network: chemical amplification using nonequilibrium autocatalytic reactions coupled in time," *Journal of the American Chemical Society*, **2004**, 126, 6327-6331.
5. I. Shestopalov, J. D. Tice, and R. F. Ismagilov, "Multi-step synthesis of nanoparticles performed on millisecond time scale in a microfluidic droplet-based system," *Lab on a Chip*, **2004**, 4, 316-321.
6. S. Ma, Y.-P. Hsieh, J. Ma, and C. Lu, "Low-input and multiplexed microfluidic assay reveals epigenomic variation across cerebellum and prefrontal cortex," *Science Advances*, **2018**, 4, eaar8187.
7. A. R. Wu, N. F. Neff, T. Kalisky, P. Dalerba, B. Treutlein, M. E. Rothenberg, F. M. Mburu, G. L. Mantalas, S. Sim, and M. F. Clarke, "Quantitative assessment of single-cell RNA-sequencing methods," *Nature Methods*, **2014**, 11, 41.

8. F. Shen, E. K. Davydova, W. Du, J. E. Kreutz, O. Piepenburg, and R. F. Ismagilov, "Digital isothermal quantification of nucleic acids via simultaneous chemical initiation of recombinase polymerase amplification reactions on SlipChip," *Analytical Chemistry*, **2011**, 83, 3533-3540.
9. D. R. Link, E. Grasland-Mongrain, A. Duri, F. Sarrazin, Z. Cheng, G. Cristobal, M. Marquez, and D. A. Weitz, "Electric Control of Droplets in Microfluidic Devices," *Angewandte Chemie International Edition*, **2006**, 45, 2556-2560.
10. S. Lee, H. Kim, D.-J. Won, J. Lee, and J. Kim, "On-demand, parallel droplet merging method with non-contact droplet pairing in droplet-based microfluidics," *Microfluidics and Nanofluidics*, **2016**, 20, 1.
11. L. Li, J. Q. Boedicker, and R. F. Ismagilov, "Using a multijunction microfluidic device to inject substrate into an array of preformed plugs without cross-contamination: comparing theory and experiments," *Analytical Chemistry*, **2007**, 79, 2756-2761.
12. E. Laks, H. Zahn, D. Lai, A. McPherson, A. Steif, J. Brimhall, J. Biele, B. Wang, T. Masud, and D. Grewal, "Resource: Scalable whole genome sequencing of 40,000 single cells identifies stochastic aneuploidies, genome replication states and clonal repertoires," *bioRxiv*, **2018**, 411058.
13. A. Rival, D. Jary, C. Delattre, Y. Fouillet, G. Castellan, A. Bellemin-Comte, and X. Gidrol, "An EWOD-based microfluidic chip for single-cell isolation, mRNA purification and subsequent multiplex qPCR," *Lab on a Chip*, **2014**, 14, 3739-3749.
14. A. Wang, A. Abdulla, and X. Ding, "Microdroplets-on-chip: A review," *Proceedings of the Institution of Mechanical Engineers. Part H, Journal of Engineering in Medicine*, **2019**, 954411919850912.
15. A. C. Hatch, J. S. Fisher, A. R. Tovar, A. T. Hsieh, R. Lin, S. L. Pentoney, D. L. Yang, and A. P. Lee, "1-Million droplet array with wide-field fluorescence imaging for digital PCR," *Lab on a Chip*, **2011**, 11, 3838-3845.
16. M. Kim, M. Pan, Y. Gai, S. Pang, C. Han, C. Yang, and S. K. Tang, "Optofluidic ultrahigh-throughput detection of fluorescent drops," *Lab on a Chip*, **2015**, 15, 1417-1423.

17. V. Yelleswarapu, J. R. Buser, M. Haber, J. Baron, E. Inapuri, and D. Issadore, "Mobile platform for rapid sub–picogram-per-milliliter, multiplexed, digital droplet detection of proteins," *Proceedings of the National Academy of Sciences*, **2019**, 116, 4489-4495.
18. S. R. Doonan, M. Lin, and R. C. Bailey, "Droplet CAR-Wash: continuous picoliter-scale immunocapture and washing," *Lab on a Chip*, **2019**, 19, 1589-1598.
19. S. S. Schütz, T. Beneyton, J.-C. Baret, and T. M. Schneider, "Rational design of a high-throughput droplet sorter," *Lab on a Chip*, **2019**, 19, 2220-2232.
20. W. Du, L. Li, K. P. Nichols, and R. F. Ismagilov, "SlipChip," *Lab on a Chip*, **2009**, 9, 2286-2292.
21. S. M. Prakadan, A. K. Shalek, and D. A. Weitz, "Scaling by shrinking: empowering single-cell'omics' with microfluidic devices," *Nature Reviews Genetics*, **2017**, 18, 345.
22. A. A. Kolodziejczyk, J. K. Kim, V. Svensson, J. C. Marioni, and S. A. Teichmann, "The technology and biology of single-cell RNA sequencing," *Molecular Cell*, **2015**, 58, 610-620.
23. A.-E. Saliba, A. J. Westermann, S. A. Gorski, and J. Vogel, "Single-cell RNA-seq: advances and future challenges," *Nucleic Acids Research*, **2014**, 42, 8845-8860.
24. L. Li, W. Du, and R. Ismagilov, "User-loaded SlipChip for equipment-free multiplexed nanoliter-scale experiments," *Journal of the American Chemical Society*, **2009**, 132, 106-111.
25. F. Shen, W. Du, E. K. Davydova, M. A. Karymov, J. Pandey, and R. F. Ismagilov, "Nanoliter multiplex PCR arrays on a SlipChip," *Analytical Chemistry*, **2010**, 82, 4606-4612.
26. R. R. Pompano, C. E. Platt, M. A. Karymov, and R. F. Ismagilov, "Control of initiation, rate, and routing of spontaneous capillary-driven flow of liquid droplets through microfluidic channels on SlipChip," *Langmuir*, **2012**, 28, 1931-1941.
27. W. Liu, D. Chen, W. Du, K. P. Nichols, and R. F. Ismagilov, "SlipChip for immunoassays in nanoliter volumes," *Analytical Chemistry*, **2010**, 82, 3276-3282.
28. M. Yu, X. Chen, H. Qu, L. Ma, L. Xu, W. Lv, H. Wang, R. F. Ismagilov, M. Li, and F. Shen, "Multistep SlipChip for the Generation of Serial Dilution Nanoliter Arrays and

Hepatitis B Viral Load Quantification by Digital Loop Mediated Isothermal Amplification," *Analytical Chemistry*, **2019**, 91, 8751-8755.

29. F. Shen, B. Sun, J. E. Kreutz, E. K. Davydova, W. Du, P. L. Reddy, L. J. Joseph, and R. F. Ismagilov, "Multiplexed quantification of nucleic acids with large dynamic range using multivolume digital RT-PCR on a rotational SlipChip tested with HIV and hepatitis C viral load," *Journal of the American Chemical Society*, **2011**, 133, 17705-17712.
30. K. Piroird, C. Clanet, and D. Quéré, "Capillary extraction," *Langmuir*, **2011**, 27, 9396-9402.
31. P. Abbyad, R. Dangla, A. Alexandrou, and C. N. Baroud, "Rails and anchors: guiding and trapping droplet microreactors in two dimensions," *Lab on a Chip*, **2011**, 11, 813-821.
32. R. Dangla, S. Lee, and C. N. Baroud, "Trapping microfluidic drops in wells of surface energy," *Physical Review Letters*, **2011**, 107, 124501.
33. M. Nagel, P.-T. Brun, and F. Gallaire, "A numerical study of droplet trapping in microfluidic devices," *Physics of Fluids*, **2014**, 26, 032002.
34. A. A. Shishkin, G. Giannoukos, A. Kucukural, D. Ciulla, M. Busby, C. Surka, J. Chen, R. P. Bhattacharyya, R. F. Rudy, and M. M. Patel, "Simultaneous generation of many RNA-seq libraries in a single reaction," *Nature Methods*, **2015**, 12, 323.
35. N. Ichikawa, K. Hosokawa, and R. Maeda, "Interface motion of capillary-driven flow in rectangular microchannel," *Journal of Colloid and Interface Science*, **2004**, 280, 155-164.
36. E. Nowak, N. M. Kovalchuk, Z. Che, and M. J. Simmons, "Effect of surfactant concentration and viscosity of outer phase during the coalescence of a surfactant-laden drop with a surfactant-free drop," *Colloids and Surfaces A: Physicochemical and Engineering Aspects*, **2016**, 505, 124-131.
37. E. Nowak, Z. Xie, N. M. Kovalchuk, O. K. Matar, and M. J. Simmons, "Bulk advection and interfacial flows in the binary coalescence of surfactant-laden and surfactant-free drops," *Soft Matter*, **2017**, 13, 4616-4628.
38. J. Atencia and D. J. Beebe, "Controlled microfluidic interfaces," *Nature*, **2004**, 437, 648.

39. Y. Kang, M. H. Norris, J. Zarzycki-Siek, W. C. Nierman, S. P. Donachie, and T. T. Hoang, "Transcript amplification from single bacterium for transcriptome analysis," *Genome Research*, **2011**, 21, 925-935.

40. V. Svensson, K. N. Natarajan, L.-H. Ly, R. J. Miragaia, C. Labalette, I. C. Macaulay, A. Cvejic, and S. A. Teichmann, "Power analysis of single-cell RNA-sequencing experiments," *Nature Methods*, **2017**, 14, 381.

41. E. Z. Macosko, A. Basu, R. Satija, J. Nemesh, K. Shekhar, M. Goldman, I. Tirosh, A. R. Bialas, N. Kamitaki, and E. M. Martersteck, "Highly parallel genome-wide expression profiling of individual cells using nanoliter droplets," *Cell*, **2015**, 161, 1202-1214.

42. C. Ziegenhain, B. Vieth, S. Parekh, B. Reinius, A. Guillaumet-Adkins, M. Smets, H. Leonhardt, H. Heyn, I. Hellmann, and W. Enard, "Comparative analysis of single-cell RNA sequencing methods," *Molecular Cell*, **2017**, 65, 631-643. e634.

43. A. T. Dobson, R. Raja, M. J. Abeyta, T. Taylor, S. Shen, C. Haqq, and R. A. R. Pera, "The unique transcriptome through day 3 of human preimplantation development," *Human Molecular Genetics*, **2004**, 13, 1461-1470.

44. L. F. García-Ortega and O. Martínez, "How many genes are expressed in a transcriptome? Estimation and results for RNA-Seq," *PloS One*, **2015**, 10, e0130262.

45. D. Ramsköld, S. Luo, Y.-C. Wang, R. Li, Q. Deng, O. R. Faridani, G. A. Daniels, I. Khrebtukova, J. F. Loring, and L. C. Laurent, "Full-length mRNA-Seq from single-cell levels of RNA and individual circulating tumor cells," *Nature Biotechnology*, **2012**, 30, 777.

46. T. M. Gierahn, M. H. Wadsworth II, T. K. Hughes, B. D. Bryson, A. Butler, R. Satija, S. Fortune, J. C. Love, and A. K. Shalek, "Seq-Well: portable, low-cost RNA sequencing of single cells at high throughput," *Nature Methods*, **2017**, 14, 395.

47. K. L. Jones, D. Drane, and E. J. Gowans, "Long-term storage of DNA-free RNA for use in vaccine studies," *BioTechniques*, **2007**, 43, 675-681.

48. A. Anilkumar, C. Lee, and T. Wang, "Surface-tension-induced mixing following coalescence of initially stationary drops," *Physics of Fluids A: Fluid Dynamics*, **1991**, 3, 2587-2591.

49. C. L. Hansen, E. Skordalakes, J. M. Berger, and S. R. Quake, "A robust and scalable microfluidic metering method that allows protein crystal growth by free interface diffusion," *Proceedings of the National Academy of Sciences*, **2002**, 99, 16531-16536.

50. D. Dendukuri and P. S. Doyle, "The synthesis and assembly of polymeric microparticles using microfluidics," *Advanced Materials*, **2009**, 21, 4071-4086.

51. C. H. Choi, J. Lee, K. Yoon, A. Tripathi, H. A. Stone, D. A. Weitz, and C. S. Lee, "Surface-tension-induced synthesis of complex particles using confined polymeric fluids," *Angewandte Chemie International Edition*, **2010**, 49, 7748-7752.

52. C. H. Choi, J. M. Jeong, S. M. Kang, C. S. Lee, and J. Lee, "Synthesis of monodispersed microspheres from laplace pressure induced droplets in micromolds," *Advanced Materials*, **2012**, 24, 5078-5082.

53. S. Y. Lee and S. Yang, "Fabrication and Assembly of Magneto-Responsive, Anisotropic, and Hybrid Microparticles of Variable Size and Shape," *Angewandte Chemie International Edition*, **2013**, 52, 8160-8164.

54. F. Li, D. P. Josephson, and A. Stein, "Colloidal assembly: the road from particles to colloidal molecules and crystals," *Angewandte Chemie International Edition*, **2011**, 50, 360-388.

Supplementary Information

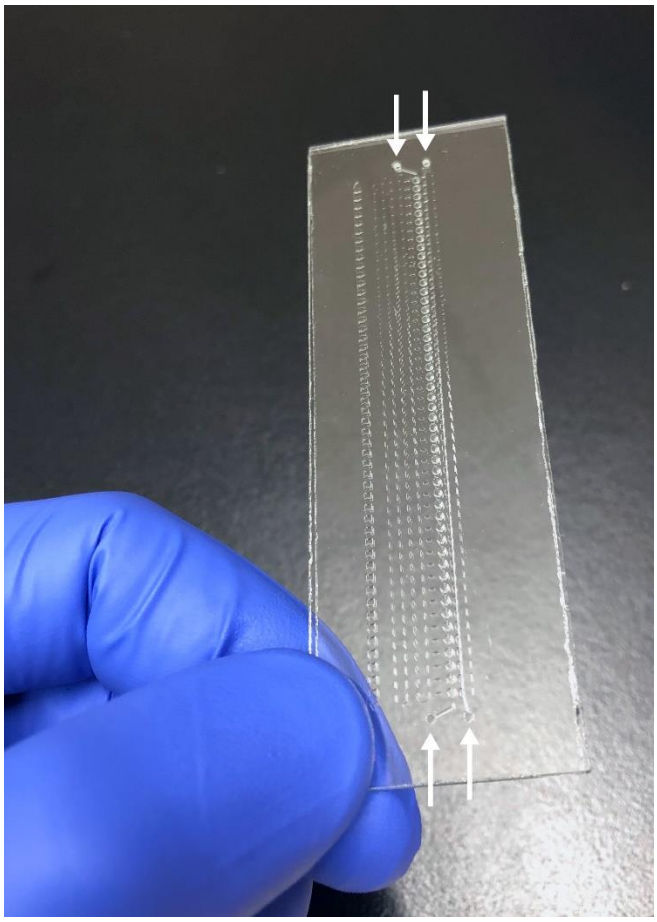

Figure S4.1 Photo of the multistep SlipChip. The arrows indicate drilled holes for device inlets and outlets. The footprint of the device is 27.4 x 82.9 mm.

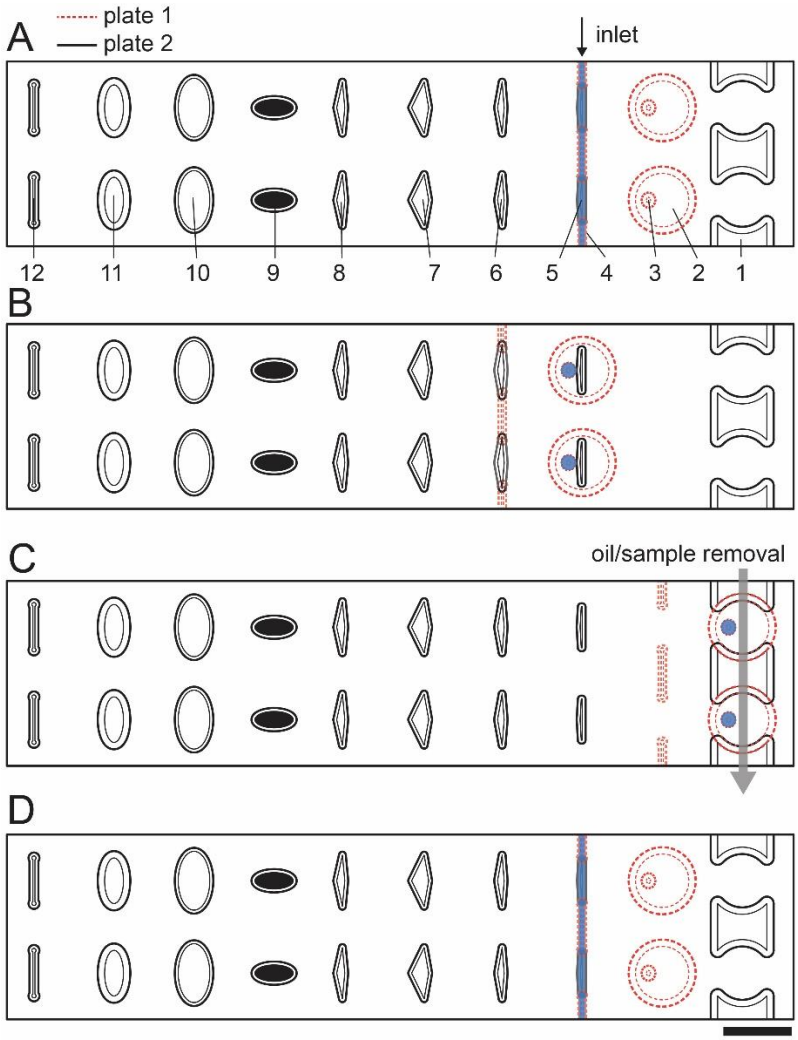

Figure S4.2 Top-down view shows the two-row section of the multistep device performing evacuation of the loaded mixing wells. (A) The multistep device is made of two plates, shown assembled and aligned. Features [1-12] and their corresponding depths: [1] evacuation channels (100 µm); [2] mixing wells (100 µm); [3] surface energy traps at the bottom of mixing wells (70 µm), mixing wells have a capacity of 71 nL together with the surface energy traps; [4] connecting channels (40 um); [5] sample wells, 3.3 nL (50 um); [6] lysis solution wells, 5 nL (50 um); [7] RNA 3'-end repair solution wells, 7.4 nL (50 um); [8] denaturing agent loading wells, 5.4 nL (50 um); [9] barcode wells (50 µm); [10] ligation mix wells, 20 nL (50 µm); [11] crowding agent wells, 28.6 nL (100 µm); [12] channels for optional clearing of the connecting channels [4]. First set of wells [5] is being loaded through the via holes. Via holes for loading/unloading are drilled in plate 1 (not shown). (B)

Sample drop-in into mixing wells. In this configuration, the user can image the loaded samples to make sure under- or over-loading did not occur. (C) To restart the experiment, the device needs to be slipped into this conformation and the previously loaded sample pipetted out together with oil through the channel formed by connected mixing wells [2] and evacuation channels [1]. Channels [1] were shaped to minimize footprint while still fully overlapping with wells [2] during evacuation. Making the depth of the evacuation channels similar to the depth of the mixing wells prevents the sample droplets from being left behind in the deeper parts of the well-channel fluidic pathway. Fresh oil needs to be reloaded before the device is returned to conformation A. (D) the device is returned to the same starting conformation as A, and the new sample can be loaded. Scale bar: 1 mm.

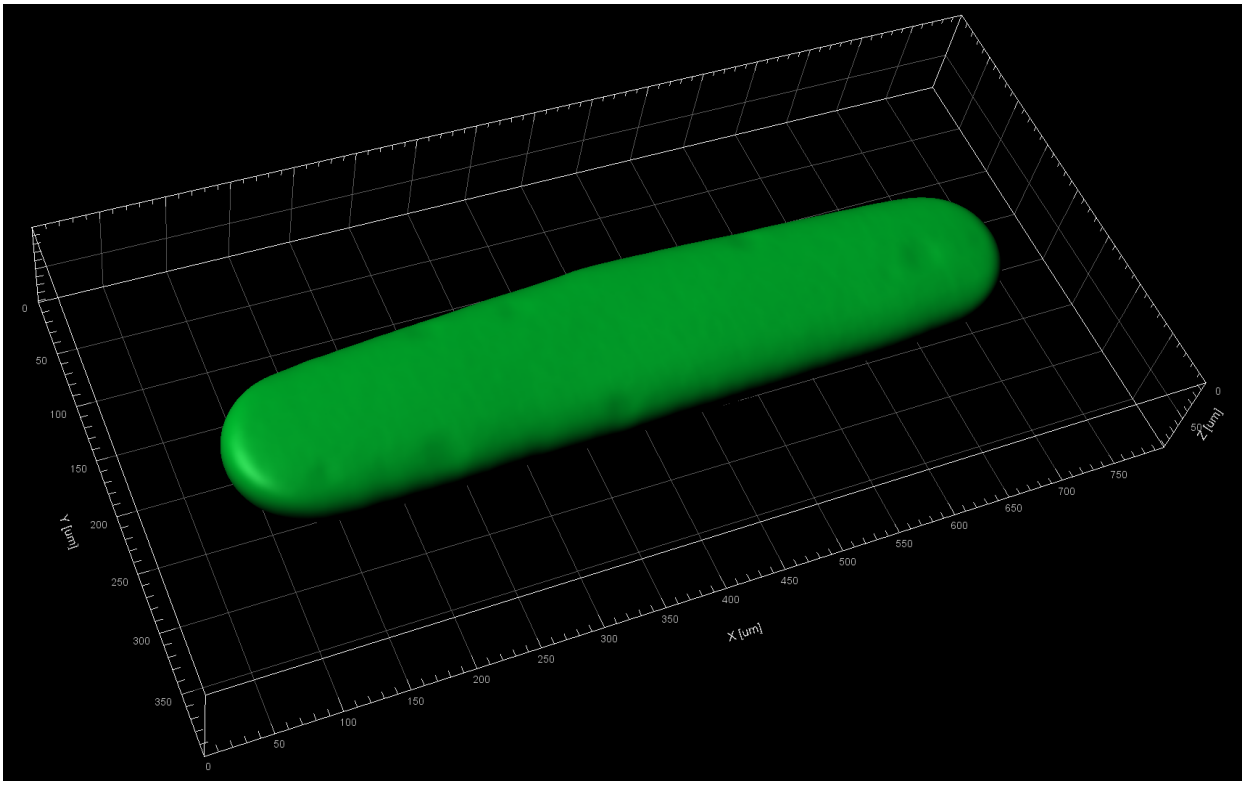

Figure S4.3 A three-dimensional reconstruction of a droplet inside a 3-nL well from confocal Z-stack for volume calculation in Imaris.

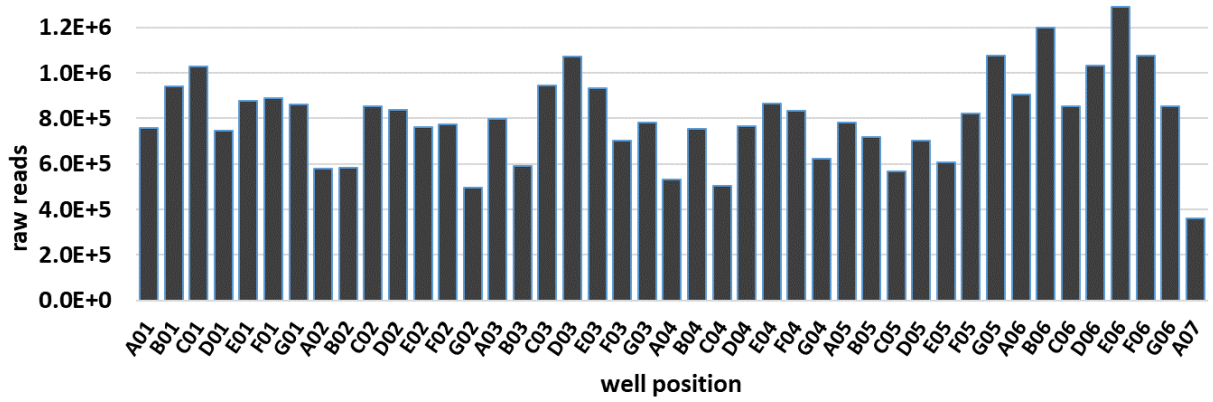

Figure S4.4 Spatial distribution of barcoded reads within the device for repaired total human RNA experiment. Reads per well that received a barcode: 802,812 ± 194,210 (mean ± S.D.).

Materials and Methods

Differences and modifications to RNAtag-Seq protocol

1. UMIs (NNNNNNNN) were added to the RNA fragments during the second ligation.
2. rRNA depletion step was skipped.
3. Superscript IV (Invitrogen, Cat.# 18090050) enzyme was used for reverse transcription (RT).
4. RT primer (p14) was one base shorter than the published AR23 oligo:
   5´–/5SpC3/CTACACGACGCTCTTCC –3´ (IDT) was used for RT.
5. Second adaptor for ligation (p38) had UMI, C3 spacer and 5’ phosphate as follows:
   5’–/5Phos/ANNNNNNNNAGATCGGAAGAGCACACGTCT/3SpC3/–3’ (IDT).
6. We used Dynabeads MyOne Silane magnetic beads (Life Technologies, Cat.# 37002D) instead of using Zymo columns and RNAClean XP beads. Final concentration of EtOH in the mixture of RLT buffer (Qiagen, Cat.# 79216), RLT-washed Dynabeads MyOne Silane magnetic beads, and samples was 60% to clean up after the first linker ligation and RT step, and 70% of the final total volume after the second ligation.
7. Q5 Hot start High Fidelity DNA polymerase (NEB, 2XMasterMix, Cat.# M0494S) was used for the library PCR amplification with Illumina primers. Primer annealing was performed at

68 °C for the first 3 cycles and at 70 °C for the rest of the cycles (18). The number of PCR cycles with Illumina primers was further adjusted: after initial amplification for 21 cycles, we visualized libraries on agarose gel by gel electrophoresis using 1% E-gel EX (ThermoFisher, Cat.# G401001). To remove artifacts and Illumina adaptor dimers (that were major products of amplification at that stage), we cut gels to collect fragments between 200 bases and 800 bases. Next, we extracted libraries from gel using Zymo Gel Clean DNA recovery kit (Zymo Research, Cat.# D4002), subjected them to additional amplification to compensate for dilution, and added 3 more cycles. To remove artifacts and Illumina primers after the amplification, we cleaned the libraries using 0.9% AmPure XP SPRI beads (Beckman Coulter, Cat.# A63880) twice.

Reagents for on-device steps

- **RNA samples** (added to mixing wells with 3 nL carrier wells):
    - Diluted in UltraPure DNase/RNase-free distilled water (Invitrogen, Cat.# 10977-015)
- **Lysis buffer** is based on the buffer used in Kang *et al*. (2015)[1] (added to mixing wells with 5 nL carrier wells):
    - 100 mM Tris-Cl pH 8.0 (ThermoFisher Scientific, Cat.# BP1758-100)
    - 200 mM KCl (Invitrogen, Cat.# AM9640G)
    - 0.2 mM EDTA (OmniPur, Calbiochem, Cat.# 6381-92-6)
    - 0.1% Triton X-100 (Sigma, Cat.# T8787-50ML)
    - 2 mM DTT (Invitrogen, a tube from SuperScript IV kit, Cat.# 900147)
    - UltraPure DNase/RNase-free distilled water (Invitrogen, Cat.# 10977-015)
    - 0.5 U/µL SUPERase-In (Ambion, Cat.#AM2694; 2500U)
    - 1 µg/µL BSA (Roche, Cat.# 10711454001)
- **RNA fragments repair solution** (added to mixing wells with 8 nL carrier wells)**:**
    - 2 U/µL T4 PNK (NEB, Cat.# M0201S)
    - 2x T4 PNK buffer (NEB, Cat.# B0201S)
    - 0.25 mM $MgCl_2$ (NEB, Cat.# B9021S)
    - 0.5 U/µL SUPERase-In (Ambion, Cat.# AM2694)

- 1 µg/µL BSA (Roche, Cat.# 10711454001)
- UltraPure DNase/RNase-free distilled water (Invitrogen, Cat.# 10977-015)

- **RNA denaturing agent solution** (added to mixing wells with 5.4 nL carrier wells)**:**
  - 95% v/v DMSO (Sigma, Cat.# D2650)
  - 5% of 20 µg/µL BSA stock (Roche, Cat.# 10711454001)
- **Barcoded ssRNA adaptors** (from Shishkin, *et al*. (2015), with a blocking group on their 3' ends (*3SpC3)* to avoid self-ligation)[2]:
  - 100 nL droplets containing 0.4 µM of adaptor and 20 mM trehalose were spotted and pre-dried in each well.
    - An example of a barcoded RNA adaptor, barcode sequence in red:
    - 5Phos/**rArUrGrArArUrU***rArGrArUrCrGrGrArArGrArGrCrGrUrCrGrUrG***rU***rArG**/3SpC3/
- **T4 RNA ligase solution** (added to mixing wells with 20 nL carrier wells):
  - 3.1x T4 RNA ligase buffer (NEB, Cat.# MO437M)
  - 3.1 mM ATP (Roche, Cat.# 11140965001)
  - 1 µg/µL BSA (Roche, Cat.# 10711454001)
  - 0.6 U/µL SUPERase-In (Ambion, Cat.#AM2694; 2500U)
  - 5.26 U/µL T4 RNA ligase (NEB, Cat.# MO437M)
  - 25% v/v MyOne Silane magnetic beads (Life Technologies, Cat.# 37002D) washed four times in UltraPure DNase/RNase-free distilled water and mixed with the UltraPure DNase/RNase-free distilled water to restore the original volume.
  - UltraPure DNase/RNase-free distilled water (Invitrogen, Cat.# 10977-015)
- **PEG solution** (added to mixing wells with 28.6 nL carrier wells):
  - 39.5% PEG8000 (Sigma, Cat.# 83271-100ML-F, PCode:101129041)
  - 17.5% v/v MyOne Silane magnetic beads (Life Technologies, Cat.# 37002D) washed four times in UltraPure DNase/RNase-free distilled water and mixed with the UltraPure DNase/RNase-free distilled water to restore the original volume.
  - 0.7 µg/µL BSA (Roche, Cat.# 10711454001)
- **Wash buffer:**

- 0.05% NP-40 Surfact-Amps™ Detergent Solution (ThermoFisher Scientific, Cat.# 85124)
- 0.5 U/μL SUPERase-In (Ambion, Cat.# AM2694)
- 1 μg/μL BSA (Roche, Cat.# 10711454001)
- All reagents were dissolved in 1x TE buffer, pH 7.5 (Affymetrix, Cat.# PN733893).

Supplementary References

1. Y. Kang, I. McMillan, M. H. Norris, and T. T. Hoang, "Single prokaryotic cell isolation and total transcript amplification protocol for transcriptomic analysis," *Nature Protocols*, **2015**, 10, 974.
2. A. A. Shishkin, G. Giannoukos, A. Kucukural, D. Ciulla, M. Busby, C. Surka, J. Chen, R. P. Bhattacharyya, R. F. Rudy, and M. M. Patel, "Simultaneous generation of many RNA-seq libraries in a single reaction," *Nature Methods*, **2015**, 12, 323.